

NONLINEAR OPTICAL MICROSCOPY FOR PHARMACEUTICAL FORMULATION DEVELOPMENT

by
Sreya Sarkar

A Dissertation

*Submitted to the Faculty of Purdue University
In Partial Fulfillment of the Requirements for the degree of*

Doctor of Philosophy



Department of Chemistry
West Lafayette, Indiana
August 2019

THE PURDUE UNIVERSITY GRADUATE SCHOOL
STATEMENT OF COMMITTEE APPROVAL

Dr. Garth Simpson, Chair

Department of Chemistry

Dr. Mary Wirth

Department of Chemistry

Dr. Adam Wasserman

Department of Chemistry

Dr. Lynne Taylor

Department of Industrial and Physical Pharmacy

Approved by:

Dr. Christine Hrycyna

Head of the Graduate Program

Dedicated to the loving memory of my father, who always believed in me.

ACKNOWLEDGMENTS

In the past years of my journey of graduate school at Purdue, I have learned that obtaining a doctoral degree is not only limited to building exceptional scientific acumen, it is a great personal development process, which prepares one to face any challenges of life in general. Therefore, it has not been a journey of all by myself, a great number of people have contributed in every step, knowingly or unknowingly.

First of all, I am grateful to my father, Manoranjan Sarkar, with deepest sadness we lost him last year unfortunately, for always encouraging me to never lose hope on anything. He always dreamed envisioning this day, and I know he is always there with me, as always he used to say. I am forever thankful to my mother, Mala Sarkar and my brother, Soumya for their unconditional love and support. I cannot thank my Maa and Baba enough for all the sacrifices they made for the family.

I would like to extend my sincere thanks to my advisor, Prof. Garth Simpson. When I first came to Purdue Chemistry Department to pursue my doctoral degree with lots of confusion in my mind, I was amazed by Garth's excitement for doing science, and without any doubt I knew I wanted to work with him for the next five years. I have learnt great many things from him, always thriving for doing "cool" science, maintaining a positive attitude and wearing a smile, and most important of all, always make time for family.

I would like to thank my collaborators at AbbVie Inc., Dr. Andrew Vogt and Dr. Gerald Danzer from the NCE Analytical R&D, PAC group. The whole group had been really welcoming during my summer internship at AbbVie, and our collaboration in the past three years has been an outstanding learning experience for my career. I would also like to acknowledge Prof. Lynne Taylor, and Ahmed Elkhazab from her group at Purdue College of Pharmacy. I feel myself truly fortunate for being able to closely work with these current and future scientific leaders.

To all the past and current members of the Simpson Lab, specially, Zhengtian, Scott, Casey, Hilary, James, Changqin, Chen, Alex, Andreas, Youlin, Nita, Jiayue, Ziyi, Minghe, Shijie, Max, Janny, Azhad, thanks so much for making the lab so much fun to work in! Simpson Lab, best lab!!!

My friends outside of the Chemistry department, Aritra, Sanchari, Prabudhya, Esha, Sayan, Somrita, Sayantan, Indrani, Arindam, Srishti, and many more definitely made the journey a lot

smoother with moments full of laughter and fun. I will always treasure the times we spent together with a sense of building another home thousands of miles away from our homeland.

Last but not the least, I would like to thank Ashesh. I cannot imagine being able to fulfill this journey without you. Thanks for being there with me in all the ups and downs of life for the last seven years. I truly consider myself to be the luckiest person to share all the moments in life with you, and I cannot wait to grow old together!

TABLE OF CONTENTS

LIST OF TABLES.....	9
LIST OF FIGURES	10
LIST OF ABBREVIATIONS.....	13
ABSTRACT.....	15
CHAPTER 1. INTRODUCTION	16
1.1 Enhancement of bioavailability by ASD.....	16
1.2 Physicochemical characterization of drug products by nonlinear optics	18
1.3 SHG microscopy for development of ASDs	19
1.4 Dissertation overview	20
CHAPTER 2. SHG MICROSCOPY OF API NUCLEATION AND GROWTH.....	23
2.1 Introduction	23
2.2 Methods	24
2.3 Results and discussions	25
2.3.1 Low limit of detection for crystallinity during accelerated stability testing	25
2.3.2 Theoretical background for kinetic modeling	28
2.3.3 Nucleation and crystal growth kinetics	30
2.4 Conclusions	34
CHAPTER 3. IN SITU CRYSTAL GROWTH RATE DISTRIBUTIONS OF API BY SINGLE PARTICLE TRACKING.....	35
3.1 Introduction	35
3.2 Methods	37
3.2.1 Design of the <i>in situ</i> platform.....	37
3.3 Results and discussions	38
3.3.1 Validation of the <i>in situ</i> platform	38
3.3.2 SHG imaging during <i>in situ</i> accelerated stability testing.....	41
3.3.3 Single particle tracking.....	43
3.4 Conclusions	46
CHAPTER 4. DISPARITIES IN CRYSTALLIZATION KINETICS OF BULK VERSUS SURFACE CRYSTALS WITHIN ASD FILMS.....	48

4.1	Introduction	48
4.2	Methods	49
4.3	Results and Discussion	50
4.4	Future Direction.....	51
CHAPTER 5. QUANTIFICATION OF CRYSTALLINITY FOR ROD-LIKE PARTICLES BY CALIBRATION-FREE IMAGE ANALYSIS		53
5.1	Introduction	53
5.2	Methods	54
5.2.1	Theoretical background.....	54
5.2.2	Auto-calibration	55
5.3	Results	56
5.3.1	Experimental implementation	56
5.4	Conclusion.....	58
CHAPTER 6. PHASE BEHAVIOR AND CRYSTALLIZATION KINETICS OF EZETIMIBE ASD DURING DISSOLUTION IN BIORELEVANT MEDIA		59
6.1	Introduction	59
6.2	Materials and Methods	60
6.3	Results and Discussions	61
6.3.1	Dissolution behavior in sodium phosphate buffer.....	62
6.3.2	Dissolution behavior in FeSSIF	64
6.3.3	Dissolution behavior in Ensure Plus®	65
6.4	Conclusions	67
CHAPTER 7. PHASE SEPARATION OF WEAKLY BASIC ASD DURING TWO-STAGE DISSOLUTION PROCESS.....		68
7.1	Introduction	68
7.2	Materials and Methods	69
7.3	Results and Discussions	71
7.3.1	Study of phase separation during dissolution by SHG and TPE-UVF	71
7.3.2	Quantification of crystalline and undissolved amorphous drug content	72
7.4	Conclusion.....	78

CHAPTER 8. NON-NEGATIVE MATRIX FACTORIZATION FOR ISOLATING DAMAGE-FREE REFLECTIONS IN MACROMOLECULAR SYNCHROTRON DATA COLLECTION	79
8.1 Introduction	79
8.2 Methods	80
8.2.1 Synchrotron XRD data acquisition	80
8.2.2 Algorithm	81
8.2.2.1 Dimension Reduction	81
8.2.2.2 NMF	82
8.2.3 Kinetic modeling	83
8.3 Results and Discussions	84
8.3.1 Decomposition into multiple XRD patterns	84
8.3.2 Kinetic modeling of X-ray damage	85
8.3.3 Effect of X-ray exposure around the crystal at room temperature	86
8.4 Conclusions	87
REFERENCES	89
VITA	96
PUBLICATIONS	97

LIST OF TABLES

Table 2.1 Parameters in JMAK model.....	30
Table 6.1. Nucleation and growth kinetics obtained from SHG microscopy images analysis measured in different dissolution media ($n = 3$)	63

LIST OF FIGURES

Figure 1.1. Biopharmaceutical classification system of drugs.	16
Figure 1.2. Schematic of relative free energies of amorphous versus crystalline states of API... 17	17
Figure 1.3. Jablonski diagram for second harmonic generation (SHG).	18
Figure 2.1. SHG images for time-dependent crystal growth in 15% DL ritonavir milled extrudate stressed in 50°C/75% RH and 40°C/75% RH chambers.	26
Figure 2.2. Percent volume fraction of crystallinity from amorphous ritonavir milled extrudate at different stress conditions with detection limit of 10 ppm (0.001%) of total drug loading.....	27
Figure 2.3. Crystal growth rate: Time-dependent ritonavir crystal particle size distribution histogram at (A) 50°C/75%RH, (B) 40°C/75%RH, (C) crystal growth rate depicted by $\ln(r)$ vs. $\ln(t-t_0)$ plot, (D) relationship between crystal growth rate and diffusion coefficient.....	31
Figure 2.4. Kinetics of nucleation, plotted logarithmically to determine the exponential order parameter k in Equation 2.5.	32
Figure 2.5. (A) Near IR spectra (B) Raman spectra of 15%DL ritonavir milled extrudate in 50°C/75% RH after 130 hrs. Both near-IR spectra and Raman spectra indicate the presence of ritonavir crystals in Form II.	33
Figure 3.1. (A), (B) CEiST design, (C) IR thermal image of CEiST for validation of set temperature at 40°C.	36
Figure 3.2. SHG images for time-dependent crystal growth of 15% HME ritonavir in (A) standard chamber, and in (B) CEiST. (C) The plot for average particle areas shows good agreement between the two different methods.	39
Figure 3.3. Time dependent SHG micrographs of 15% ritonavir ASDs stressed in CEiST at 50°C/75%RH.	40
Figure 3.4. (A) Sample taken out of 50OC/75% RH standard chamber every one hour and stayed in room temperature for 15 min each time, (B) sample stayed in 50OC/75% RH standard chamber for 5 hours directly.....	41
Figure 3.5. Individual crystal growth distribution in (A) HME with surfactant, (B) SDD with surfactant, (C) HME without surfactant, and (D) SDD without surfactant. Each plot has 20 different crystals tracked along the entire time trace and selected from different FOVs. The inset in each plot shows the dispersion in growth rates with the average growth rates shown in each plot as dashed line.	42
Figure 3.6. Average nucleation rates for (A) HME with surfactant, (B) SDD with surfactant, (C) HME without surfactant, and (D) SDD without surfactant.	43
Figure 3.7. Anticipated signal to noise ratio of nucleation rate for <i>in situ</i> vs conventional stability testing based on the Poisson statistics of crystal counting. I: nucleation rate, σ : uncertainty of nucleation rate based on Poisson statistics, N_t : number of crystals at time t	45
Figure 4.1. Schematic of "sandwich" and "open-face" seeded films.....	49

Figure 4.2. Evolution of seeded crystals in “sandwich” and “open-face” seeded films over time.	50
Figure 4.3. IR thermal image of the TRHA platform.	51
Figure 5.1. Time evolution of percent crystallinity in 15% ritonavir HME, rotovap, and SDD ASDs stressed <i>in situ</i> temperature and relative humidity-controlled platform at 50°C/75% RH.	57
Figure 6.1. SHG microscopy images of ezetimibe ASDs; (A) PAA at 6, 15, 35, and 120 minutes, (B) PVP at 10, 20, 35 and 120 minutes, and (C) HPMC-AS at 10, 20, 35 and 120 minutes, upon dissolution in sodium phosphate buffer at 37°C. Scale bar: 100 µm.	62
Figure 6.2. SHG microscopy images of ezetimibe ASDs; (A) PAA at 15, 30 and 120 minutes, (B) PVP at 15, 30, and 120 minutes, and (C) HPMC-AS at 30, 120 and 240 minutes, upon dissolution in FeSSIF at 37°C. Scale bar: 100 µm.	65
Figure 6.3. SHG microscopy images of ezetimibe ASDs; (A) PAA at 25, 45, 60 and 120 minutes, (B) PVP at 30, 60, 75 and 120 minutes, and (C) HPMC-AS at 75, 120, 150 and 180 minutes, upon dissolution in Ensure Plus® at 37°C. Scale bar: 100 µm.	66
Figure 7.1. Schematic of the two-stage dissolution experiments.	70
Figure 7.2. SHG images of posaconazole ASDs prepared at (A) 10%, (B) 25%, (C) 50% drug loading and (D) tablet powder upon suspension/dissolution in FaSSGF for 30 minutes (left column), dissolution in FaSSIF for 30 minutes (middle column), and dissolution in FaSSIF for 180 minutes (right column). Scale bar: 100 µm.	73
Figure 7.3. Brightfield and TPE-UVF images of posaconazole ASDs prepared at (A) 10%, (B) 25%, (C) 50% drug loading and (D) tablet powder upon suspension/dissolution in FaSSGF for 30 minutes (left column), dissolution in FaSSIF for 30 minutes (middle column), and dissolution in FaSSIF for 180 minutes (right column). The corresponding brightfield images for (A) 10% ASDs are shown in the first row. Scale bar: 100 µm.	74
Figure 7.4. Volume fraction (%) calculated for (A) SHG signal (crystallinity) and (B) TPE-UVF signal (undissolved posaconazole either in amorphous or crystalline form) for all ASDs and the tablet powder at different time points, upon dissolution in FaSSGF then FaSSIF. The dashed vertical line denotes media transfer at that timepoint. Error bars are omitted for clarity.	75
Figure 7.5. Ratio of volume fraction crystallinity to volume fraction posaconazole (from Figure 7.4) during suspension/dissolution in FaSSGF after 30 minutes.	77
Figure 8.1. Schematic for data collection by X-ray radiation around the crystal at room temperature.	81
Figure 8.2. Flowchart of the algorithm for dimension reduction followed by NMF.	84
Figure 8.3. (A), (B), (C) Decomposed XRD patterns for three components; (D), (E), (F) angular distribution of the peaks in three respective components.	85
Figure 8.4. Kinetics of propagation of damage at cryogenic conditions.	86

Figure 8.5. (A) Change in the overall integrated intensity of XRD peaks, (B), (C), and (D) decomposition into multiple components after applying NMF due to damage induced by radiation around the crystal at room temperature. 87

LIST OF ABBREVIATIONS

API	Active Pharmaceutical Ingredient
ASD	Amorphous Solid Dispersions
BCS	Biopharmaceutical Classification System
CEiST	Controlled Environment for <i>In-situ</i> Stability Testing
DL	Drug Loading
DOF	Depth of Field
DSC	Differential Scanning Calorimetry
FASSGF	Fasted-State Simulated Gastric Fluid
FASSIF	Fasted-State Simulated Intestinal Fluid
FDA	Food and Drug Administration
FeSSIF	Fed-State Simulated Intestinal Fluid
FoV	Field of View
FTIR	Fourier-Transform Infrared
GM/CA@APS	General Medicine and Cancer at Advanced Photon Source
HARP	High Aspect-Ratio Particle
HME	Hot Melt Extrusion
HPMC-AS	Hydroxypropyl Methylcellulose Acetyl Succinate
IR	Infrared
IVIVC	<i>in vitro-in vivo</i> Correlation
JMAK	Johnson, Mehl, Avrami and Kolmogorov
NMF	Non-negative Matrix Factorization
PAA	Polyacrylic Acid
PLM	Polarized Light Microscopy
ppm	Parts per Million
PVP	Polyvinyl Pyrrolidone
PXRD	Powder X-ray Diffraction
QbD	Quality by Design
RH	Relative Humidity

SDD	Spray Dried Dispersion
SHG	Second Harmonic Generation
SNR	Signal to Noise Ratio
SONICC	Second Order Nonlinear Optical Imaging for Chiral Crystals
ssNMR	Solid State Nuclear Magnetic Resonance
TPE-UVF	Two Photon Excited UV-Fluorescence
TRHA	Temperature Relative Humidity Array
UV	Ultraviolet
XFEL	X-ray Free Electron Laser
XRD	X-ray diffraction

ABSTRACT

Author: Sarkar, Sreya. PhD

Institution: Purdue University

Degree Received: August 2019

Title: Nonlinear Optical Microscopy for Pharmaceutical Formulation Development

Committee Chair: Garth Simpson

The unique symmetry requirements of second harmonic generation (SHG) provide exquisite selectivity to chiral crystals, enabling independent quantitative modeling of the nucleation and crystal growth of active pharmaceutical ingredients (APIs) within amorphous solid dispersions (ASDs) during accelerated in situ stability testing, and in vitro dissolution testing. ASDs, in which an API is maintained in an amorphous state within a polymer matrix, are finding increasing use to address solubility limitations of small-molecule APIs. SHG microscopy yielded limits of detection for ritonavir crystals as low as 10 ppm, which is about two orders of magnitude lower than other methods currently available for crystallinity detection in ASDs. The quantitative capabilities of SHG analysis were substantially improved further while simultaneously dramatically reducing the total sample volume and storage burden through in situ analysis. Single particle tracking of crystal growth performed in situ enabled substantial improvements in the signal to noise ratio (SNR) for recovered crystal nucleation and growth rates by nonlinear optical microscopy. Upon dissolution, the presence of solubilizing additives in biorelevant media greatly affected the generation and stabilization of supersaturated solutions. SHG microscopy was found to enable the detection of crystals even in the highly turbid Ensure Plus® system. Analysis of the SHG micrographs clearly indicated that differences in the nucleation kinetics rather than growth rates dominated the overall trends in crystallinity. For weakly basic drugs, the fate of dissolution in fasted-state simulated intestinal fluid (FaSSIF, pH 6.5) varied with the ASDs drug loading, and was highly affected by the pre-exposure to the fasted-state simulated gastric fluid (FaSSGF, pH 1.6) medium, versus the dissolution in FaSSIF medium alone. The presence of crystals during the first stage of posaconazole ASDs dissolution in FaSSGF acted as nuclei for further crystallization in the later dissolution stage in FaSSIF. The results provide insights of better formulation prediction of poorly soluble drugs, as well as understanding origins of intraluminal absorption variability for such systems.

CHAPTER 1. INTRODUCTION

1.1 Enhancement of bioavailability by ASD

The conventional timeframe for a new drug approval starting from the drug discovery phase to the drug application phase is considered to be at least one or two decades long.¹ Involvement of several steps in between as well as significant complications related to each passing step to ensure maximal patient safety make the whole process prolonged. It is also apparent that the associated costs escalate with time. In a recent study, it has been estimated that \$2.87 billion and 11 years is the average requirement to establish an active pharmaceutical ingredient (API) from discovery phase for market sale, and preclinical work requires an estimated \$450 million in out-of-pocket costs.¹ Following the rational drug design, in the preclinical development phase utilization of state-of-the-art analytical techniques to solve crucial measurement challenges can significantly lower the time required for developing effective formulations.

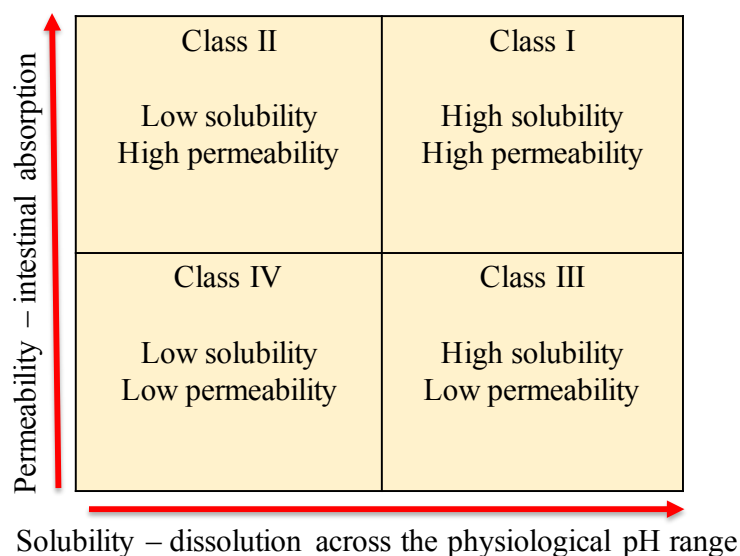


Figure 1.1. Biopharmaceutical classification system of drugs.

Among various possible dosage forms, oral dosage form is the most common one used for efficient drug delivery.² Oral formulation is easy to supervise in patients, as well as is the most patient-friendly dosage form, in which reductions in pill-load are balanced by ensuring sufficient bioavailability. Two key factors play vital roles when deciding bioavailability, solubility and

permeability of the drug product. Based on these two components, APIs can be divided into four classes, widely known as Biopharmaceutical Classification System (BCS),³ shown in Figure 1.1. High solubility and high permeability correspond to desirable release of the oral dosage form in the body, therefore showing higher bioavailability. As the solubility and permeability of the API decreases, chances of using the API in non-oral dosage form increases.⁴

For the past few decades, due to modern drug discovery strategies, the majority of the APIs have become more lipophilic, and of higher molecular weight, which hinder their aqueous solubilities.⁵ One of the most acknowledged strategy to increase the solubility of an API is forming an amorphous solid dispersion (ASD)^{6,7} of the drug in a polymer, which acts as the carrier matrix. The crystalline form of an API provides high purity, and physical as well as chemical stability as it has lower free energy due to its long-range-ordered molecular structure.⁸ Whereas, due to the short-range-ordered and long-range-disordered molecular structure of the amorphous form, it generally resides in a thermodynamically metastable zone, exhibiting higher free energy. Therefore, when the amorphous form of the API is cast into an amorphous polymer matrix to form the kinetically stabilized ASD, the amorphous API typically has significant thermodynamic driving force to revert back to the crystalline state (Figure 1.2).

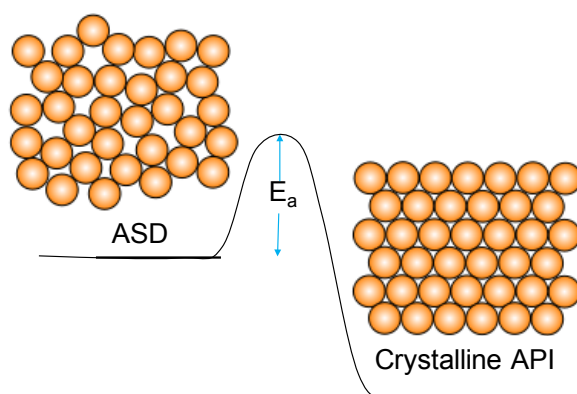


Figure 1.2. Schematic of relative free energies of amorphous versus crystalline states of API.

Factors affecting the stability of the amorphous drug in the ASD include environmental influences such as temperature, and relative humidity, preparation method, preparation conditions etc.⁹ The physical and chemical stability, solubility, dissolution rate etc. of the drug product are greatly affected by this conversion.¹⁰ Thus, it is extremely important to prevent any crystallization

from happening as well as to detect the presence of any residual crystallinity in the ASD as those can act as nuclei to expedite the further propagation of crystallization.^{11,12}

1.2 Physicochemical characterization of drug products by nonlinear optics

Numerous analytical techniques for assessing the physicochemical properties of ASDs include polarized light microscopy (PLM),¹³ X-ray powder diffraction (PXRD),¹⁴ differential scanning calorimetry (DSC),^{9,15} Raman spectroscopy,¹⁶ Fourier transform infrared spectroscopy (FTIR),¹⁷ and solid state nuclear magnetic resonance (ssNMR).¹⁸ PLM is one of the most common methods used for determining the presence of crystalline phase. Despite its widespread use, PLM can only provide qualitative information on optically transparent samples and is commonly complicated by interference from occlusions, contaminants, and crystalline excipients. As a consequence, PLM is challenging to integrate into fully automated quantitative analyses of crystallinity. PXRD is arguably the current “gold standard” for detecting trace crystallinity within the pharmaceutical industry but generally does not enable quantification at low crystallinity, takes several minutes for sample preparation/analysis, and requires several mg of material for analysis. Collectively, all of these conventional methods have relatively higher detection limit and significantly longer data acquisition time. If the drug loading in a life-saving oral medication is less than 1% (w/w percentage),¹⁹ the traditional techniques are not sensitive enough to detect any low level of crystallinity. Therefore, a fast-analytical method with low detection limit would help speedy identification of solutions to present-day challenges.

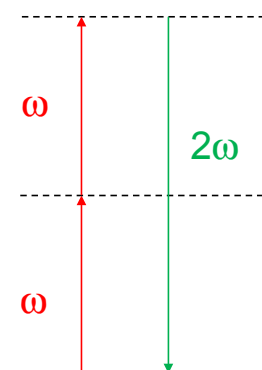


Figure 1.3. Jablonski diagram for second harmonic generation (SHG).

Nonlinear optics has recently gained traction in the pharmaceutical industry for sensitive detection and quantification of trace crystalline content within amorphous formulations.^{20,21} Second harmonic generation (SHG) describes the coherent conversion of light to twice the frequency (Figure 1.3), which is symmetry-forbidden in centrosymmetric media but allowed in assemblies of lower symmetry, including the large majority of noncentrosymmetric crystals.²² Chirality within the molecular building blocks of homochiral API crystals guarantees a noncentrosymmetric crystal. SHG provides a near background free measurement of the crystalline fraction of an ASD since the disordered, amorphous material will not produce coherent SHG. Due to the sensitivity and selectivity of SHG, routine measurements can be made with a limit of detection in the ppm regime.²³ Utilizing the sensitivity of SHG to crystalline content for identification of regions of interest, the detection limits for Raman and XRD have been lowered into the ppm regime as well.²⁴ The low limits of detection of SHG microscopy enabled quantification of crystallization kinetics in ASDs spanning a 4 orders of magnitude range in crystallinity. Altogether, second order nonlinear optical imaging for chiral crystals (SONICC) has the potential to quantitatively determine the pivotal attributes of drug products such as, nucleation events, crystal growth kinetics, crystalline versus amorphous content, polymorph discrimination etc. for pharmaceutical formulation development.^{23,25,26}

1.3 SHG microscopy for development of ASDs

Stability testing of drug substances and drug products are routinely performed in industries as per the US food and drug administration (FDA) guidelines.²⁷ Stability testing or stress testing informs the effect of environmental factors such as, temperature, relative humidity on the quality of the drug over a certain time period to evaluate bioavailability, efficacy, storage conditions, and shelf-life of the drug.²⁸ Apart from the external perturbations, intrinsic properties of the drug product including physical and chemical stability of the API and the excipients, composition of the dosage form, method of preparation etc. can also negatively affect the stability over time.²⁹ The time frames for these stability testing can extend up to months to years depending upon the conditions used for stress testing. To escalate the timeline, accelerated stability testing is often carried out at elevated temperature and relative humidity condition.³⁰ Accelerated stability testing provides comparable quality of information at much shorter time frame. The results of these studies are extremely important to effectively develop the successful formulation.

After the oral administration of the dosage form, it is also necessary to administer the behavior of the drug at *in vitro* conditions to predict its *in vivo* performance.³¹ *In vitro* dissolution studies are conducted at physiological conditions to evaluate solubilization, and release of the drug product across the gastro-intestinal tract.³² ASDs show higher dissolution rates, and they produce supersaturated solutions upon introduction to any aqueous medium, making them a desired formulation approach to enhance solubility and bioavailability.³³ Inherent characteristics of the drug product such as particle size, polymorph, physical and chemical stability, excipients, solubility of drug, drug loading as well as attributes of the medium of dissolution for example, volume, pH, co-solvents, enzyme, surfactant, presence of bile salts and phospholipids also influence the dissolution profile.³⁴ Use of dissolution media mimicking the composition and physicochemical characteristics of human gastrointestinal tract is therefore valuable.

1.4 Dissertation overview

The thesis will focus on utilization of nonlinear optics to inform pharmaceutical formulations by elucidating physical and chemical transformations at controlled conditions. The process of crystallization is central to most of the transformations happening here. The role of two key components for determining early stage crystallization events, detection of nuclei and evolution of crystal growth will be explained in detail.

In the works described in chapter 2, a large dynamic range with correspondingly low limits of detection for crystallinity was achieved by utilization of SHG microscopy during accelerated stability testing of ritonavir ASDs. The large dynamic range and access to the low levels of crystallinity at two different conditions, 50°C/75% RH and 40°C/75% RH enabled building of a kinetic model, which could be used to predict the relative stability and shelf life of the ASD at ambient conditions.²³

In chapter 3, the quantitative capabilities of SHG analysis were substantially improved further while simultaneously dramatically reducing the total sample volume and storage burden for accelerated stability testing through *in situ* analysis. A controlled environment for *in situ* stability testing (CEiST) was developed to leverage the sensitive, non-destructive analysis capabilities of SHG for continuous monitoring of individual crystallites during nucleogenesis and growth. The CEiST platform allowed for single particle tracking over hours to days under accelerated stability conditions typical for ASD analysis. Monitoring the same fields of view over

time lowers noise in determinations of the nucleation rates and crystal growth rates obtained from accelerated stability tests while simultaneously lowering the amount of sample required.

Chapter 4 describes disparities in the crystal growth kinetics for ritonavir crystallites seeded at the surface versus embedded in the bulk of a supersaturated copovidone ASD by SHG microscopy. “Sandwich” materials were prepared, in which sparsely prepared seeds of ritonavir single crystals were pressed between two identical ASD thin films to assess bulk crystallization rates. The sandwich materials were compared and contrasted with analogously prepared “open-faced” samples without the capping film to assess surface crystallization rates. Single particle analysis by SHG microscopy time-series during *in situ* crystallization showed one order of magnitude higher variation in average growth rates for surface particles than the embedded ones.

Chapter 5 introduces a modified particle counting algorithm correcting for particle-particle overlap of rod-like particles. First, the algorithm was applied to simulated SHG images, then it was used on the rod-like ritonavir particles formed during accelerated stability testing of ASDs prepared from different methods with variable crystallization kinetics.

Chapter 6 focuses on phase behavior of a poorly water-soluble drug, ezetimibe ASDs in different biorelevant media during *in vitro* dissolution testing.²⁵ The ASDs were prepared in different polymer matrices, namely, polyacrylic acid (PAA), polyvinyl pyrrolidone (PVP), and hydroxypropyl methylcellulose acetyl succinate (HPMC-AS) and the media employed for dissolution were, sodium phosphate buffer, fed-state simulated intestinal fluid (FeSSIF), and Ensure Plus®. Substantial variation in the phase behaviors and crystallization kinetics of different ASDs were observed in different dissolution media. Although crystal growth rates were similar across all cases, significant variances in nucleation rates played major role in driving overall crystallization kinetics. Quantitative analysis of supersaturation behaviors in highly turbid media was made possible due to high selectivity and sensitivity of SHG microscopy.

In chapter 7, role of pH shift was evaluated on drug release and phase separation of ASDs of a weakly-basic drug, posaconazole and Noxafil® tablets upon dissolution in two-stage media representing gastric (fasted-state simulated gastric fluid, FASSGF) and small intestinal conditions (fasted-state simulated intestinal fluid, FASSIF). Nucleation events emerging in the gastric compartment at lower pH promoted further crystallization in the intestinal compartment at higher pH, despite of initial generation of supersaturation.

Chapter 8 describes utilization of non-negative matrix factorization for isolating damage-free reflections in macromolecular synchrotron data collection. In this work, a “damage-free” set of reflections in macromolecular crystallography was mathematically isolated by non-negative matrix factorization (NMF) and used to recover the of the X-ray diffraction (XRD) pattern of the protein unaffected by X-ray-induced damage. Damage during diffraction data collection can have a significant impact on the quality of the recovered protein structures. Here, the native XRD pattern of tetragonal lysozyme prior to X-ray exposure was recovered. NMF identified multiple sequential perturbations and isolated the corresponding changes in the reflections from each. At room temperature, NMF enabled independent isolation of perturbations to the reflections from direct X-ray exposure versus diffusion of molecular radicals generated upon solvent exposure. Application of NMF during the room temperature damage mechanism helped in observing the firsthand effects of indirect X-ray radiation around the sample.

CHAPTER 2. SHG MICROSCOPY OF API NUCLEATION AND GROWTH

Reprinted (adapted) with permission from Song Z.*, Sarkar S.*, Vogt A. D., Danzer G. D., Smith C. J., Gualtieri E. J., Simpson G. J., Kinetic modeling of accelerated stability testing enabled by second harmonic generation microscopy, *Analytical Chemistry* **2018** 90 (7), 4406-4413.(*equal contribution). Copyright: American Chemical Society.

2.1 Introduction

ASDs are an attractive drug formulation strategy, in which casting the API into a glassy matrix with controlled dissolution kinetics leads to higher apparent solubilities and accelerated dissolution rates.⁶ However, the stability of ASDs affects the bioavailability of the API. If a significant fraction of an API spontaneously crystallized during preparation or storage, the effective dose may be lower than the intended dose. Furthermore, residual crystals present upon dissolution may serve as nuclei for re-crystallization following dissolution under conditions of supersaturation.³⁵ Extensive accelerated stability testing methods are currently performed to assess evaluation and detection of any trace crystallinity present in ASDs under stressed conditions, as stability testing under ambient conditions is prohibitively time-consuming.²⁷

In principle, kinetic modeling at elevated temperatures and humidity can be used to predict stability under ambient conditions, which is ultimately the defining property of interest.³⁶ Moreover, evolution of crystals from ASDs under stressed conditions can be independently and self-consistently modeled in terms of nucleation and diffusion-limited growth.³⁷ In turn, parameterized models for nucleation and growth allow prediction of time-dependent crystallization under ambient conditions.³⁸ However, in practice, this approach is often hindered by the relatively high limits of detection for crystallinity of most benchtop instruments. Current analytical methods being used routinely in pharmaceutical industries routinely only allow Boolean assessments with long measurement times, which can complicate integration with quality by design (QbD) principles.³⁹ Given the increased prominence of QbD methods in regulatory decision-making, improvements in the detailed understanding of stability can have a considerable impact in approvals processes.

As a consequence of the relatively high limits of detection of conventional analytical methods, most stability testing is currently performed with a Boolean pass/fail assessment that

serves little value for quantitative kinetic modeling for extrapolation to ambient conditions. Nonlinear optical imaging, specifically second harmonic generation (SHG) has proven to be a successful method in the pharmaceutical field for the sensitive detection of trace crystallization in amorphous systems.⁴⁰ While previous studies suggest nonlinear optical methods can be used for the detection of non-centrosymmetric crystals with high sensitivity, it has not yet been demonstrated as an analytical technique for accelerated stability testing of ASDs. In this work, accelerated stability testing has been carried out on a model ritonavir-ASD to determine the detection limits of SHG microscopy and assess the utility of the approach for informing kinetic modeling of crystal nucleation and growth. Specifically, the primary objective of the present work is the development of parameterized models for early-stage crystal nucleation and growth kinetics that can be used for quantitatively assessing the anticipated stability under ambient conditions.

2.2 Methods

Amorphous ritonavir milled extrudate samples were prepared in-house with 15% amorphous ritonavir (manufactured by AbbVie) and 85% copovidone (a commercial polyvinylpyrrolidone routinely used as a tablet binder).^{41,42} In brief, samples were prepared by placing powdered extrudates on the glass slides as a thin layer ($\sim 300\ \mu\text{m}$) over a sample area of $\sim 1\ \text{cm}^2$. For accelerated stability testing, samples were stressed at $50^\circ\text{C}/75\%$ relative humidity or $40^\circ\text{C}/75\%$ relative humidity. SHG images were used to observe the crystallization of stressed amorphous ritonavir at early times (0 hours – 24 hours).

SHG images were acquired by using a commercial SONICC (second-order nonlinear optical imaging of chiral crystals) microscope (Formulatrix, Inc.), modified in-house for compatibility with powders analysis. Specifically, the instrument was redesigned to allow epi-detection of SHG (details shown in Supporting information). The system is powered by a Fianium FemtoPower laser (1060 nm, 170 fs, 50 MHz). A resonant mirror (8 kHz) and a galvanometer mirror are used for beam scanning to generate SHG images. In this study, all of the SHG images were acquired with 350 mW excitation laser power at the sample and each field of view was $1925\ \mu\text{m} \times 1925\ \mu\text{m}$. For unstressed samples, the SHG signal was collected in the epi direction (i.e., back through the same objective used to deliver the infrared beam), as powders typically generate little signal in transmission due to optical scattering. For the ritonavir milled extrudates sample stressed at either 50°C or 40°C with 75% relative humidity, SHG signal was collected in

transmission direction because of its high transparency following a coalescence of the copovidone polymer. Two replicates of each sample were prepared, and three different positions of each sample were observed for a total of six fields of view obtained for each time-point. ImageJ was used to analyze the SHG images based on particle counting analysis as described previously.

2.3 Results and discussions

2.3.1 Low limit of detection for crystallinity during accelerated stability testing

Under the condition for accelerated stability testing at both 50°C/75% RH and 40°C/75% RH, crystal growth kinetics from the 15% drug loading (DL) amorphous ritonavir milled extrudate was recorded by collecting SHG images on a scheduled basis. 10 representative SHG images were shown in Figure 2.1. All of the images are shown with the same brightness scale for comparative purposes. It is worth noting that the SHG micrographs even at the earliest stages shown in the figure yield signals well above the noise floor of the instrument. The unstressed amorphous ritonavir milled extrudate samples were examined by collecting SHG signal in epi direction. The time-zero samples showed no detectable SHG, with the onset of detectable SHG at 5 hours for samples stressed at 50°C/75% RH and 40°C/75% RH.

The 15% DL amorphous ritonavir milled extrudate sample contained 15% amorphous ritonavir and 85% copovidone. Neither of the components is SHG-active. Ritonavir crystals were non-centrosymmetric and SHG active. For SHG images in Figure 2.1, the SHG-active areas represent ritonavir crystals. Based on the comparison of Figure 1A and Figure 1B, after the same stressed time, the milled extrudate stressed at 50°C/75% RH developed more ritonavir crystals with larger size than the sample stressed at 40°C/75% RH.

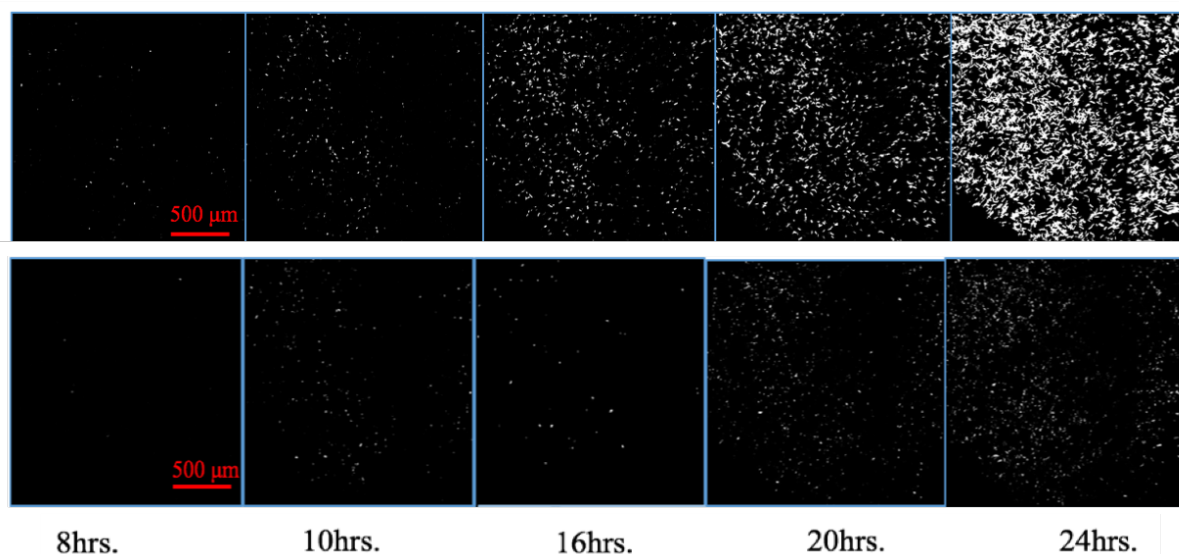


Figure 2.1. SHG images for time-dependent crystal growth in 15% DL ritonavir milled extrudate stressed in 50°C/75% RH and 40°C/75% RH chambers.

A particle counting approach was used to quantify crystallinity at level below 10%, described in detail elsewhere. In brief, the volume of each individual crystallite was estimated based on the cross-sectional area of the particle. This approach removes noise associated with variance in the SHG intensity from differences in crystal orientation. Bias introduced from particle overlap for crystallinities $>1\%$ was removed using a size-distribution dependent correction factor derived previously. Although the algorithm as described is formally derived assuming spherical particles, the aspect ratio ($\sim 3:1$) of the ritonavir particles is sufficiently low to allow reliable application of the method in the present study.

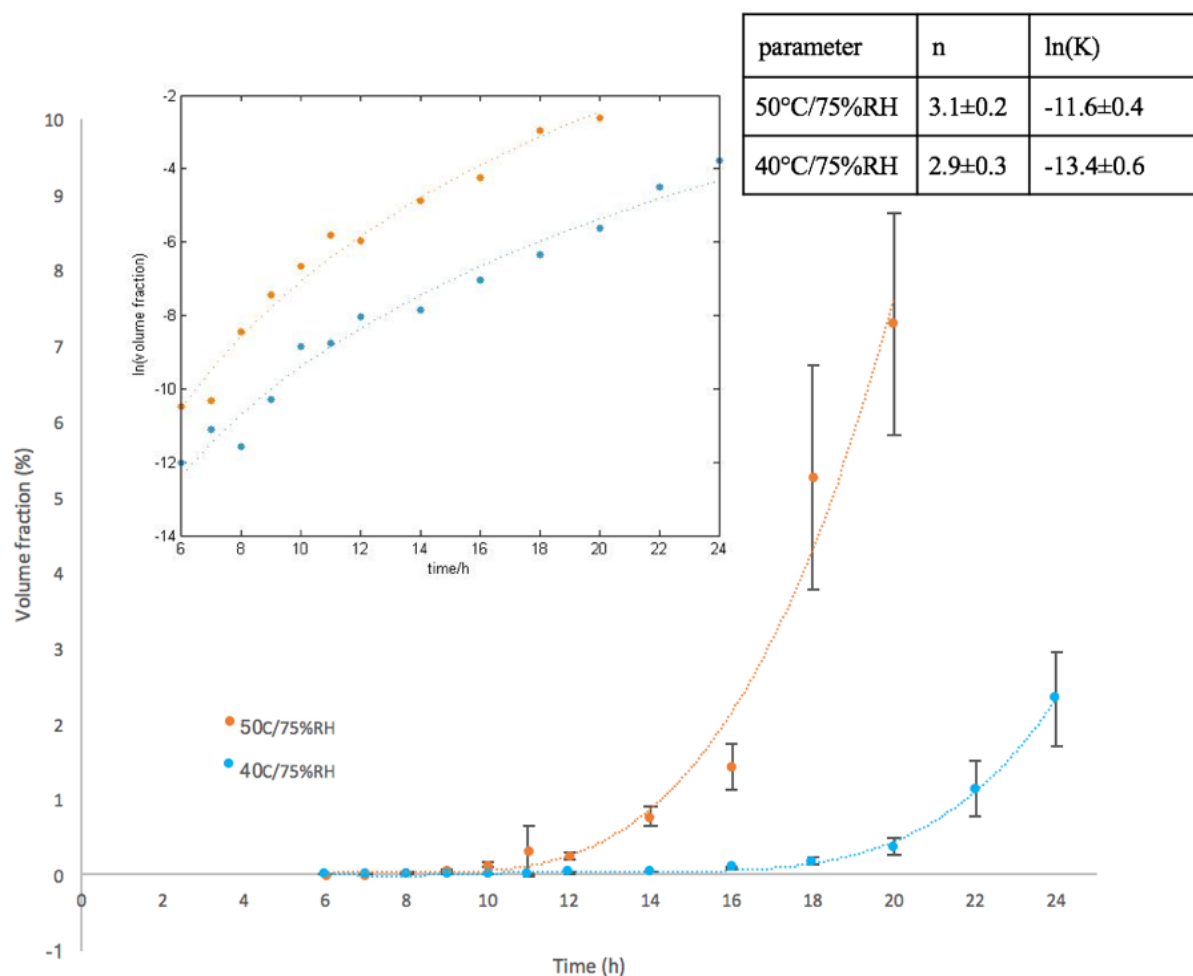


Figure 2.2. Percent volume fraction of crystallinity from amorphous ritonavir milled extrudate at different stress conditions with detection limit of 10 ppm (0.001%) of total drug loading.

Figure 2.2 shows the volume fraction of crystallinity from 15% DL amorphous ritonavir milled extrudate stressed at 50°C/75% RH (orange) or 40°C/75% RH (blue). SHG microscopy reduced the lower limits of detection of crystalline ritonavir in a milled extrudate powder to 10 ppm, which is approximately three orders of magnitude lower than alternative commonly available methods (DSC, PXRD, near IR). The growth rates are clearly not linear with each condition exhibiting a significant induction time, which is tentatively attributed to the stochastic nature of nucleation coupled with the need to generate particles large enough to generate significant SHG ($> \sim 1 \mu\text{m}$) for detection.

2.3.2 Theoretical background for kinetic modeling

Crystallization can be independently and self-consistently modeled in terms of nucleation and diffusion-limited growth.⁴³ Parameterized models for nucleation and fundamental models for growth allow prediction of time-dependent crystallization. The overall crystallization kinetics theory under isothermal condition can be described by JMAK theory (Johnson, Mehl, Avrami and Kolmogorov) in terms of volume fraction of the new phase considering nucleation and growth rates are constant throughout the transformation.^{Error! Reference source not found.,44} In this theory, the volume fraction of the new phase is proposed by Equation (2.1). t_0 represents induction time, which is defined as the first detectable time points.

$$\alpha(t - t_0) = 1 - \exp \left\{ -g \int_{t_0}^t I(t') \left[\int_{t'}^t U(t'') dt'' \right]^3 dt' \right\} \quad (2.1)$$

For spherical crystals shape-factor g is $4\pi/3$. Consideration of nucleation and growth rates being constant throughout the steady-state homogeneous nucleation, Equation (2.1) can be rewritten as Equation (2.2).

$$\alpha(t - t_0) = 1 - \exp \left[-\frac{gIU^3(t - t_0)^4}{4} \right] \quad (2.1)$$

The volume fraction of the transformed material can be given by the more general form of Avrami (JMAK) equation is given by Equation (2.3).

$$\alpha(t - t_0) = 1 - \exp(-K(t - t_0)^n) \quad (2.2)$$

In order to determine the constants K and n , Equation (3) can be rewritten as Equation (4). The nonlinear fitting by using Equations (2.3), (2.4) and the Avrami coefficient are shown in Figure 2.2.

$$\ln(-\ln(1 - \alpha)) = \ln K + n \ln(t - t_0) \quad (2.3)$$

The parameter n is called the Avrami coefficient and depends on both nucleation and crystal growth rates and thus from the formulas $N \propto (t - t_0)^k$ and $r \propto (t - t_0)^m$, which describe the variation in crystal number (N) and crystal size (r) with time. The Avrami coefficient can be given by the following Equation (2.5).

$$n = k + 3m \quad (2.4)$$

While the nucleation kinetics were largely insensitive to the difference in temperature over the regime investigated, the crystal growth kinetic exhibited a steep temperature-dependence. A general expression for the growth rate U is given in Equation (2.6), including both nucleation and

diffusion. In Equation (2.6), ΔG_v is the thermodynamic driving force per unit volume of crystal, a is an average (effective) size parameter of the ions building the crystalline phase, k_B is Boltzmann's constant and f is a dimensionless parameter describing the different growth modes. For the normal growth mechanism $f=1$. U is the crystal growth rate, which was the slope from the linear fitting in Figure 2.3 (D).

$$U = f \frac{D}{4a} \left[1 - \exp \left(-\frac{1}{2} \frac{\Delta G_v a^3}{k_B T} \right) \right] \quad (2.6)$$

In practice, the expression in Equation (2.6) can often be simplified if either diffusion limits the growth rate (in which case D dictates the overall kinetics) or if the Gibbs free energy term in the exponential represented by ΔG_v dictates the crystallization rate.⁴⁵ Since the supersaturation decreases with increasing temperature, growth rates would be expected to decrease at elevated temperatures for crystallization under thermodynamic control. For diffusion-limited growth, the opposite trend is anticipated, with faster nucleation and growth at elevated temperatures consistent with the observations. Under diffusion-limited growth conditions, Arrhenius parameters for diffusion allow predictions of growth at intermediate temperatures (and lower temperatures provided no phase transitions arise).⁴⁶

$$D = D_0 e^{-\frac{E_a}{k_B T}} \quad (2.7)$$

Arrhenius parameters for diffusion-limited crystal growth kinetics are shown in Figure 2.3, fit according to Equation (2.7). An estimate of the steady-state growth rate was generated from the latest five time points under each of the two stressed conditions explored, as they contained the least number of crystallites smaller than the lower limits of detection of the instrument. In this regime, the growth rates based on crystal size changes could be most confidently recorded. Based on the temperature-dependent crystal growth rate, the calculated activation energy of diffusion is 68.8 ± 4.3 kJ/mol, which is generally consistent with previously reported values for polymers.

Equation (2.5) suggests close relationships between the exponential parameters describing nucleation and growth, which can be tested from independent assessment of the rate of new particle nucleation and the rate of growth for crystals already established. In Figure 2.4, log-log plots of the nucleation rate recover the exponential parameter k from the slope, based on the relationship $N \propto (t-t_0)^k$. The induction time t_0 was 5 hours for samples stressed at 50°C/75% RH and 40°C/75% RH. Analogous operations can be performed to assess the growth rates from Figure 2.3 (C) based

on the mean of the histogram of particle sizes to extract the parameter m in Equation (2.5) from $r \propto (t-t_0)^m$. The slope results shown in Table 2.1 fit the Equation (2.5) and show internal consistency with JMAK model.

Table 2.1 Parameters in JMAK model.

	n	k	m
50°C/75%RH	3.1 ± 0.2	2.0 ± 0.2	0.4 ± 0.04
40°C/75%RH	2.9 ± 0.3	2.9 ± 0.2	0.07 ± 0.05

2.3.3 Nucleation and crystal growth kinetics

Steady-state nucleation rates are similar for both temperatures, with the primary difference in the induction time. Induction time is likely attributable to the timeframe required for crystals to grow to the level detectable by SHG, suggesting a relatively weak temperature dependence to nucleation in this temperature range and the differences in induction times dominated by differences in growth kinetics, consistent with the result in Figure 2.3.

A temperature-insensitive nucleation rate is consistent with a system in which both thermodynamics and kinetics in Equation (2.6) play significant roles in driving nucleation. As one decreases temperature, thermodynamics suggests a higher supersaturation and a corresponding increase in nucleation rate (according to classical nucleation theory). In contrast, diffusion models suggest higher rates with increasing temperature for mass-transport limited processes. A weak temperature dependence for nucleation suggests that both effects are significant, such that the decrease in nucleation rates from thermodynamics as supersaturation decreases is largely offset by an increase in nucleation rates from diffusion as temperature is increased.

It is worth comparing the results of the kinetic modeling of the SHG data to analogous modeling performed using conventional methods for crystallinity determination. The low limits of detection by SHG significantly reduce the induction time required to first observe onset of detectable crystallinity for integration into kinetic modeling. In the case of ritonavir in copovidone, limits of detection on the order of 0.5% crystallinity have been achieved in-house by PXRD. From inspection of Figure 2.2, this limit of detection would correspond to 4 data points in the 50°C crystallization trial and 2 data points in the 40°C trials over the same time frame for the experiment. With so few data points available, it would be challenging at best to assess the validity of any

particular model for predicting crystallization kinetics by PXRD alone. In principle, longer times could be devoted to monitoring crystallization (e.g., several days or longer). However, the modeling becomes more challenging as the concentration of solubilized drug and the corresponding degree of supersaturation changes significantly at higher crystallinity. In addition, the present study was performed under conditions leading to relatively rapid crystal formation. For stability testing performed approaching ambient conditions, the timeframes required for observation of crystallinity to inform modeling by conventional benchtop methods can become prohibitive for routine optimization of formulations.

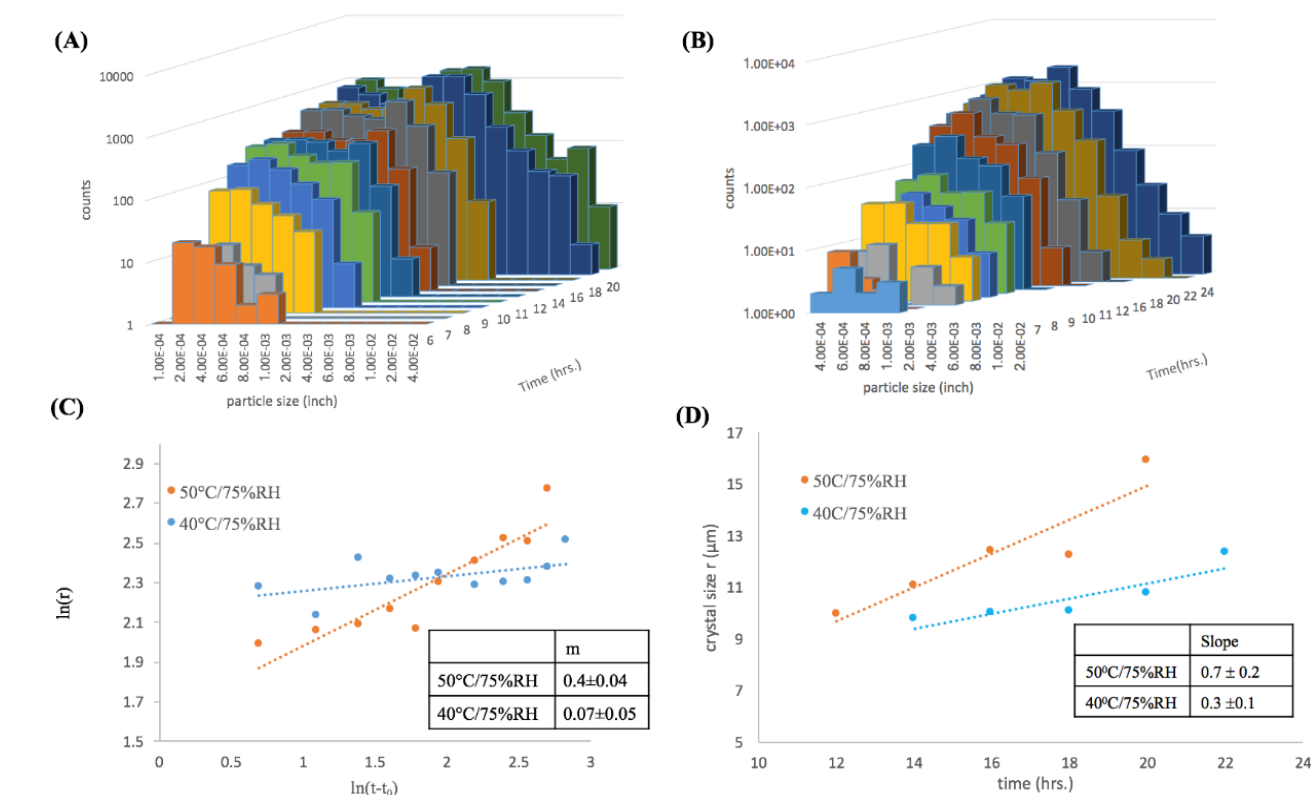


Figure 2.3. Crystal growth rate: Time-dependent ritonavir crystal particle size distribution histogram at (A) 50°C/75%RH, (B) 40°C/75%RH, (C) crystal growth rate depicted by $\ln(r)$ vs. $\ln(t-t_0)$ plot, (D) relationship between crystal growth rate and diffusion coefficient.

The importance of quantitative modeling for predictive behavior is particularly relevant to pharmaceutical analysis given the regulatory shifts toward quality by design (QbD) concepts for pharmaceutical characterization. QbD approaches rely on quantitative understanding of key aspects of the formulation. For ASDs, stability is arguably one of the most critical to evaluate.

Boolean pass/fail assessments of different formulations routinely performed with established instruments provide course-grained information that can complicate development of high-level predictive models for QbD assessments. In contrast, the rich information content available by SHG microscopy allows for the prediction of trends with substantially greater statistical confidence. By using parameterized models, the measurements also allow prediction of anticipated trends under alternative conditions (e.g., ambient). This predictive ability can benefit long-term stability assessments for which the direct measurements are prohibitively time-consuming during formulations optimization.

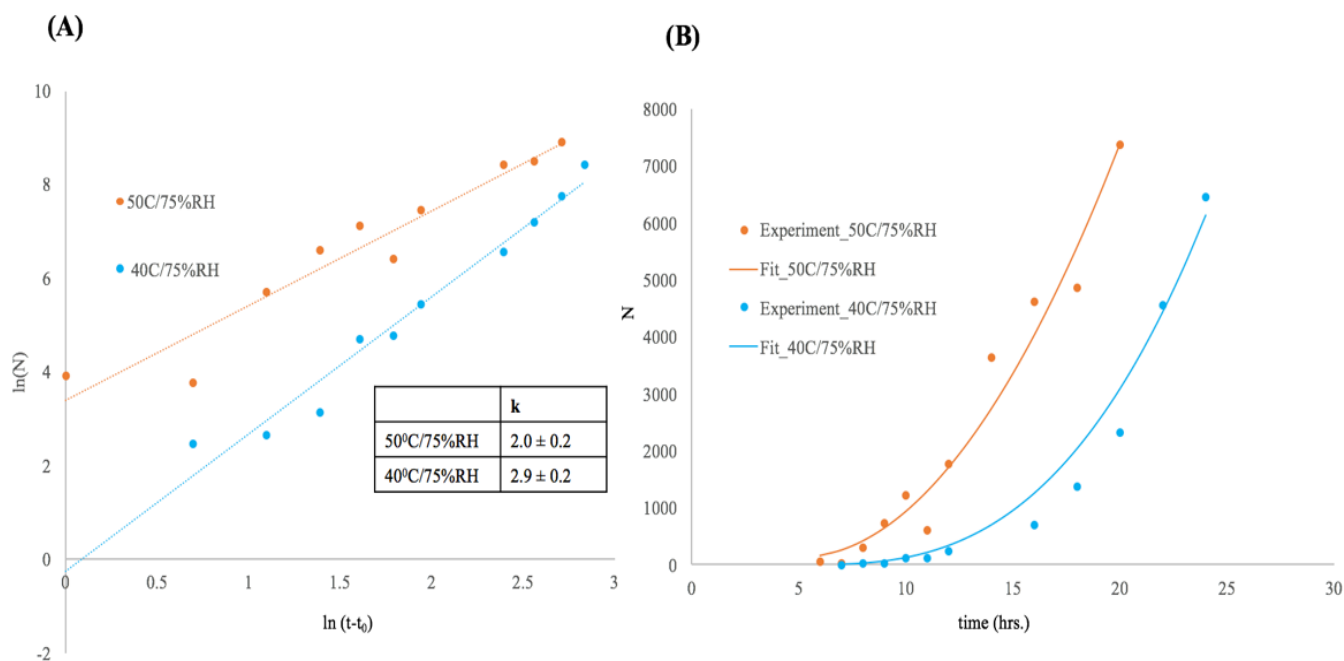


Figure 2.4. Kinetics of nucleation plotted logarithmically to determine the exponential order parameter k in Equation 2.5.

The SHG image analysis approach demonstrated in this work also has distinct practical advantages over established methods such as PLM. PLM can exhibit limits of detection well below 1% under favorable conditions. However, the image contrast for crystals is reduced by the presence of false-positive contributions from surface/edge effects in the sample, occlusions, scattering, etc. The high background and false-positives within the PLM images effectively render most automated particle counting image analysis approaches inapplicable, such that images are often interpreted manually. In contrast, SHG exhibits little detectable background from occlusions and the polymer matrix, such that the resulting images are directly compatible with well-established

and relatively simple automated image analysis algorithms. Compatibility with automated operation is clearly an attractive property for widespread adoption within the pharmaceutical community.

The particle counting approach described herein has the distinct advantage of being applicable irrespective of the crystal form of the SHG-active moiety or the need for calibration with a pure substance. Crystallinity is assessed entirely based on the calculated volume from individual particles. This capability is particularly advantageous in studies of pharmaceutical materials, as APIs often exhibit rich phase behavior with several crystal forms and/or polymorphs potentially accessible for crystal formation. Ritonavir is a particularly well-studied example of crystal polymorphism, in which the Form II polymorph exhibits significantly lower bioavailability

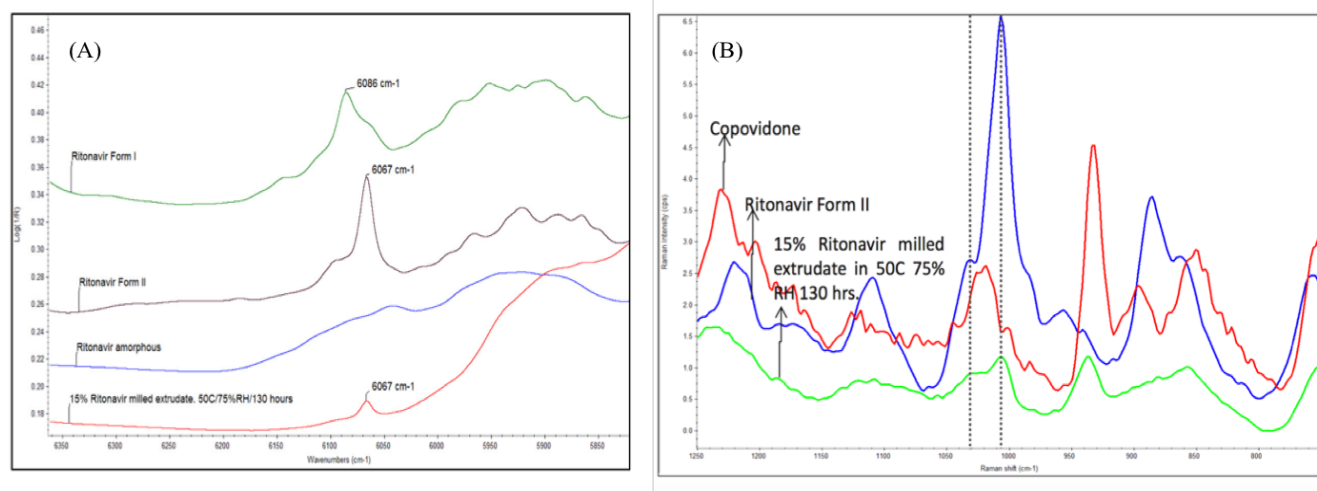


Figure 2.5. (A) Near IR spectra (B) Raman spectra of 15%DL ritonavir milled extrudate in 50°C/75% RH after 130 hrs. Both near-IR spectra and Raman spectra indicate the presence of ritonavir crystals in Form II.

in oral formulations relative to the metastable Form I. Confocal Raman and near infrared spectra acquired from later stages in the crystallization were consistent with the more stable Form II produced in the present study, which are shown in Figure 2.5. Such combined measurements highlight the advantages of coupling quantitative analysis approaches such as SHG with qualitatively rich spectroscopic characterization methods

2.4 Conclusions

In this study, SHG microscopy was used to develop analytical models for predicting the crystallization behavior of ritonavir in a model ASD formulation. The low (10 ppm) limit of detection of SHG microscopy extended the range of data to incorporate into the model by ~ 2 orders of magnitude lower compared to other routine benchtop methods for ritonavir crystallinity detection in ASDs, (e.g. DSC, PXRD). Most significantly, SHG extends the measurement into the low crystallinity regime, in which the analytical modeling is simplified by the assumption of a constant average concentration in the polymer. Image analysis of the SHG micrographs allowed separate evaluation of the contributions from both nucleation and growth in dictating the overall net kinetics of crystallization. The values of crystallinity were demonstrated to be consistent with the JMAK kinetic model. This information allows prediction of both the anticipated crystalline fraction as well as the crystalline number density and size distribution. The temperature-dependent changes in the SHG microscopy images allowed for determination of a diffusional activation energy, which in turn allowed for modeling to predict the anticipated kinetics under unique experimental conditions.

CHAPTER 3. IN SITU CRYSTAL GROWTH RATE DISTRIBUTIONS OF API BY SINGLE PARTICLE TRACKING

Adapted from manuscript submitted for AbbVie Inc. approval process with permission from Sarkar S., Song Z., Griffin S., Vogt A. D., Danzer G.D., Ruggles A., Simpson G.J., In situ Crystal Growth Rate Distributions of Active Pharmaceutical Ingredients.

3.1 Introduction

Production of amorphous solid dispersions (ASDs) offers a broadly applicable approach for kinetically circumventing solubility limitations of poorly soluble active pharmaceutical ingredients (APIs).⁷ When optimizing a polymer/excipient/API cocktail for preparing final dosage forms, one critical consideration is the long-term stability of the API within the ASD. Concentrating the API in the ASD to minimize the total mass load of the final dosage form is balanced by a desire to also reduce the chances of API nucleation and crystallization during storage of the ASD. For poorly soluble APIs, the crystalline form often exhibits negligible bioavailability, passing through the digestive tract for oral final dosage forms. In intravital formulations, residual insoluble API particulates can pose additional risks from inducing foreign body embolism.^{24,47,48,49} For these reasons, stability testing is widely used to inform the optimization of final dosage forms. High throughput testing requires a host of different test materials, multiple replicates of which at multiple time points are required for stability assessment over long timeframes (up to year-long timeframes). The high throughput, high sampling rate, and long incubation times (weeks to months) can significantly complicate sample preparation and storage capacities even when using accelerated conditions.

The duration of stability testing is ultimately dictated by the sensitivity with which crystal formation can be quantified for informing kinetic modeling, with a suite of methods currently brought to bear to address this measurement challenge. A large dynamic range with correspondingly low limits of detection has multiple benefits in accelerated stability testing, including: i) improved statistical confidence in kinetics parameters, ii) simplified kinetic modeling without the need to account for depletion effects, iii) compatibility with low API-load ASDs, iv) reduced volumes for sample storage during testing, and v) reduction in the timeframe necessary for decision-making in stability assessments. For the majority of the methods routinely used for

API analysis, limits of detection are on the order of a fraction of a percent, providing a relatively narrow dynamic range in crystalline API detection; in some cases, the total drug loading may only be on the order of a few percent.

In addition to the limited dynamic range, the majority of the common analysis tools probe only ensemble-average behaviors, masking possible intrinsic heterogeneity in crystal nucleation and growth kinetics. For example, it is well established that the nucleation and growth kinetics can differ substantially for crystals generated on the surfaces of ASD particles relative to the bulk.^{50,51} Even in homogeneous media, subtle differences in local environment can produce variance in crystal growth rates.⁵² The impact of this variance in growth kinetics on subsequent performance remains unresolved, due in part to the dearth of methods currently available to quantitatively inform the inherent variation in single-particle growth kinetics.

Second harmonic generation (SHG) microscopy has the potential to provide the limits of detection required for investigating single-particle growth kinetics and fill this knowledge gap. SHG provides a near background free measurement of the crystalline fraction of an ASD since the disordered, amorphous material will not produce coherent SHG. The low limits of detection of SHG microscopy enabled quantification of crystallization kinetics in ASDs spanning a 4 order of magnitude range in crystallinity.^{53,23}

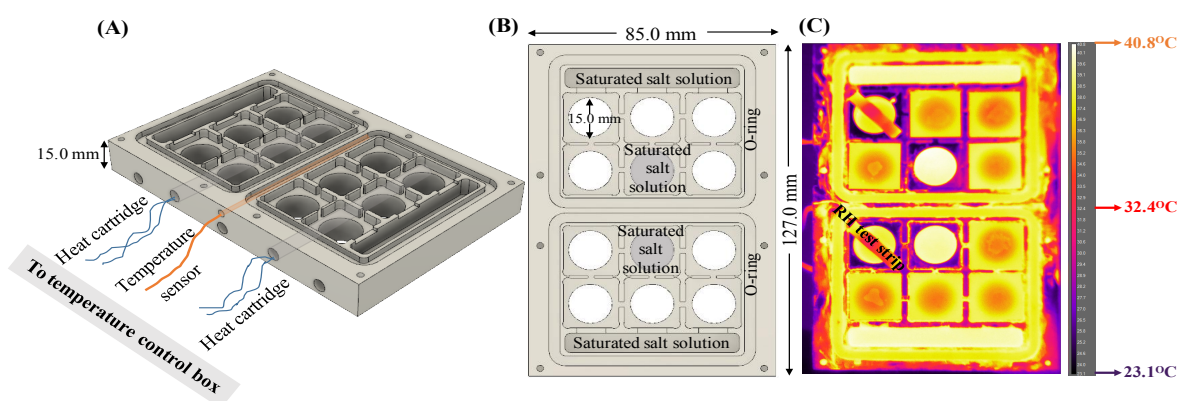


Figure 3.1. (A), (B) CEiST design, (C) IR thermal image of CEiST for validation of set temperature at 40°C.

In this work, the quantitative capabilities of SHG analysis are substantially improved further while simultaneously dramatically reducing the total sample volume and storage burden through *in situ* analysis. A controlled environment for *in situ* stability testing (CEiST) was developed to

leverage the sensitive, non-destructive analysis capabilities of SHG for continuous monitoring of individual crystallites during nucleogenesis and growth. The CEiST platform allowed for single particle tracking over hours to days under accelerated stability conditions typical for ASD analysis. Monitoring the same fields of view over time lowers noise in determinations of the nucleation rates and crystal growth rates obtained from accelerated stability tests while simultaneously lowering the amount of sample required.

3.2 Methods

ASD samples of ritonavir (15%), sorbitan monolaurate (10%), copovidone (74%), and colloidal silicon dioxide (1%) were prepared by AbbVie, prepared as spray dried dispersions (SDDd) and hot melt extrudates (HMEs). Samples without the sorbitan monolaurate were also made where the copovidone weight percent was increased to 84%. HME samples were milled to prior to use. All powder samples were placed into the CEiST chamber or into a standard stability chamber as thin layers ($\sim 300\ \mu\text{m}$).

3.2.1 Design of the *in-situ* platform

The CEiST's design is shown in Figure 3.1. The CEiST has two sections separated by greased O-rings that can be kept at different RHs depending on the saturated salt solution put into the reservoirs. Both compartments of the device were kept at an elevated RH of 75% through all experiments by using a saturated NaCl solution. The RH in each compartment of the CEiST was validated using reversible Moisture Indicator strips (Indigo Instruments, 33813-2080). The temperature was controlled by using two Tempco low density cartridge heaters (LDC00003) placed at different locations on the CEiST and a thermocouple in the center for feedback control by a custom controller built by the Johnathan Amy Facility at Purdue, depicted in Figure 3.1 (A). An IR thermal image of the CEiST in Figure 3.1 (C) confirms uniform temperature within $\pm 2^\circ\text{C}$ of the set point temperature. Samples were placed onto cover slips and then onto one of the ten wells within the CEiST. For comparative purpose, a standard stability chamber was made by placing saturated sodium chloride solution into the bottom of a desiccator wrapped in heat tape. The temperature of the entire chamber was monitored by thermocouple feedback.

Accelerated stability tests were performed using a SONICC microscope from Formulatrix (Bedford MA) for SHG imaging that was modified in house for epi detection. For the *in-situ*

stability testing, samples in the CEiST chamber were maintained an elevated temperature and humidity during SHG imaging. For samples maintained in the standard stability chamber, aliquots were sampled at select time points, analyzed by SHG under ambient conditions, and then discarded. The time from stability chamber removal through testing was about 10 minutes. Experiments were performed using 350 mW excitation laser power and 894 ms exposure time, repeated every hour (duty cycle of 2.8×10^{-4}). SHG was measured in the transmission direction due to the high transparency of samples in the CEiST through deliquescence of the ASD. SHG was collected in the epi direction for powdered samples before being subjected to elevated temperature and humidity. For samples within the standard chamber, three fields of view were used for each time point. For samples within the CEiST, several fields of view were selected from each of 3 wells prepared for each ASD.

3.3 Results and discussions

3.3.1 Validation of the *in-situ* platform

The performance of CEiST was evaluated relative to a conventional temperature and humidity-controlled chamber through side-by-side comparisons of accelerated stability testing of

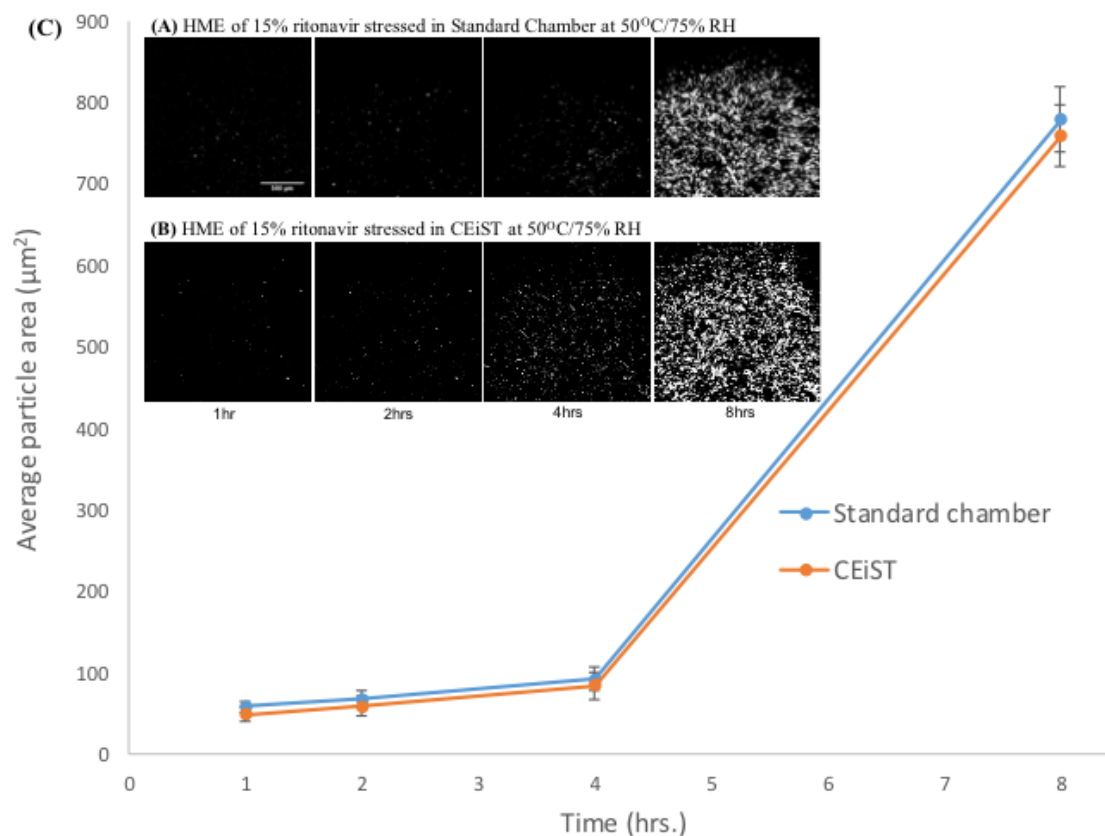


Figure 3.2. SHG images for time-dependent crystal growth of 15% HME ritonavir in (A) standard chamber, and in (B) CEiST. (C) The plot for average particle areas shows good agreement between the two different methods.

15% DL (w/w) ritonavir ASDs with HME at 50°C/75%RH, the results of which are summarized in Figure 3.2. The amorphous excipients present in the HME ASDs did not produce significant

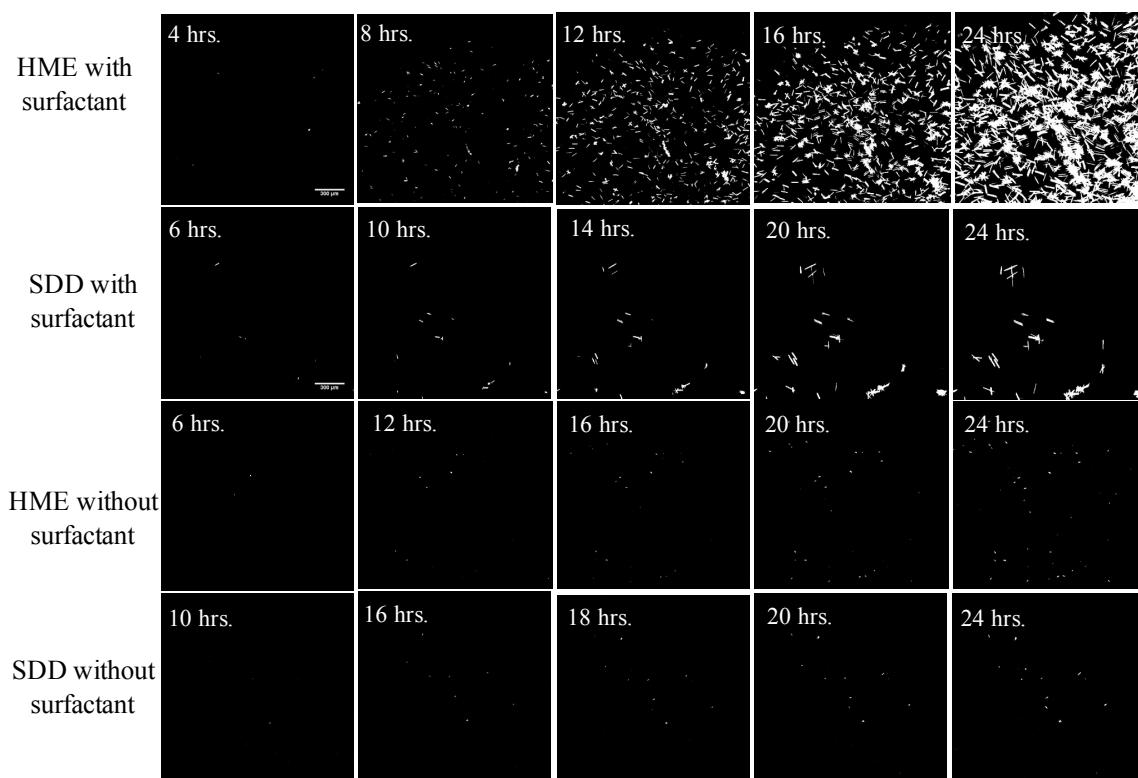


Figure 3.3. Time dependent SHG micrographs of 15% ritonavir ASDs stressed in CEiST at 50°C/75%RH.

coherent SHG signal. In contrast, ritonavir crystals adopt an SHG-active non-centrosymmetric lattice upon crystallization, enabling selective detection of crystalline ritonavir in HME ASDs using a particle counting algorithm. SHG images at four representative time points are shown in Figure 3.2 (A) for ASDs stored in a standard chamber at elevated temperature and humidity, and Figure 3.2 (B) for ASDs stored in the CEiST under identical target conditions. For quantitative comparison of ritonavir crystallization between the two platforms, the average crystal area at each time point was recovered by particle counting, shown in Figure 3.2 (C). The error bars in Figure 3.2 (C) represent the standard deviations of three fields of view for each time point. The SHG micrographs and the average crystal areas observed for both the standard chamber and the CEiST platform were in excellent agreement, suggesting that the conditions produced in the CEiST platform are representative of those experienced in conventional temperature and humidity-controlled chambers.

3.3.2 SHG imaging during *in situ* accelerated stability testing

Using the CEiST platform, 10 trials of *in situ* accelerated stability testing were run in parallel for ritonavir crystallization in different ASDs at 50°C and 75% RH. The ASDs were prepared with different components and different manufacturing techniques (see Experimental Methods). The ASD powder samples were examined by SHG microscopy and initially showed no detectable epi-SHG signal (i.e., no continuous regions of interest with at least 3 contiguous pixels of at least 3 counts). From previous studies using SHG to interrogate ASDs, this criterion corresponds to a lower limit of detection of 10 ppm crystallinity, indicating that the initial crystallinity in all cases was less than this lower limit of detection.

The SHG images and corresponding bright field images were automatically collected every hour starting from 0 to 48 hours. Four sets of representative SHG images at five different time points are shown in Figure 3.3. All of the images are shown with the same brightness scale for comparison. Based on the time-dependent SHG images, the incorporation of surfactant (span 20) increased the ritonavir nucleation rate and crystal growth rate in ASDs. In this case, the addition of span 20 resulted in more crystals and larger crystal size in accelerated stability testing, consistent with the presence of span 20 significantly reducing the stability of ritonavir against crystal formation in both hot melt extruded and spray dried ASDs. Compared with SDD ASDs, HME samples showed a greater number of crystals and lower induction times in the accelerated stability testing.

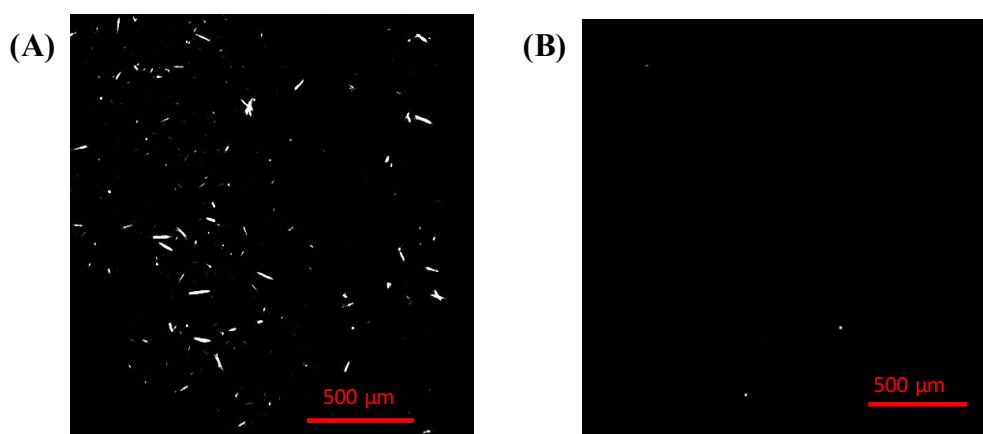


Figure 3.4. (A) Sample taken out of 50°C/75% RH standard chamber at every hour and stayed in room temperature for 15 min each time, (B) sample stayed in 50°C/75% RH standard chamber for 5 hours directly.

When accelerated stability testing was performed by using the standard temperature and humidity control chamber, the sample was taken out of the controlled environment to enable SHG

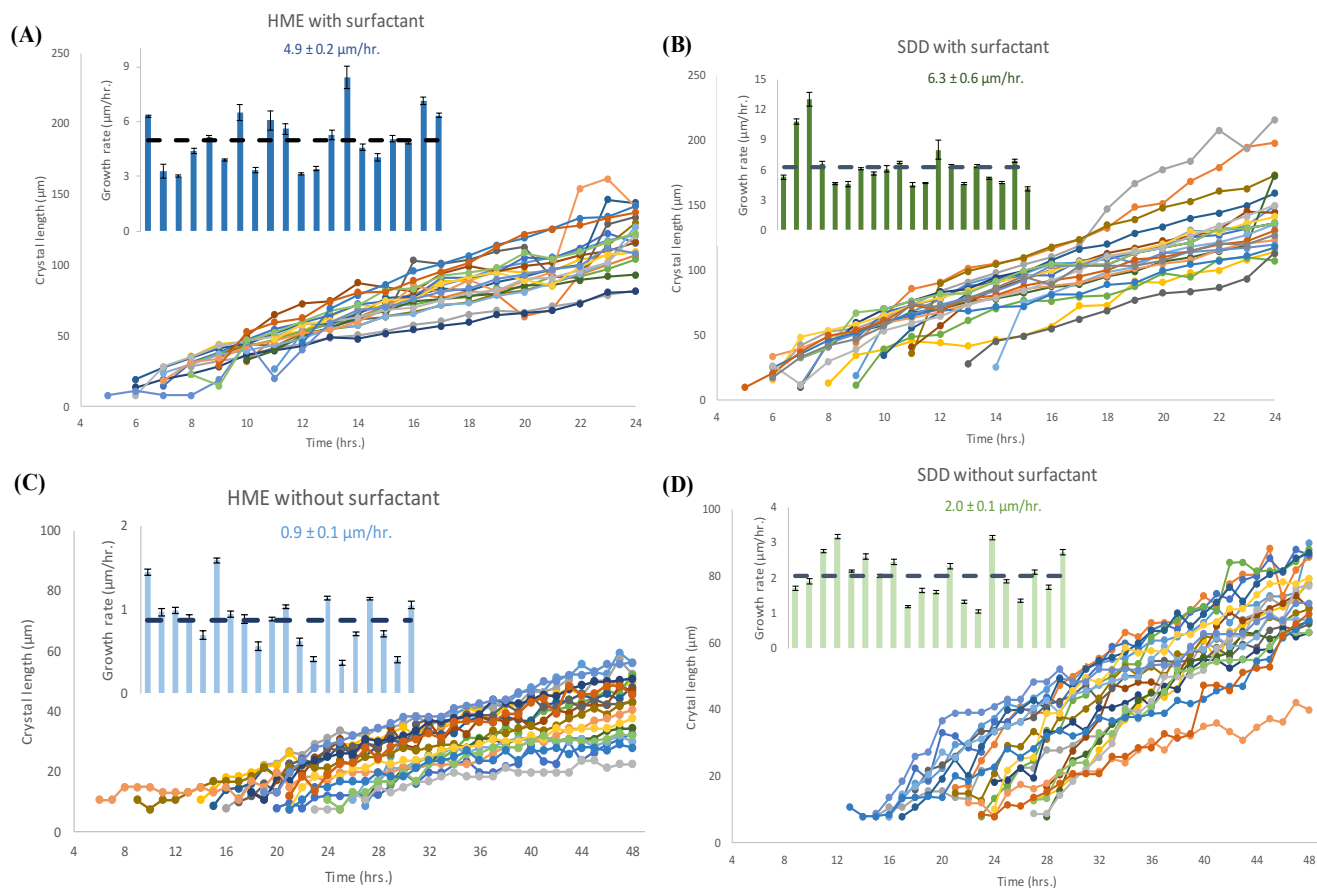


Figure 3.5. Individual crystal growth distribution in (A) HME with surfactant, (B) SDD with surfactant, (C) HME without surfactant, and (D) SDD without surfactant. Each plot has 20 different crystals tracked along the entire time trace and selected from different FOVs. The inset in each plot shows the dispersion in growth rates with the average growth rates shown in each plot as dashed line.

imaging under ambient conditions. Since temperature and humidity cycling can significantly change the crystallization kinetics (Figure 3.3), all the samples using the standard chamber were discarded following SHG imaging. The perturbations associated with temperature cycling are attributed to a two-step process: i) increase in supersaturation upon cooling to room temperature, resulting in increased nucleation rate, followed by ii) increased diffusion upon return to elevated temperature and humidity, resulting in increased crystal growth rates. Multiple aliquots of sample were therefore required to collect images at different time points using conventional stability

chambers to avoid kinetic artifacts from temperature cycling. This practice was in stark contrast to measurements performed using the CEiST system, which supported continuous monitoring of the same fields of view within a sample under controlled conditions.

3.3.3 Single particle tracking

For each sample, single-particle tracking was performed to monitor the growth rates of individual particles, representative results of which are shown in Figure 3.5 (A), (B), (C) and (D), selected from 4-6 different fields of view. The long axes of the needle-like ritonavir crystals (Form II) were used to quantify crystal size. The dispersion in crystal growth rates is shown in the inset plots of Figure 3.5. For individual crystals, error bars in the growth rates were assessed from the standard error of the slope of crystal size versus time. From inspection of the histograms of single crystal growth rates and the standard errors, it is clear that the dispersion in growth rates exceeds experimental uncertainties, and therefore reflects an intrinsic diversity in single crystal growth kinetics within the samples.

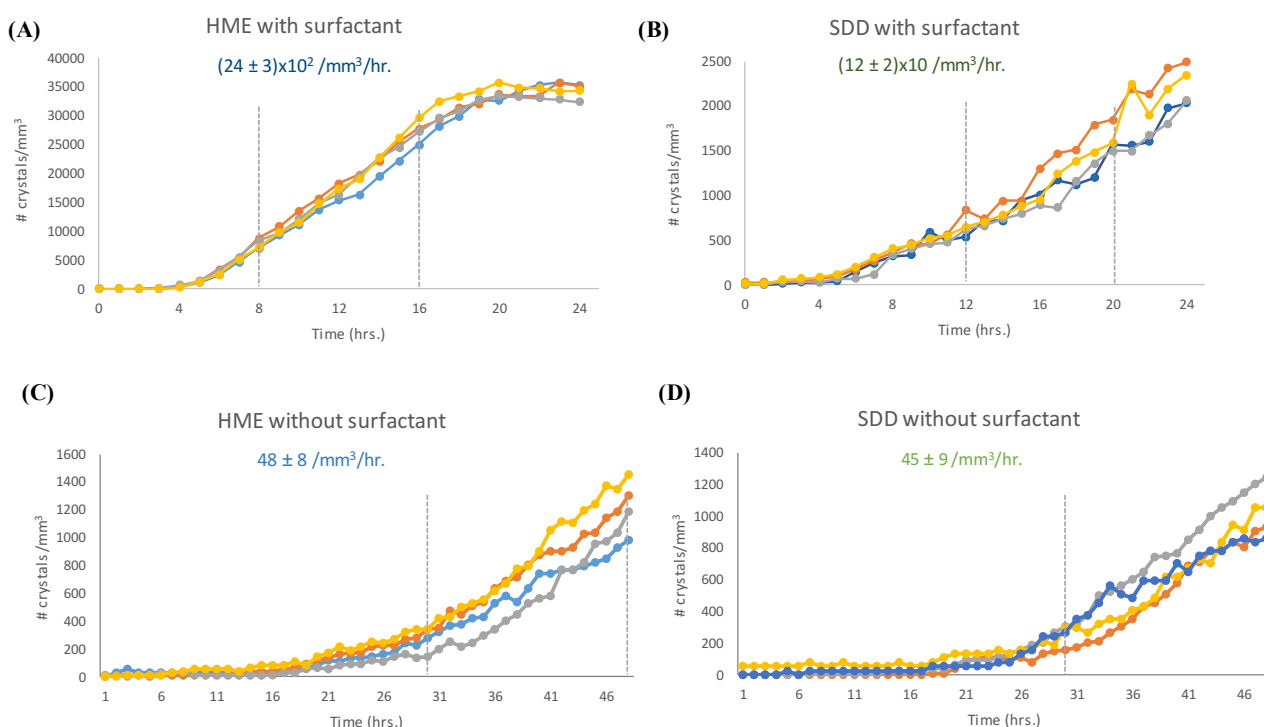


Figure 3.6. Average nucleation rates for (A) HME with surfactant, (B) SDD with surfactant, (C) HME without surfactant, and (D) SDD without surfactant.

Single-particle tracking enabled by the CEiST platform provided substantial signal to noise benefits in nucleation kinetics as well. The average nucleation rates were found from the linear growth regime shown in Figure 3.6 (A), (B), (C) and (D) by linear fitting of nucleation events from four different fields of view. The uncertainties reported in each plot arise from the variabilities of the fields of view. The linear region for fitting was marked by the dashed line. The nucleation rate in HME ASDs in Figure 3.6 (A) is one order of magnitude higher than in SDD shown in Figure 3.6 (B), in presence of 10% span 20 in the ASDs. The residual nuclei present in HME ASDs might be responsible for producing this higher nucleation rate. However, without the presence of span 20, the ritonavir nucleation rates are similar in both HME and SDD.

The substantial improvement in signal to noise for nucleation rate determination in CEiST can be understood considering the Poisson statistics associated with crystal genesis in combination with the sensitivity of SHG imaging to support single particle tracking. Nucleation rates using a standard stability chamber were calculated from the differences in the number of crystals between multiple independent samples analyzed at different time-points. Because each sample is statistically independent, the number of crystals in any given field of view is given by a Poisson-distribution. As a result, the nucleation rate is generated from the difference between two Poisson-distributed numbers acquired at different time-points. In the linear kinetics regime, the number of previously nucleated crystals contributes to the uncertainty in the number of new particles, rapidly degrading the precision to which the number of new particles can be determined based on Poisson statistics. In contrast, the nucleation rates in the CEiST chamber were calculated from the differences in the numbers of new crystals *within the same single FoV*, removing all statistical uncertainties regarding the number of pre-existing crystals. As such, uncertainty in the nucleation rate is defined only by the Poisson statistics for the number of new particles within a given FoV. The signal to noise advantage associated with nucleation rates determined from analysis of single samples versus stochastic sampling is shown in Figure 3.7. Following the initial onset of nucleation, Poisson-distributed uncertainties in the differences in particle numbers between independent samples rapidly degrade the precision to which nucleation rates can be determined. However, no such statistical loss in SNR is expected from repeated analysis of a single FoV.

Interestingly, the SNR improvement afforded by single particle tracking pairing SHG microscopy with the CEiST platform provides a simultaneous advantage in reducing sample volume requirements. Stability testing of pharmaceutical formulations can extend over several

weeks, or months, or even years, for each of potentially many different formulation candidates. The temperature cycling complication coupled with the Poisson statistics limitations associated with crystal analysis pose cost challenges associated with archiving large volumes of identical replicate samples in controlled environments for testing times spanning multiple months or years. Continuous *in situ* monitoring of a single field of view over the entire time-course of a stability assessment (e.g., by SHG microscopy) provides reduction in sample volume requirements proportional to the number of time-points used for kinetics assessments. For example, in the present study with up to 48 time-points recorded for a given sample, the total assay volume is correspondingly reduced up to 48-fold.

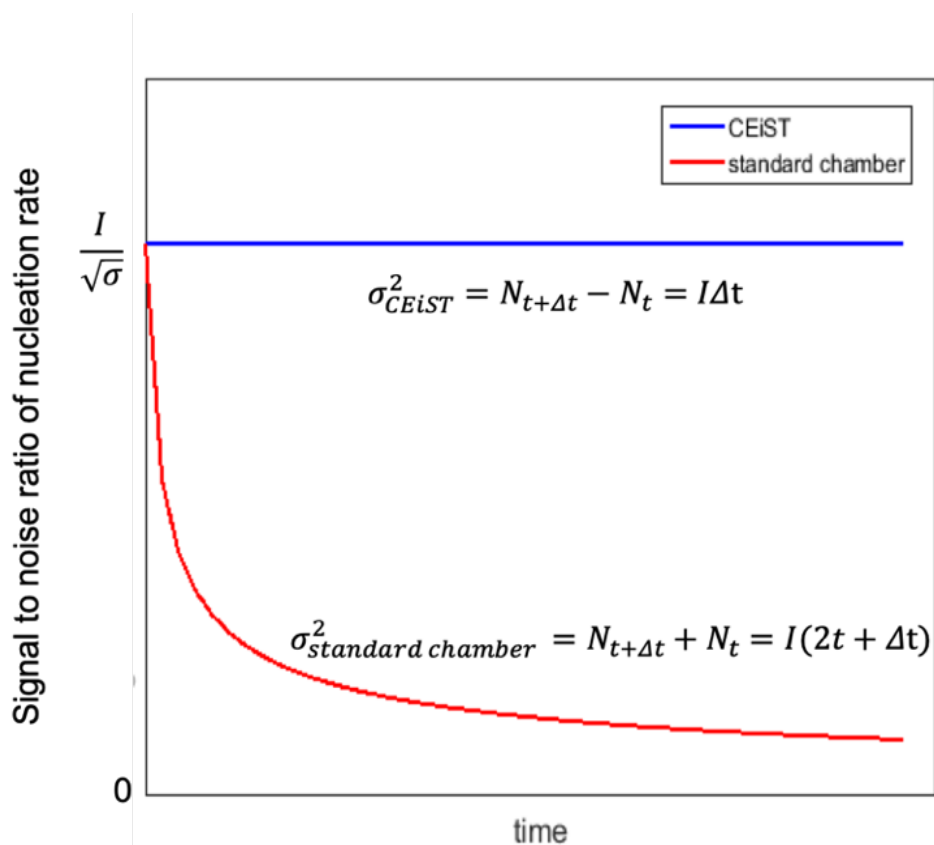


Figure 3.7. Anticipated signal to noise ratio of nucleation rate for *in situ* vs conventional stability testing based on the Poisson statistics of crystal counting. I: nucleation rate, σ : uncertainty of nucleation rate based on Poisson statistics, N_t : number of crystals at time t.

The collective results of the single-particle tracking experiments provide insights into the molecular connections between stability, method of preparation, and composition of ASDs. The

higher observed crystal growth rate in SDD relative to HME ASDs suggests a fundamental difference in the molecular diffusion constant within the matrices, as the ritonavir growth rate is diffusion limited in this regime. The origin of this disparity in diffusion constants may potentially be attributed to the desolvation step in SDD generation, which may potentially produce a higher density of microscopic voids in the final products and higher molecular diffusion. Presence of Span 20 in ASD formulations of ritonavir contributes to processability, but dramatically increases molecular diffusion, with corresponding increases in single crystal growth rates. Specifically, the surfactant, span 20 increased the crystal growth rate by ~5 times for HME and ~3 times for SDD. The surfactant, span 20 induced ~50-fold and ~20-fold change in nucleation rates for HME and SDD, respectively. The nucleation kinetics are also distinctly different between SDD and HME ASDs in the presence of span 20, with nucleation rates were about an order of magnitude higher in HME. This difference in nucleation rate may potentially arise from the presence of residual nuclei within the melt in the HME materials from incomplete melting. Optimization of conditions for HME preparation strikes a balance between the competing desires for higher temperatures to remove residual nuclei and lower temperatures to minimize pyrolysis. As such, the presence of trace residual nuclei within the HME is arguably more likely than in the SDD materials, consistent with the observations made by single particle tracking by SHG microscopy.

Recovery of the crystal growth rate distribution from single particle tracking suggests the presence of subtle but significant heterogeneity within the samples at microscopic scales. In all of the cases, the differences between the crystal growth rates of single crystals within individual fields of view are beyond the errors from fitting. This intrinsic variability in growth rates for nominally identical crystal forms suggests subtle differences in local diffusion rates, which in turn indicates heterogeneity in local structure within the surrounding matrix. The growth rate dispersion might result from subtle variation in local density, hydrophobicity, chemical composition, etc. The diversity in growth rates, and correspondingly diversity in local environments is similar between different formulations.

3.4 Conclusions

The CEiST platform developed in this work enabled single particle tracking during accelerated stability testing of ritonavir ASDs by SHG microscopy. The high selectivity of SHG to crystalline content provides high-contrast images over a large dynamic range of crystallinity for

kinetics analysis. The advantage of monitoring the same field of view over time facilitated substantial signal to noise improvements for nucleation and growth rate assessments, supported single-particle tracking, and reduced the sample volume requirements by ~50 fold. From the single-particle tracking measurements by SHG microscopy, the heterogeneity in crystal growth rates within the ASDs suggests subtle but non-negligible local diversity in physical and/or chemical characteristics of the sample.

CHAPTER 4. DISPARITIES IN CRYSTALLIZATION KINETICS OF BULK VERSUS SURFACE CRYSTALS WITHIN ASD FILMS

4.1 Introduction

The shelf-lives of final dosage forms containing ASDs are often dictated by the rates of API crystallization.⁵⁴ Any trace amount of crystallinity can act as a source of nucleation, which can further promote crystal growth, thus accelerating the overall crystallization kinetics.⁵⁵ During stability testing, analysis of crystallization kinetics may be biased from differences in nucleation and growth rates at the surface versus in the bulk of the material.^{56,57} Therefore, methods that can discriminate between surface and bulk rates could provide a more cohesive and predictive framework.^{58,59} However, most of the current methods do not possess sufficient penetration depth and sensitivity to measure crystallinity within bulk sample.

SHG microscopy is the most potential to attract attention in this case due to its high sensitivity and selectivity.⁶⁰ Coupling the capabilities of SHG microscopy with the *in situ* measurements from the CEiST platform (described in Chapter 3), enable study of growth rate distributions of seeded needle-shaped ritonavir crystals in the bulk versus on the surface. Nucleation and growth rates are likely to vary for particles at surfaces versus buried in the bulk. However, quantitative assessment of the differences in crystallization kinetics is complicated by challenges associated with isolation of a particular contribution in complex ASD assemblies.

In the present study, “sandwich” materials were prepared, in which sparsely prepared seeds of ritonavir single crystals were pressed between two identical ASD thin films to assess bulk crystallization rates. These sandwich materials were compared and contrasted with analogously prepared “open-faced” samples without the capping film to assess surface crystallization rates. Single particle analysis by scheduled automated SHG microscopy during *in situ* crystallization process produced average growth rates of ~2-3 $\mu\text{m}/\text{hour}$ for both bulk and surface particles. However much higher uncertainties were observed for crystals seeded at the surface, showing variation in crystal growth rates.

4.2 Methods

Materials used for preparing the samples include, milled hot melt extrudate (HME) of ritonavir ASD comprised of ritonavir (15%), sorbitan monolaurate (10%), copovidone (74%), and colloidal silicon dioxide (1%) and needle-shaped ritonavir form II API crystals, both prepared by AbbVie. The ASD was used to make the thin films, each 100 μm in thickness and the API crystals were seeded onto the films in order to prepare either “sandwich” or “open-face” sample.

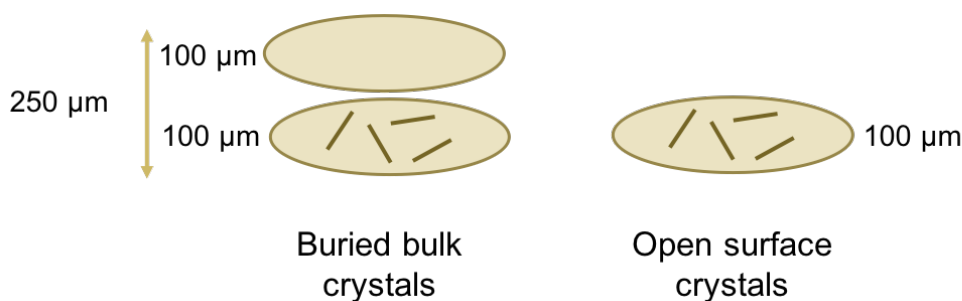


Figure 4.1. Schematic of "sandwich" and "open-face" seeded films.

A schematic cartoon showing the set-up of the seeded films are shown in Figure 4.1. To make ASD thin films, ~50-60 mg of the powdered sample was measured and put onto an aluminum-foil disk of 29 mm diameter, which was inside a constant thickness (100 μm by using specified spacer) film maker (Atlas Constant Thickness Film Maker, GS15640, Specac, UK). A second identical aluminum-foil disk was then placed on top. Then the whole assembly was positioned between the two heated platens at 115°C (GS15633, Specac, UK). After the temperature of the entire assembly reached the set temperature of 115°C, the pressure was set to 4 tons by using the Atlas Manual 15T Hydraulic Press (GS15633, Specac, UK). The set temperature and pressure were maintained for 10 minutes and then, the temperature was lowered to 65°C, but the pressure was maintained at 4 tons. After the temperature reached 65°C, the pressure was released, and the film maker assembly was placed inside a cooling chamber. The top foil-disk was peeled off, and individual needle-shaped ritonavir form II crystals were placed on top of it by single particle manipulation. Another 100 μm thick film from ritonavir HME ASD was prepared following the same procedure, and then the two films were pressed together using a 250 μm spacer to form the “sandwich” film. Temperature and pressure were maintained at 98°C and 1.25 tons for pressing the films. After the seeded sandwiched film was cooled down, the foil disks on both sides were carefully stripped off.

To make the open-faced film, both foil disks were peeled off from the 100 μm film and ritonavir form II crystals were carefully placed on top of the transparent film following the same technique.

Once the films with buried and exposed crystals were made, they were placed onto glass coverslips inside the CEiST platform maintained at 50°C/75% RH. Seeded single crystals were identified as regions of interest by initial screening by brightfield and SHG microscopy, and the same fields of view were imaged for the next 48 hours at one-hour intervals. Multiple z-steps were collected for probing the total volume of interest. Single particle tracking analysis was then performed on the growing crystals.

4.3 Results and Discussion

SHG images for both sandwiched and open-faced films at different time points are shown in Figure 4.2. The level of overall percent crystallinity is much higher for surface crystals than the bulk crystals. However, single particle tracking demonstrates the single particle growth rates are not significantly varied and they fall in the same order of magnitude, $\sim 2 \mu\text{m/hr.}$ and $\sim 4 \mu\text{m/hr.}$ for bulk and surface crystals, respectively. Although, the overall growth rates are similar, a large variance in the growth rates was observed for surface crystals, which was one order of magnitude higher from the bulk crystals.

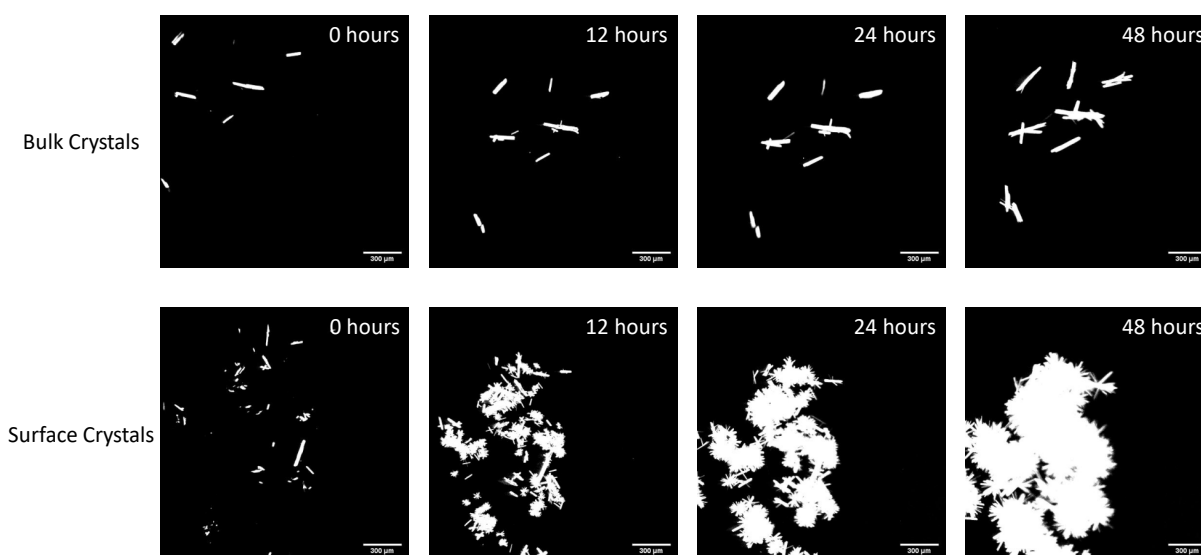


Figure 4.2. Evolution of seeded crystals in “sandwich” and “open-face” seeded films over time.

It is interesting to see the substantial differences in the morphological changes during crystal growth between the two cases. New crystals around the surface-seeded crystals started to appear due to the higher API concentration around the seeded crystals in the overall deliquescent matrix at elevated temperature and humidity conditions. Interestingly, this mechanism was significantly suppressed for buried crystals.

4.4 Future Direction

More data will be acquired to increase the number of tracked single particles for increased statistical significance. Further analysis is required to quantify the morphological transformations as well the complex nucleation behavior, which are currently under investigation. The current platform for in situ stability testing can hold up to 10 samples for a single run. Its advancement in providing increased signal to noise ratio by monitoring the same field of view over time can be further enhanced by increasing the number of sample-wells. High-throughput measurements deliver significant improvements by higher SNR, lower sample volume, lower storage burden etc.,⁵⁴ and at the same time can be coupled with fully-automated data acquisition and analysis processes for enabling autonomous instrumentation.

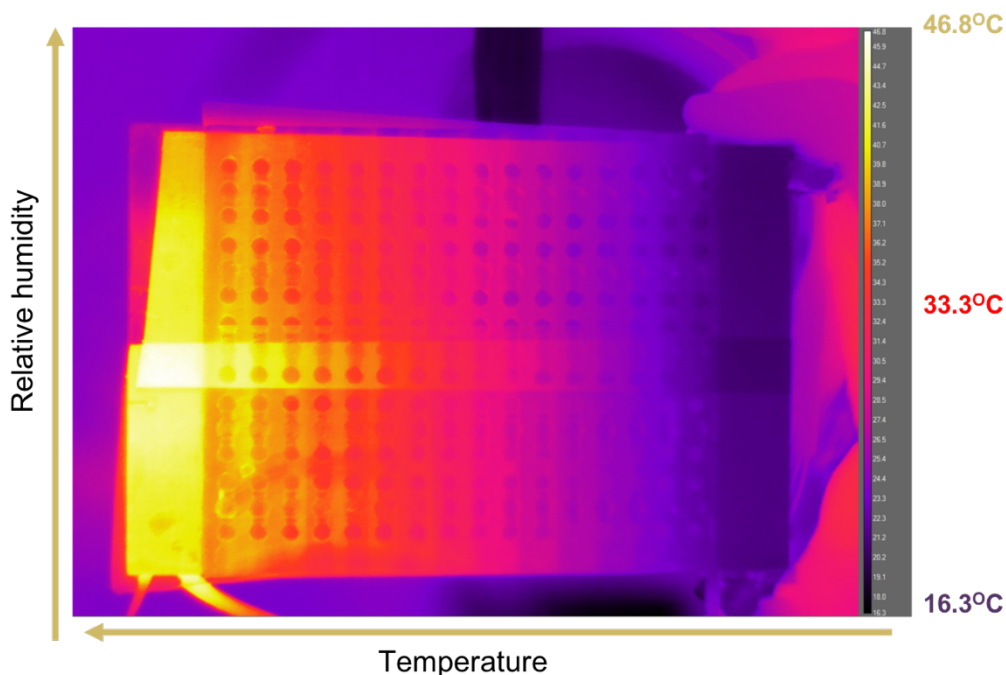


Figure 4.3. IR thermal image of the TRHA platform.

An effort is being undertaken currently to build a platform for high-throughput stress testing with variable temperature and humidity conditions, temperature and relative humidity array (TRHA). The TRHA platform is shown in Figure 4.3, which can be used to study the crystallization for up to 80 different samples in the same run. The temperature gradient runs through the horizontal axis, and the relative humidity (RH) varies along the vertical axis, as shown in Figure 4.3. The TRHA was built using aluminum as a thermally conductive metal, following a conventional 96-well plate footprint design. The temperature gradient was achieved by setting the temperatures at the two vertical ends at higher (50°C) and lower (10°C) temperatures, thus, creating a thermal gradient between the two ends. The temperature on the higher end was maintained by using a Tempco low density cartridge heater (LDC00003) and a thermocouple for feedback control by a custom controller built by the Johnathan Amy Facility at Purdue. On the other end, cold water was run through a narrow channel in the TRHA, which was maintained at 10°C by a water recirculation pump. The temperature gradient varied between $\sim 37^{\circ}\text{C}$ and $\sim 16^{\circ}\text{C}$ as seen from the IR thermal image of the TRHA, in Figure 4.3. An array of different RHs can be achieved by using saturated solution of particular salts. The temperature and RH gradients were already validated, and high-throughput measurements are currently being performed in the TRHA.

CHAPTER 5. QUANTIFICATION OF CRYSTALLINITY FOR ROD-LIKE PARTICLES BY CALIBRATION-FREE IMAGE ANALYSIS

5.1 Introduction

For a given API in the crystalline form is typically the most thermodynamically stable form and exhibits lower apparent aqueous solubility, which eventually leads to lower bioavailability.⁶¹ Although, in an ASD the API can have some equilibrium solubility in the polymer, and can be present below supersaturation. Therefore, precise quantification of trace crystallinity in the final dosage form as well as monitoring evolution of crystallinity during stress testing and dissolution testing are crucial. Currently, there are a few methods available to quantify the level of crystallinity from SHG microscopy that rely on image analysis, yet these methods depend on the overall percent crystallinity at the imaged sample.^{40,62}

At regimes of low crystallinity with negligible or no particle overlap, particle counting algorithms can be used with knowledge of the sample morphology to determine the percent crystallinity of the sample. At regimes of higher percentage crystallinity (generally at 2.5% or more),⁶² with a large amount of particle overlap, integration of the SHG intensity can be used to determine the percent crystallinity, but requires calibration standards.⁵³ In general, particle counting methods have a signal-to-noise advantage over the integrated intensity method due to suppression of dark counts and lack of variance in particle intensity that is inherent in SHG microscopy, yet the dynamic range of particle counting method is small due to the bias introduced from particle overlap. Integrated intensity is affected in the reliability and versatility of sample standards due to variance in particle thickness and orientation.⁶⁰ For the intermediate region between these two regimes of crystallinity, neither of these conventional methods works reasonably for quantification of crystalline content.⁶²

Previous work was done on bridging the gaps between the two methods of integrated SHG intensity and particle counting for overlapping spheroidal particles.⁶² Based on the relative variance in the recovered volume, a statistical model was developed from analytical expressions that optimized the signal-to-noise of particle counting methods to correct for the bias that originates from particle overlap. Likewise, with extraction of the SHG-activity per unit volume by the developed particle counting methods, this lower region of crystallinity was used as an internal standard for extension to signal integration. These methods were then supported by Monte Carlo

simulations and used to interpret nucleation and growth rates of evacetrapib (a cholesteryl ester transfer protein inhibitor). Despite these successes, the statistical model in the previous work was developed for low aspect ratio, spheroidal particles, complicating application of this model to the more general case of arbitrary aspect ratio, including rod-like and needle-like particles.

In this work, a generalized particle counting algorithm was developed to connect the two methods of quantification (particle counting and signal integration) for moderately overlapping particles of arbitrary aspect ratio. Through determination of individual particle widths and the average aspect ratio, an empirical model was developed in order to correct for bias introduced from particle-particle overlap. A computation package for simulating SHG images for rod-like particles was developed to evaluate the model. The developed model was then used on experimentally acquired data of ASDs of ritonavir to assess the particle counting model's applicability to sensitively recover crystallinity over a large dynamic range during *in situ* accelerated stability testing of ASDs.

5.2 Methods

5.2.1 Theoretical background

In SHG imaging, individual crystal in the DOF are visualized as single 2D particles in the image plane. At lower levels of crystallinity (for e.g. the parts per million regime), particle-counting algorithms can approximate the total particle volume by use of the cross-sectional area of each of the particles due to absence of particle overlap. At higher levels of crystallinity, the probability of particle-particle overlap within the DOF increases, and bias is introduced into the particle analysis. Since overlapping particles in an image are treated as a single particle by conventional approaches, the measured cross-sectional area of the overlapping particles will be higher than if the particles were completely separated. Thus, depending on the degree of overlap of the two particles, recovery of the total volume (and overall particle count) is challenging by conventional particle counting approaches alone.

To overcome the bias from particle overlap, methods have been developed that are able to correct for particle-particle overlap mostly for small aspect-ratio particles.⁶² Yet for higher aspect ratio particles (e.g. rod-shaped and needle-shaped particle), quantification is more complex due to the variability of aspect ratio, and the introduction of Euler angles (θ , ϕ , ψ) needed to fully

define a rod-like particle in real space. Defined as the angle out of the 2D projection plane, the polar angle can significantly affect the observed length in the cross-sectional area of a particle. The polar tilt angle (θ) has the most significant effect on the projection of a rod-like particle onto the 2D object plane, and the azimuthal angle (ϕ) and twist angle (ψ) do not significantly affect particle analysis.

For the current studies, high aspect-ratio particle (HARP) correction model is proposed, such that a modified particle-counting algorithm was developed to negate the large perturbations due to polar angle rotation and to correct against the bias from overlapping particles. The success of the HARP correction model lies in determination of the average aspect ratio and particle width to calculate the volume. Since the perturbations from the twist angle on the observed particle width (w_{obs}) is generally small, and generally, as rod-like particles grow the average aspect ratio is assumed to stay constant, the volume of the rod-like particle from the HARP correction model (V_{HARP}) can be determined by Equation 5.1, where the aspect ratio (AR) of a particle is defined as the ratio of the particles length (l) and width (w).

$$V_{HARP} = w_{obs}^3 * AR \quad (5.1)$$

To determine the average aspect ratio used in the calculation of particle volume, multiple fields-of-view (FOVs) and/or images of a system under investigation were used to find the particle for each FOV that has a polar angle closest being perpendicular to the optical axis. Thus, the HARP correction model assumes that particle with the longest length in each FOV is closest to perpendicular and provides the best estimate for the true aspect ratio of this particle. Once the average aspect ratio from multiple FOVs was calculated, determination of the width for each particle can allow for calculation of the particle volume. Lastly, a correction factor (α) was introduced into the HARP correction model to correct for deviations due bias introduced from orientation effects.

5.2.2 Auto-calibration

In the previous work with spheroidal particles, once the crystallinity of the sample had reached approximately 3% crystallinity, the SNR benefits from use of particle-counting algorithms are diminished, and correction of particle overlap becomes difficult. At this point, use of integrated intensity yields SNR advantage in volume determination, but requires a calibration standard to use. In the present work, images with crystallinity content up to 4% crystallinity were used in the

analysis, taking this integrated intensity switchover point from the previous work. From the best linear fit to all of the data points, the slope of this line provides the maximum likelihood estimate of the average integrated intensity per volume. With this value calculated, the particle volume can be extrapolated to time points with higher percent crystallinity by use of the integrated intensity.

5.3 Results

5.3.1 Experimental implementation

For experimental SHG images, ritonavir ASD was stressed under accelerated stability testing conditions under which rod-like crystals started to appear first with zero overlap and then with a varying degree of overlap between the particles. Rod-like ritonavir crystals are formed from 15% DL(w/w) ritonavir ASDs under accelerated stability testing conditions. ASD samples of ritonavir (15%), sorbitan monolaurate (10%), copovidone (74%), and colloidal silicon dioxide (1%) were prepared by AbbVie Inc. Different methods of preparation were used to make the ritonavir ASDs of same formulation, namely, hot melt extrusion (HME), rotary evaporation (rotovap), and spray dried dispersion (SDD). About 5mg of each of powdered ASD samples were placed onto glass cover slips inside a custom-built *in situ* platform for accelerated stability testing as thin layers (~300 μm). SHG images were collected at four different fields of views for statistical significance. The conditions in the platform were maintained at an elevated temperature of 50°C and 75% relative humidity for accelerated stability testing conditions. Automated scheduled SHG imaging of the samples inside the stressed platform were acquired for 0-24 hours, at every hour interval using a SONICC microscope from Formulatrix (Bedford, MA). SHG images were obtained using 350 mW excitation laser power and 894 ms exposure time. Images were collected in the transmission direction due to the high transparency of the sample through deliquescence of the powdered ASD at elevated temperature and humidity.

The amorphous polymer as well as other excipients present in the ASDs do not produce significant coherent SHG signal. However, ritonavir crystals formed during accelerated conditions adopt a non-centrosymmetric lattice upon crystallization that is SHG active, enabling selective detection of the crystalline particles using the HARP correction model. SHG micrographs of six representative time-points are shown in Figure 5.1 to illustrate the evolution of crystallinity in the ASDs during the accelerated stability testing. The volume fraction of the new crystalline phase

consisting rod-like ritonavir crystals was calculated using the HARP correction model, and conventional particle counting approaches that assume counting spherical ritonavir particles using FIJI. Though the respective aspect ratios for ritonavir crystals arising from HME, rotovap, and

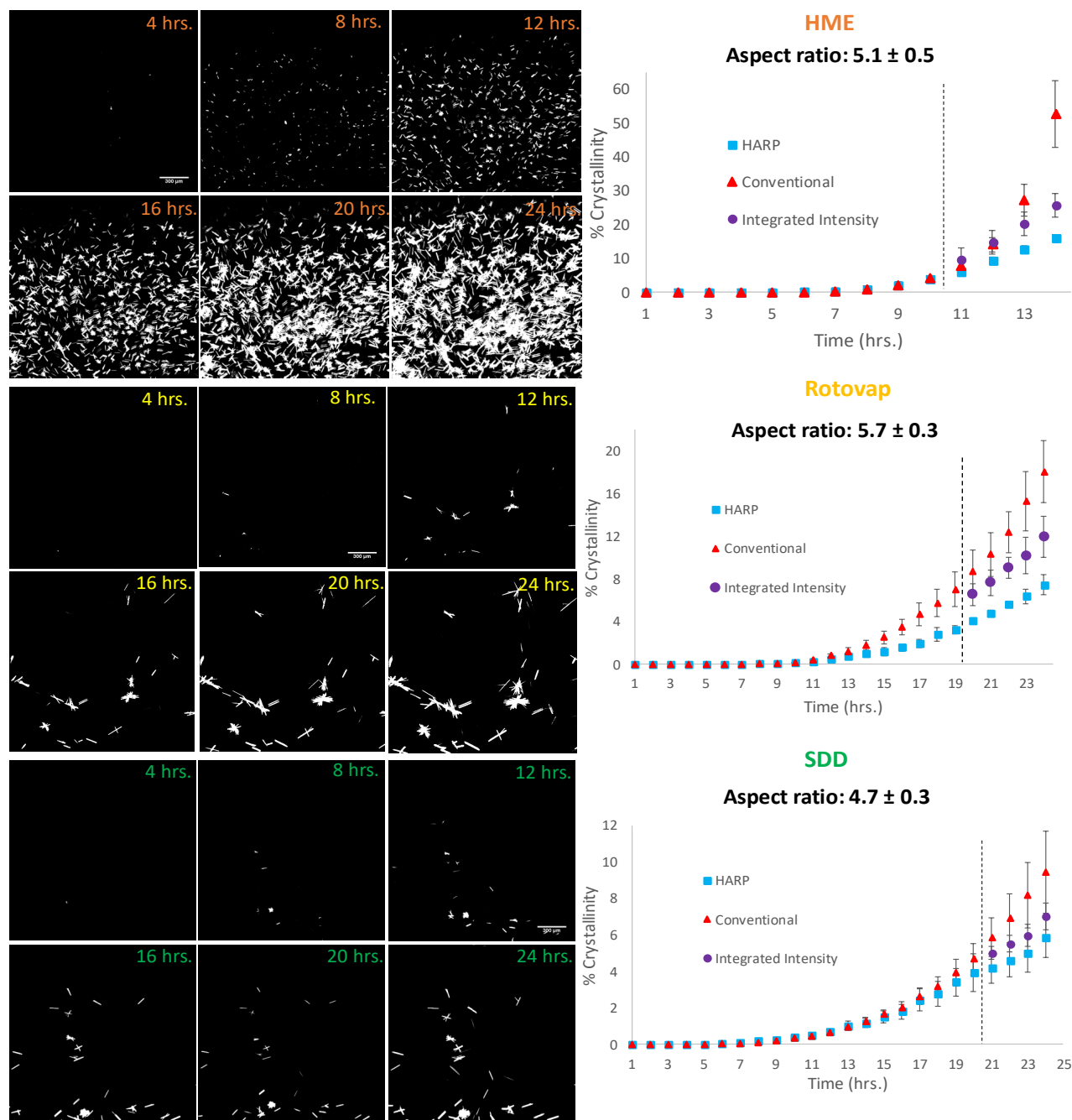


Figure 5.1. Time evolution of percent crystallinity in 15% ritonavir HME, rotovap, and SDD ASDs stressed *in situ* temperature and relative humidity-controlled platform at 50°C/75% RH.

SDD ASDs were very similar, as shown in Figure 5.1, the crystallization kinetics are substantially different in all three. The HARP model efficiently predicted the level of crystallinity in all three cases. The conventional model over-estimated the crystalline volume fraction, especially for later time-points. Overall, the HARP correction model was more effective in precise calculation of the percent crystallinity with higher confidence as seen from the values of the error bars in Figure 5.1. The autocalibration approach was used for crystalline phases beyond 4% as discussed above.

5.4 Conclusion

An empirical model for the quantification of crystallinity in SHG images for particles of high aspect ratio was theoretically and experimentally validated. Recovery of the average aspect ratio for multiple FOVs was validated, and a correction factor was optimized for the empirical model to account for the spread around this average value. Additionally, the HARP correction model allowed for calculation of the average integrated SHG intensity per volume from the particle-counting regime, allowing for quantification by signal integration without the need for an external standard. Recovery of particle volume was reliably shown from simulated SHG images of rod-like particles for this empirical model. Further validation of this model was done on experimental images of ritonavir ASDs, showing the applicability of particle-counting methods to quantification of crystallinity during accelerated stability testing. Thus, the empirical model improves the accessibility of crystalline quantification from nonlinear optical microscopy and facilitates a broader use in the pharmaceutical drug pipelines.

CHAPTER 6. PHASE BEHAVIOR AND CRYSTALLIZATION KINETICS OF EZETIMIBE ASD DURING DISSOLUTION IN BIORELEVANT MEDIA

Reprinted (adapted) with permission from Elkhazab A., Sarkar S., Dinh J. K., Simpson G. J., Taylor L. S., Variation in Supersaturation and Phase Behavior of Ezetimibe Amorphous Solid Dispersions upon Dissolution in Different Biorelevant Media, *Molecular Pharmaceutics* **2018** 15 (1), 193-206. Copyright: American Chemical Society.

6.1 Introduction

With increasing complexities and advancements in drug discovery, in recent years more and more molecules tend to show higher molecular weights and lower aqueous solubilities, showing BCS class II or class IV drug behavior.⁴ To increase the solubility of these drug substances, ASD is one of the most common approach for formulating effective drug products.³³ ASDs show accelerated dissolution rates and generate supersaturated solutions upon introduction to aqueous media, therefore exhibiting apparent higher solubilities.^{63,64} However, since supersaturation is a metastable state, after dissolution in a media, it can undergo desupersaturation, meaning decreased dissolved drug concentration. The amorphous drug crystallizes in this stage, indicating lower efficacy of the drug product. Therefore, it is crucial to study the supersaturation-desupersaturation phase behavior of the ASDs.

A number of factors affect the phase behavior of a drug product, namely the particle size, a specific polymorph, effective surface area, chemical stability in certain dissolution media, presence of excipients (lubricants, suspending agents), solubility of drug, drug loading etc.⁶⁵ Certain characteristics of the media where the drug is dissolving also affect the supersaturation behavior, including dissolution volume, pH of the media, presence of co-solvents, enzyme, surfactant, bile salts, and phospholipids.⁶⁶ In addition to that, an *in vitro-in vivo* correlation (IVIVC) is necessary by establishment of an *in vitro* dissolution testing environment simulating the composition and hydrodynamics of the gastrointestinal environment.^{3,31}

In this work, the phase transformations during the dissolution of a BCS class II drug, ezetimibe ASDs, upon introduction to different dissolution media were studied. Ezetimibe is used for lowering cholesterol levels in the blood. ASDs of ezetimibe: polymer (50:50 w/w) were prepared with polyacrylic acid (PAA), polyvinyl pyrrolidone (PVP), and hydroxypropyl

methylcellulose acetyl succinate (HPMC-AS). The selected polymers show varied levels of hydrophilicity, PAA being the most hydrophilic and HPMC-AS being the most hydrophobic one, therefore, affecting the release of the drug in certain dissolution medium. Dissolution testing was performed in different media including sodium phosphate buffer (10 mM, pH 6.8), fed state simulated intestinal fluid (FeSSIF, pH = 5.0) and Ensure Plus®. Both FeSSIF and Ensure Plus® are well-established biorelevant media and have been widely used for mimicking intestinal and gastric fed state conditions respectively. The utility of second order nonlinear optical imaging of chiral crystals (SONICC) for the detection of crystallization in turbid biorelevant media was explored. Ezetimibe has a chiral center, and therefore the amorphous drug is expected to crystallize into an SHG-active space group upon desupersaturation, enabling differentiation between undissolved amorphous material/dissolution media components, and crystalline content.

6.2 Materials and Methods

Ezetimibe monohydrate (Cambridge Crystallographic Data Center ref code QATNEF), which crystallizes as the orthorhombic SHG-active space group ($P2_12_12_1$) was purchased from Attix Pharmaceuticals (Toronto, Ontario, Canada). Polyacrylic acid (PAA), polyvinyl pyrrolidone (PVP) K29/32 were supplied by Sigma-Aldrich (St. Louis, MO), while hydroxypropyl methylcellulose acetyl succinate (HPMC-AS) MF grade was supplied by Shin-Etsu Chemical Co. (Tokyo, Japan). Methanol and Acetonitrile were purchased from Fisher Scientific (Pittsburgh, PA). FaSSIF/FeSSIF/FaSSGF powder (Version 1) was acquired from Biorelevant (London, UK). Ensure Plus® vanilla nutrition shake (8 oz bottles) was obtained from Abbott Laboratories (Chicago, IL).

The evolution of ezetimibe crystallinity during ASD dissolution in sodium phosphate buffer (10 mM, pH 6.8), FeSSIF and Ensure Plus® was investigated as a function of time using SHG microscopy. All three media were confirmed to show zero SHG signal, prior to adding the prepared dispersions for dissolution. Dissolution experiments were performed as described above, and samples for SHG analysis were prepared by removing a small aliquot of the dissolution media at different time points. Each sample was pipetted into a round nylon 6/6 flat washer (inner diameter: 6.069 mm, outer diameter: 11.938 mm, thickness: 0.381 mm, Small Parts Inc., Logansport, IN) mounted on a glass slide. A coverslip was then added to form a small liquid cell of known thickness. SHG images were acquired using a commercial SHG microscope instrument

manufactured by Formulatrix (Bedford, MA). This instrument utilizes a Fianium FemtoPower laser (1064 nm, 51 MHz repetition rate and a 166 fs pulse width) equipped with resonant mirror/galvanometer beam scanning (8 kHz fast axis) to generate images. All SHG microscopy acquisitions were acquired with 350 mW infrared (IR) power, and an exposure time of 894 milliseconds. SHG microscopy images had fields of view of dimensions of 1925 μm x 1925 μm , and scans were obtained in different focal planes in the Z direction, with 100 μm increments. For each measurement three different fields of views were inspected for statistical significance.

6.3 Results and Discussions

The current understanding of possible phase transformations of supersaturated solutions in the complex media used as surrogates for gastrointestinal fluids is rather limited and has not been adequately investigated to date. Crystallization is one of possible phase transformations of supersaturated solutions in complex biorelevant media, which ultimately result in the loss of supersaturation, consequently lowering the driving force for membrane transport. Turbidity, and presence of phospholipids, bile salts etc. associated with biorelevant media make the process further complicated. Furthermore, the dissolution media often turns turbid due to the formation of an amorphous, drug-rich phase and the solutions then contains small scattering species generated during ASD dissolution. Conventional spectroscopic and optical techniques therefore cannot be applied to study these systems. Moreover, differentiation of the crystalline versus non-crystalline phase becomes extremely important for adequate characterization of the system. SHG microscopy enables selective detection of the new API crystalline phase in complex turbid media.²⁵

Quantitative analysis of the SHG images allows disentanglement of nucleation and growth kinetics in driving crystal formation in the different media. For the crystal growth kinetics, the change in average crystal size was recorded as a function of time. The majority of the images contained too many overlapping crystals for reliable determination of the average crystal size by particle counting. Instead, Fourier analysis of the images allowed estimation of the mean particle sizes from the first minimum in the radial power spectrum. The results of the crystallization kinetics are summarized in Table 6.1. Both the nucleation and growth rates are averaged values across the duration of the experiment. Integration of the total SHG intensity was used to assess the fractional crystallinity at the longest time-points in the experiments, which are also included in Table 6.1. Final crystallinity represents the percentage values of the crystalline material per unit

volume of each field of view in the SHG images, that is, the amount of crystallinity in a given volume of medium, and not the percentage of crystallinity in the ASDs.

6.3.1 Dissolution behavior in sodium phosphate buffer

SHG microscopy images were acquired for samples withdrawn from the dissolution media at different time points, with results shown in Figure 6.1. The ASDs formulated with PAA showed

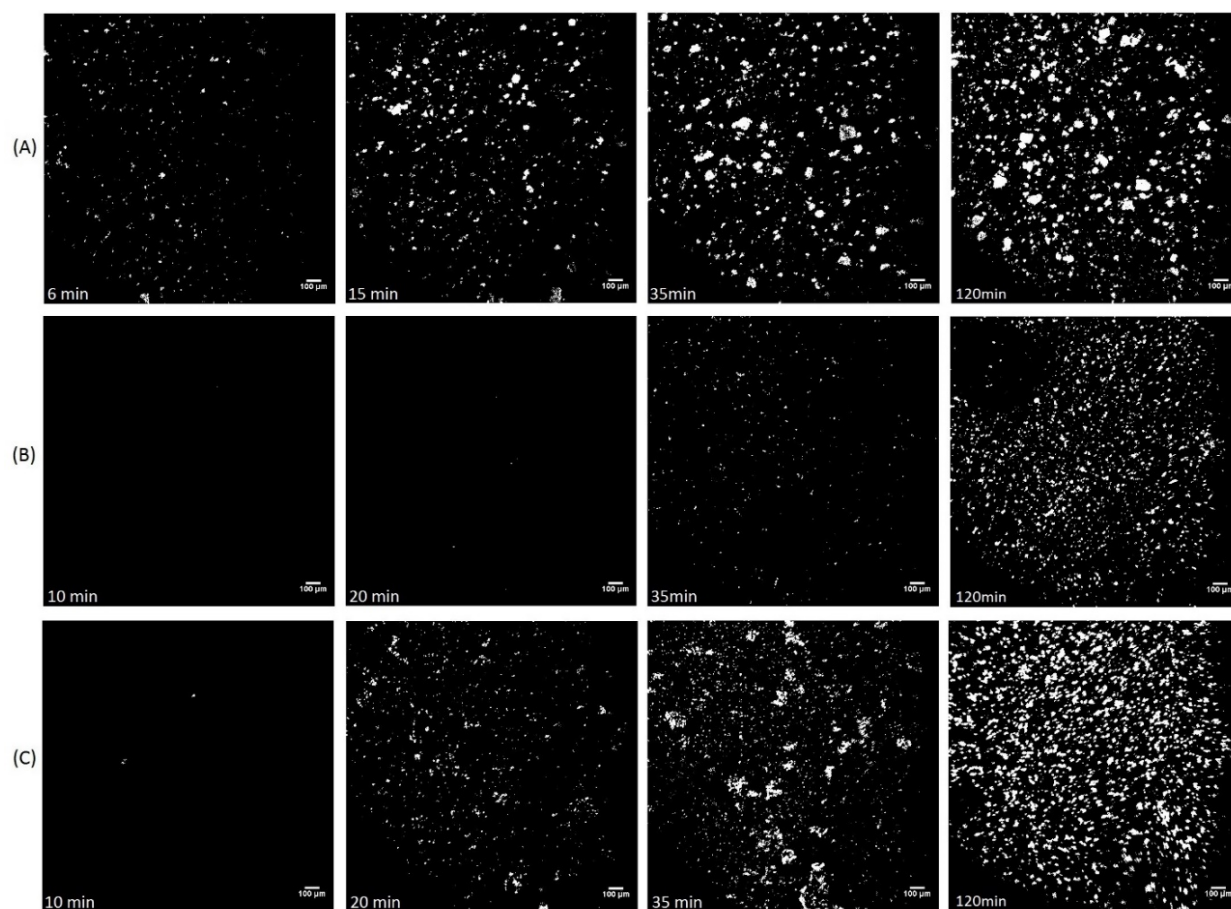


Figure 6.1. SHG microscopy images of ezetimibe ASDs; (A) PAA at 6, 15, 35, and 120 minutes, (B) PVP at 10, 20, 35 and 120 minutes, and (C) HPMC-AS at 10, 20, 35 and 120 minutes, upon dissolution in sodium phosphate buffer at 37°C. Scale bar: 100 µm.

SHG-active crystalline domains as early as 6 minutes, after which the SHG signal increased with time, both in terms of the size of crystalline regions and the total SHG count. For the ASDs prepared with PVP, the presence of crystals was minimal at 10 and 20 minutes. At 35 minutes, however, a few SHG active domains started to appear, with a notable increase in size and number

at 120 minutes, can be seen in Figure 6.1 (B). The appearance of significant crystallinity in the SHG images coincided with the decrease in ezetimibe concentration observed in Figure 5, after 30 minutes. ASDs prepared with HPMC-AS showed minimal (but not zero) crystallinity initially with

Table 6.1. Nucleation and growth kinetics obtained from SHG microscopy images analysis measured in different dissolution media (n = 3)

Dissolution medium	Polymer in ASDs	Nucleation rate (no. particles/min/ μm^3)	Growth rate ($\mu\text{m}/\text{min}$)	Final crystallinity %
Sodium phosphate buffer	PAA	15 ± 2	0.3 ± 0.2	30 ± 5
	PVP	80 ± 40	0.4 ± 0.1	13 ± 2
	HPMC-AS	110 ± 40	1.0 ± 0.3	32 ± 2
FeSSIF	PAA	$\gg 30$ Indefinite due to particle overlapping and large variations in particle size.	0.2 ± 0.1	4 ± 0.6
	PVP	600 ± 200	0.020 ± 0.001	8 ± 4
	HPMC-AS	0.04 ± 0.03	0.05 ± 0.02	0.04 ± 0.02
Ensure Plus®	PAA	0.07 ± 0.03	0.7 ± 0.2	0.08 ± 0.03
	PVP	0.03 ± 0.02	0.2 ± 0.1	0.03 ± 0.01
	HPMC-AS	0.02 ± 0.01	0.2 ± 0.1	0.02 ± 0.01

increased crystallinity emerging at 20 minutes and evolving at the 35 minute and 120 minute time points. After 35 minutes of dissolution, and based on the SHG signals, the PVP dispersion showed less crystals than the other dispersions. However, all three ASDs demonstrated a comparable degree of crystallinity after 120 minutes of dissolution.

For PAA dispersion, no supersaturation was observed, and crystallization occurred once the solid amorphous material was added to the buffer. For both PVP and HPMC-AS supersaturation was also short-lived. Despite the slight delay in the onset of crystallization, the average nucleation rate throughout the dissolution experiment was higher for PVP and HPMC-

AS dispersions relative to the PAA dispersions, whereas the final crystalline contents after 120 minutes were very similar and higher for PAA and HPMC-AS dispersions (Table 6.1).

6.3.2 Dissolution behavior in FeSSIF

SHG images for these systems are shown in Figure 6.2. PAA dispersions were highly crystalline after 15 minutes, with no apparent evolution of the SHG signals in terms of size and count after that time point. PVP ASDs displayed very few crystalline regions at 15 minutes, however the extent of crystallinity rapidly increased at later time-points whereby the crystallites were much smaller than those observed for the PAA systems. In contrast, HPMC-AS ASDs showed much more stable dissolution behavior, with SHG images indicated very few crystallized regions in the first hour, which gradually increase at later time-points, however the crystallinity is lower in comparison to the PAA and PVP dispersions.

PAA dispersion showed similar phase behavior in buffer and FeSSIF but with higher nucleation rate. The PVP dispersions dissolved very rapidly in FeSSIF, and only after 30 minutes there were considerable number of microcrystals. SHG images suggest that PVP acts as a poor nucleation as well as crystallization inhibitor for ezetimibe in FeSSIF. Hence, at the high supersaturation generated by rapid release of ezetimibe from PVP ASDs in FeSSIF, the nucleation rate is high (Table 6.1), leading to many small crystals appearing for these dispersions. SHG imaging also showed overall reduction in crystallization for this system with low nucleation and crystal growth rates, as shown Table 6.1. HPMC-AS dispersion appeared to be an effective crystallization inhibitor in the presence of the drug-rich colloidal phase of ezetimibe, and the components of FeSSIF did not reduce that inhibitory effect, as in the case of PVP.

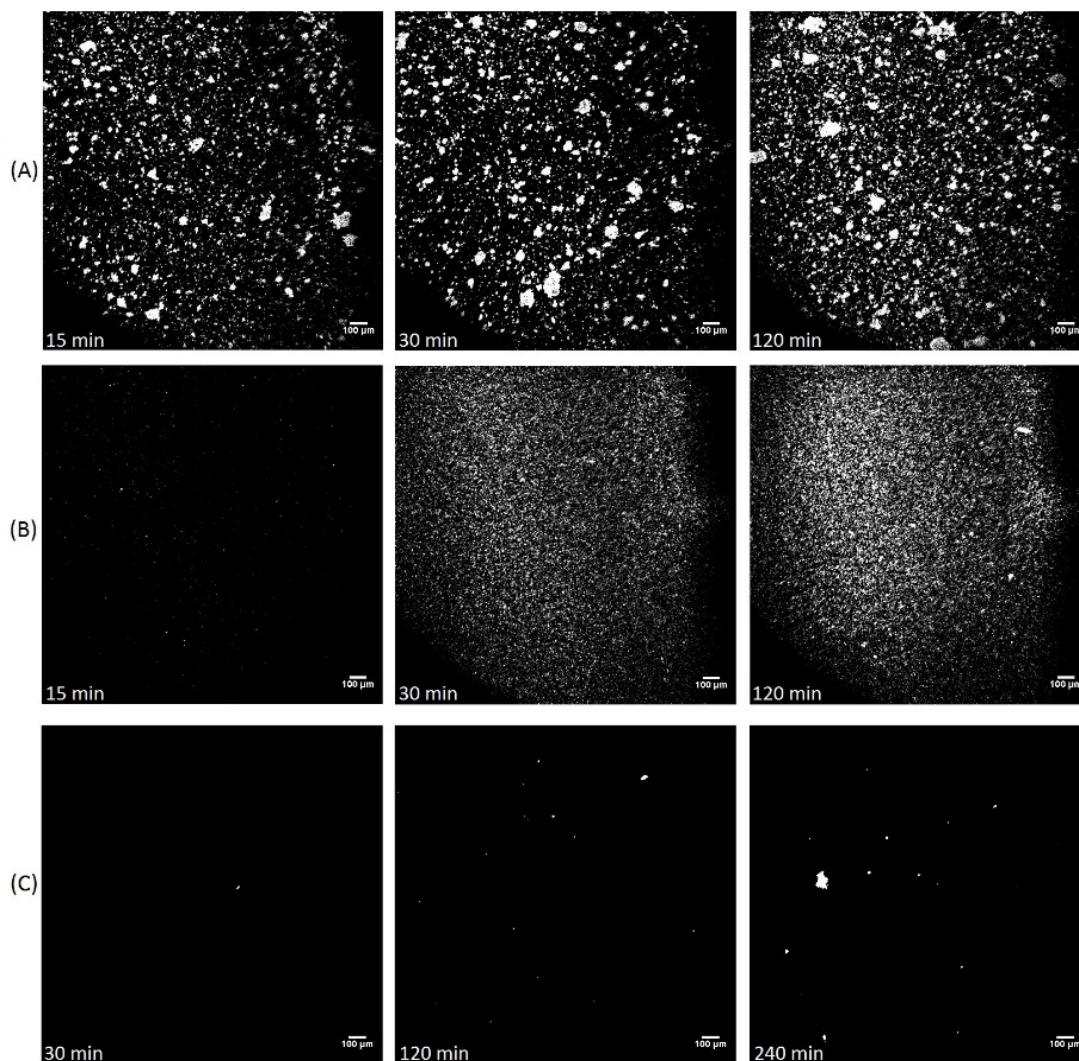


Figure 6.2. SHG microscopy images of ezetimibe ASDs; (A) PAA at 15, 30 and 120 minutes, (B) PVP at 15, 30, and 120 minutes, and (C) HPMC-AS at 30, 120 and 240 minutes, upon dissolution in FeSSIF at 37°C. Scale bar: 100 µm.

6.3.3 Dissolution behavior in Ensure Plus®

SHG images showed that ASDs formulated with PAA, Figure 6.3 (A) and PVP, Figure 6.3 (B) had small levels of crystalline material present after 10 and 20 minutes respectively. In contrast, the HPMC-AS ASD exhibited no SHG signal initially, with the first indications of crystallinity occurring at the 120-minute time-point, Figure 6.3 (C). Regardless of the polymer used, the evolution of the SHG signal during dissolution of all dispersions in Ensure Plus®, with respect to count and size with time, was much lower in comparison relative to observations in other media.

Ensure Plus provide an interesting approach to mimic the fed-state gastric state, and a better understanding of how ASDs perform in a complex biorelevant lipid-rich medium. It has

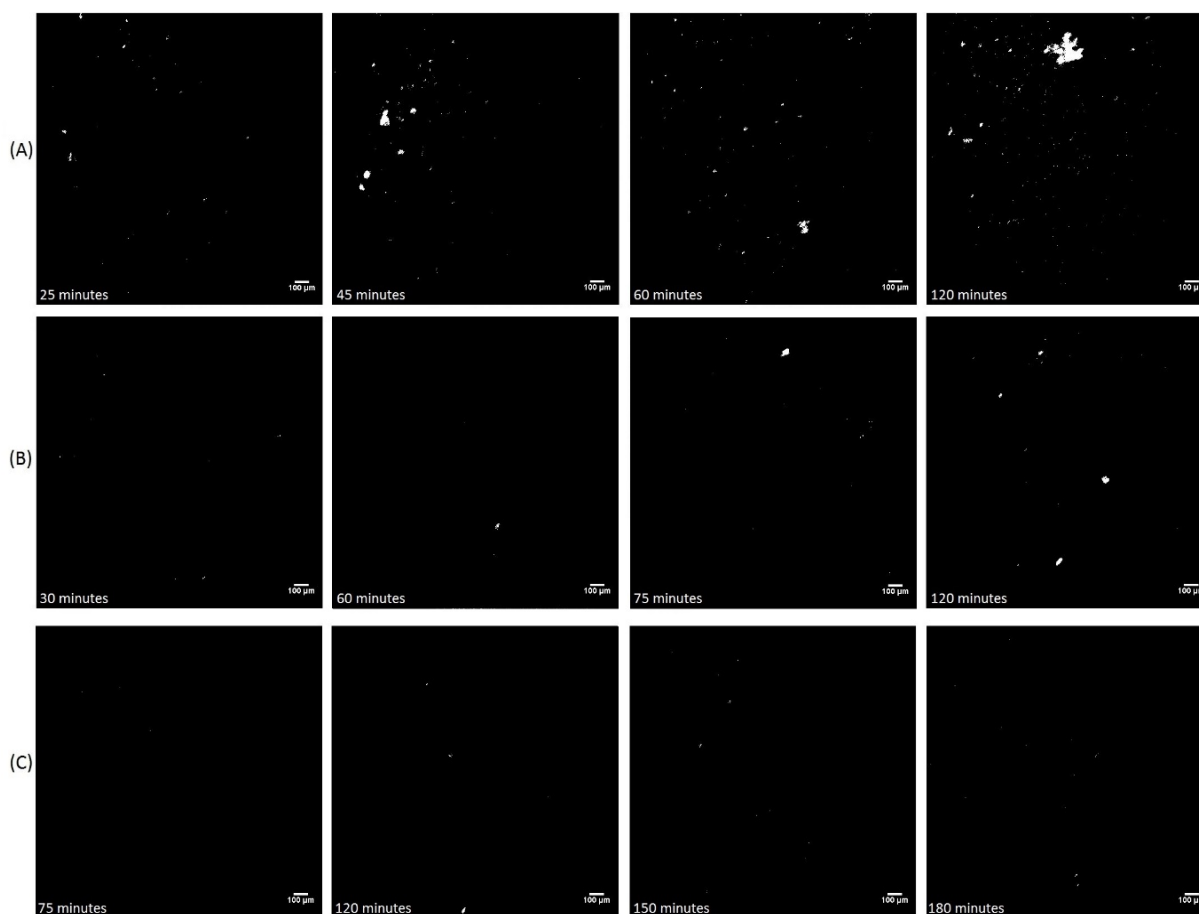


Figure 6.3. SHG microscopy images of ezetimibe ASDs; (A) PAA at 25, 45, 60 and 120 minutes, (B) PVP at 30, 60, 75 and 120 minutes, and (C) HPMC-AS at 75, 120, 150 and 180 minutes, upon dissolution in Ensure Plus® at 37°C. Scale bar: 100 µm.

high solubilizing power due to its high lipid content and the possible binding of drug to peptides or proteins. It can also lead to micelle formation, raising the solubility of highly lipophilic compounds. All the dispersions irrespective of the polymer showed significantly higher level of supersaturation in Ensure Plus® than both buffer and FeSSIF. HPMC-AS ASDs were the most stable formulation during dissolution in Ensure Plus®, where only tiny crystals could be observed after 2h, with little progression in size and number by 3 h, Figure 6.3 (C).

6.4 Conclusions

Dissolution behavior of the dosage form in biorelevant media is the key to understand the effect of gastrointestinal compartment for *in vitro* processes. SHG microscopy stands out to be the most valuable tool by selective identification of crystalline phase in highly turbid biorelevant media comprising of complex compositions enabling better understanding of nucleation and crystal growth kinetics during phase separation, which would not have been possible by any other suite of analytical technique. As Ensure Plus® contains lipid vesicles and micelles, they can substantially increase the solubilization capacity and therefore, affect the crystallization kinetics. From analysis of the SHG micrographs, it is clear that differences in the nucleation kinetics rather than growth rates dominate the overall trends in crystallinity. The present work explored the variations in dissolution behavior of ASD in a variety of media of relevance to oral delivery, which in turn will facilitate the formulation of ASDs that maximize supersaturation and are robust to crystallization.

CHAPTER 7. PHASE SEPARATION OF WEAKLY BASIC ASD DURING TWO-STAGE DISSOLUTION PROCESS

7.1 Introduction

Formulating a poorly soluble API as an ASD can significantly improve the intestinal absorption of the drug by increasing the apparent solubility.⁶⁷ However, as the ASD resides in an energetically higher state, it always has the tendency to revert back to the crystalline state. The propensity is influenced by many different factors, including degree of supersaturation.⁶⁸ Crystallization inhibitors, such as polymers, excipients, surfactants are typically employed to maintain the supersaturated state over a sufficient period for efficient absorption.⁶⁹ Polymers can delay crystallization by impacting nucleation and/or crystal growth.⁷⁰ Although the mechanisms of preventing crystallizations are not extensively explored yet. For ASDs formulated with enteric polymers, which are practically insoluble at acidic pH and form suspensions under gastric conditions, it is extremely important to inhibit the crystallization in the matrix prior to complete dissolution *in vivo*.⁷¹ Thus, the drug release to the small intestine where absorption is typically favored can be controlled.

The gastrointestinal physiology can influence the solubility of an API.⁷² Crystallization kinetics also can vary significantly depending on level of pancreatic secretions, pH of the environment, gastrointestinal transfer, residence times etc. Altogether, these are pivotal for effectual formulation and drug product development. For weakly basic drugs, the increase in pH during intraluminal transit from the gastric compartment to the intestinal compartment in the fasted-state can drastically decrease the aqueous solubility (ionized to nonionized state), resulting in supersaturation.^{73,74} Therefore, *in vitro* dissolution experiments for weak bases should take into consideration the pH-shift occurring during the gastrointestinal transit.⁷⁵

Posaconazole is an extended-spectrum triazole antifungal exhibiting very low aqueous solubility and is considered a BCS class II drug. Posaconazole often suffers from variable and unpredictable absorption affected by several factors including meal intake, dosing regimen and gastric dysfunction in some patient groups.⁷⁶ Noxafil® is the marketed delayed-release tablet comprising posaconazole molecularly mixed with hydroxypropylmethyl cellulose acetate succinate (HPMC-AS) where the ASD is prepared by hot melt extrusion. As HPMC-AS is a pH sensitive polymer, Noxafil® tablets provide a formulation approach to avoid extensive drug

release in the stomach and thus avoid some of the variability described above. When Noxafil® tablets were administered, gastric aspirates under fasted and fed state indeed showed only a small extent of release in the stomach.

In the present study, the drug release, supersaturation and crystallization kinetics of posaconazole ASDs, as well as Noxafil® tablets, using *in vitro* fasted-state biorelevant media representing gastric and small intestinal conditions were evaluated. A two-stage dissolution setup to test the role of pH shift on drug dissolution behavior was adopted. The impact of an abrupt shift from an acidic gastric environment represented by fasted-state simulated gastric fluid (FaSSGF [pH 1.6]), to a fasted state intestinal environment represented by fasted-state simulated intestinal fluid (FaSSIF [pH 6.5]), on the phase behavior was studied using SHG and two photon excited UV-fluorescence (TPE-UVF) microscopy to evaluate both solid state and solution state phase transitions.

7.2 Materials and Methods

Posaconazole (Form I) was purchased from Chemshuttle (Hayward, CA). Noxafil® delayed-release tablets manufactured by Merck & Co. (Kenilworth, NJ) were purchased from the Purdue Pharmacy (West Lafayette, IN). Hydroxypropyl methylcellulose acetyl succinate (HPMC-AS) MF grade was supplied by Shin-Etsu Chemical Co. (Tokyo, Japan). Acetonitrile, hydrochloric acid (HCl), maleic acid, methanol and sodium chloride were purchased from Fisher Scientific (Pittsburgh, PA). Sodium hydroxide (NaOH) was obtained from Avantor Performance Materials, LLC (Radnor, PA). FaSSIF/FaSSIF/FaSSGF and FaSSIF version 2 powders were bought from Biorelevant (London, UK).

The dissolution testing for posaconazole ASDs consisted of two stages using two dissolution media: the gastric phase (FaSSGF), and the intestinal phase (FaSSIF). The two-stage dissolution setup is summarized in Figure 7.1. During both stages of dissolution, the media were stirred at 300 rpm, and the temperature was maintained at 37°C.

SHG microscopy was used to detect the onset of crystallinity during dissolution of posaconazole ASDs and tablet powder. The crystallization of SHG-active compounds can be detected by differentiating chiral crystals from an amorphous or solution state. TPE-UVF microscopy was also used as a compliment to SHG for sensitive detection of posaconazole presence irrespective of its physical state. Two-stage dissolution experiments were performed as

described above, however the amount of ASD relative to the dissolution media was scaled up (5 times) to provide adequate SHG and TPE-UVF signals for image analysis. Accordingly, 80, 32, 16 and 50 mg of the 10%, 25%, 50% ASDs and the tablet powder respectively, was weighed and

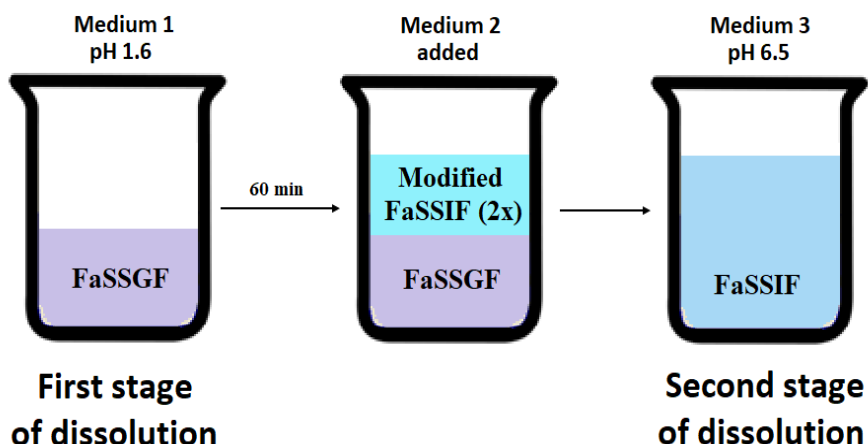


Figure 7.1. Schematic of the two-stage dissolution experiments

dispersed in 20 mL of FaSSGF. After 60 minutes, 20 mL of modified pH-FaSSIF concentrate was added to generate normal strength FaSSIF. Samples for SHG and TPE-UVF analysis were prepared by removing a small aliquot of the dissolution media at different time points. Time points taken for each sample were typically at 30 and 60 minutes of dissolution in FaSSGF, and at 30, 60, 120 and 180 minutes of dissolution in FaSSIF. Each sample was pipetted into a round nylon-6/6 flat washer (inner diameter, 6.069 mm; outer diameter, 11.938 mm; thickness, 0.381 mm; Small Parts Inc., Logansport, IN) mounted on a glass slide. SHG and TPE-UVF images were acquired using a commercial second order nonlinear imaging of chiral crystals (SONICC) instrument manufactured by Formulatrix (Bedford, MA). SONICC uses the Fianium FemtoPower laser operating at 1064 nm with 51 MHz repetition rate and a 166 fs pulse width. Beam scanning with resonant mirror/galvanometer with 8 kHz fast axis beam scanning generates images. For TPE-UVF experiments, the fundamental beam was doubled to 532 nm through focusing onto and through a lithium triborate crystal (LBO, 5×5×2 mm). The 532 nm incident light was then directed through the beam scanning unit and then focused onto the sample with a dichroic mirror centered at 532 nm with a 10x objective (Nikon, 0.3 NA). The SHG signal at 532 nm was collected in trans-direction by a 10x near-UV objective (Thorlabs, 0.25 NA). Brightfield and TPE-UVF images were

collected in the epi-transmission. SHG microscopy images were acquired at 350 mW infrared (IR) power and an exposure time of 894 ms, while TPE-UVF images were acquired at 50 mW power and 447 ms as an exposure time. SHG and TPE-UVF images had fields of view of dimensions of $1925\ \mu\text{m} \times 1925\ \mu\text{m}$, and scans were obtained in different focal planes in the Z direction, at 100 μm steps. Imaging analysis was performed using ImageJ 1.05b software. The number of new particles formed per unit time was obtained by employing the built-in particle counting algorithm in ImageJ, using the time dependent SHG and TPE-UVF images.

7.3 Results and Discussions

7.3.1 Study of phase separation during dissolution by SHG and TPE-UVF

SHG images acquired during dissolution of these systems at different time-points are shown in Figures 7.2. All three dispersions, plus the tablet powder, displayed the presence of crystallinity early on during the FaSSGF stage. As shown in Figure 7.2 (A), (B) and (D), the 10%, 25% ASDs and tablet powder showed a few crystals after 30 minutes of immersion in acidic media. In FaSSIF, SHG-active domains were also present at 30 minutes and 180 minutes with an increase in number at the later timepoint. The 50% ASDs were highly crystalline in terms of size and number of crystals compared to the other dispersions, throughout all timepoints of the dissolution experiments, Figure 7.2 (C). It should be noted that no crystals were observed in the ASDs prior to dissolution studies, strongly suggesting that crystallization was initiated by suspension in gastric conditions. Figure 7.3 shows TPE-UVF images which can be used to monitor the suspension/dissolution of ASDs and tablet powder in FaSSGF and FaSSIF. During suspension in FaSSGF, TPE-UVF images revealed large ASD particles containing posaconazole (posaconazole is not fully released in the gastric medium due to the polymer insolubility). Upon media transfer to FaSSIF, the TPE-UVF- active signals notably decreased for the 10%, 25% ASDs and tablet powder, consistent with drug release as the polymer dissolved in the higher pH environment. This was not the case for the 50% ASDs however, which is consistent with extensive crystallinity in the ASD matrix. It should be noted that the fields of views from both SHG and TPE-UVF were not exactly congruent, thus overlaid images cannot be trivially generated. The corresponding brightfield images for the 10% ASDs are also displayed (Figure 7.3) providing further information about the ASD particles during dissolution.

7.3.2 Quantification of crystalline and undissolved amorphous drug content

Finally, integration of the SHG signal intensity was utilized to calculate the fractional volume crystallinity for SHG, while the overall fractional volume of posaconazole species (crystalline and amorphous) was be assessed by using the TPEF signal intensity. These results are

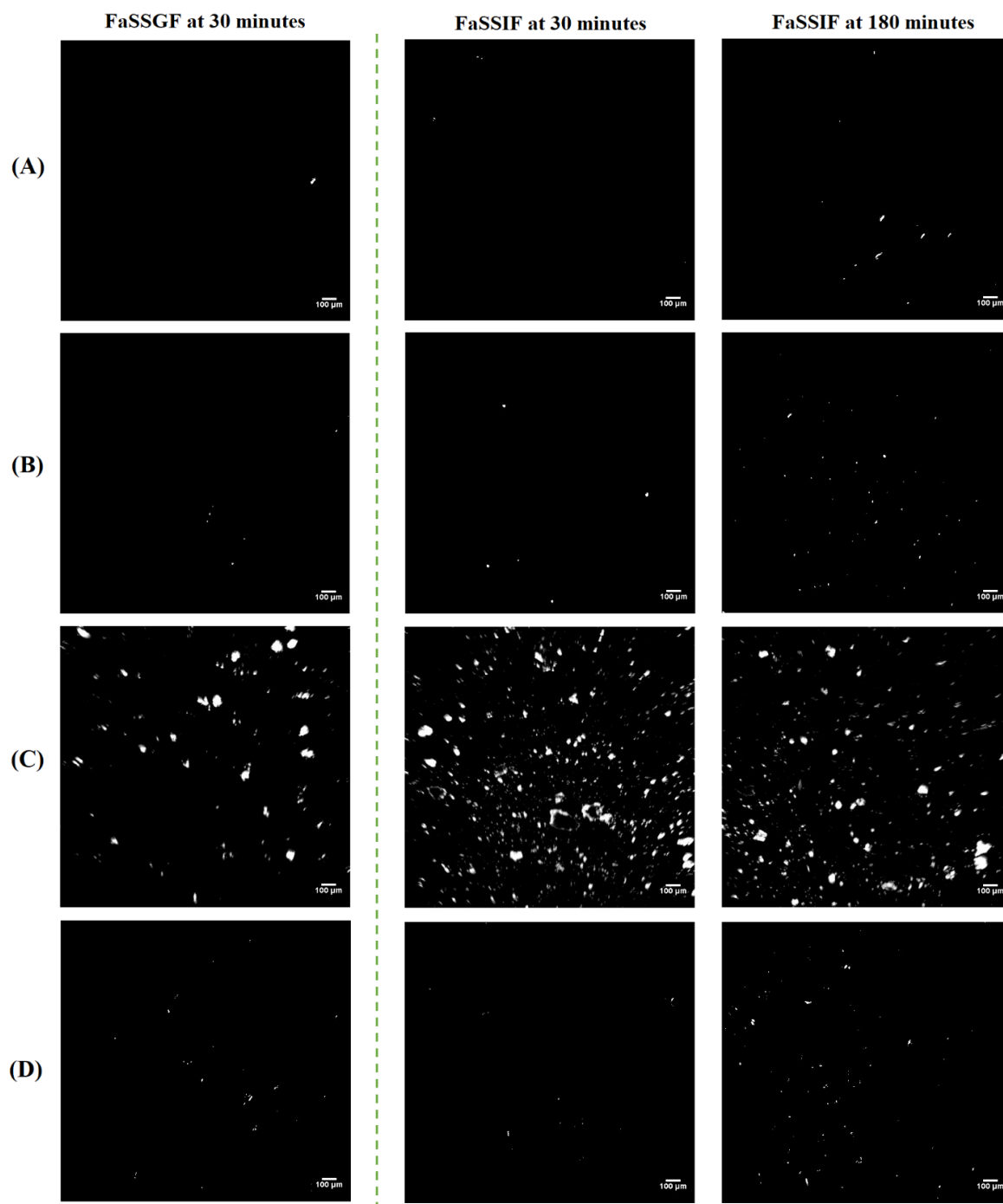


Figure 7.2. SHG images of posaconazole ASDs prepared at (A) 10%, (B) 25%, (C) 50% drug loading and (D) tablet powder upon suspension/dissolution in FaSSGF for 30 minutes (left column), dissolution in FaSSIF for 30 minutes (middle column), and dissolution in FaSSIF for 180 minutes (right column). Scale bar: 100 μm.

summarized in Figures 7.4. In Figure 7.4 (A), the volume fraction crystallinity % appeared to increase with time for all systems until it reached a maximum at 240 minutes of dissolution.

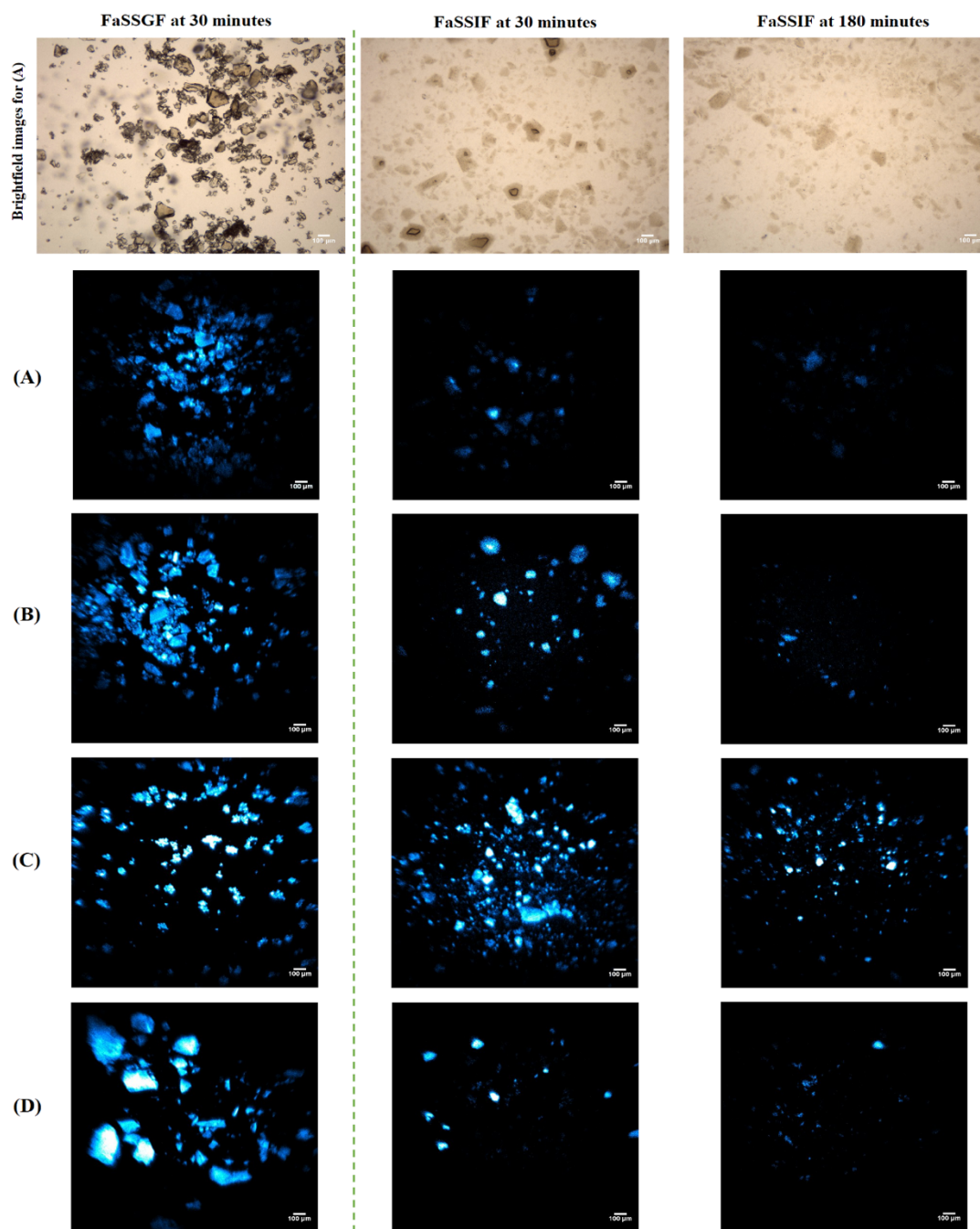


Figure 7.3. Brightfield and TPE-UVF images of posaconazole ASDs prepared at (A) 10%, (B) 25%, (C) 50% drug loading and (D) tablet powder upon suspension/dissolution in FaSSGF for 30 minutes (left column), dissolution in FaSSIF for 30 minutes (middle column), and dissolution in FaSSIF for 180 minutes (right column). The corresponding brightfield images for (A) 10% ASDs are shown in the first row. Scale bar: 100 µm.

Additionally, the 50% ASDs had the highest average volume crystallinity compared to the other systems, where the final crystallinity at end of the experiment was roughly 250 times that of 25% ASDs. Figure 7.4 (A) demonstrates the volume fraction of undissolved posaconazole species as detected from the TPE-UVF signal intensity. Except for the 50% ASDs, all systems demonstrated higher volume fraction values of detectable posaconazole species in the FaSSGF dissolution stage, in comparison to the FaSSIF dissolution stage, since the majority of the drug was not released in the gastric medium.

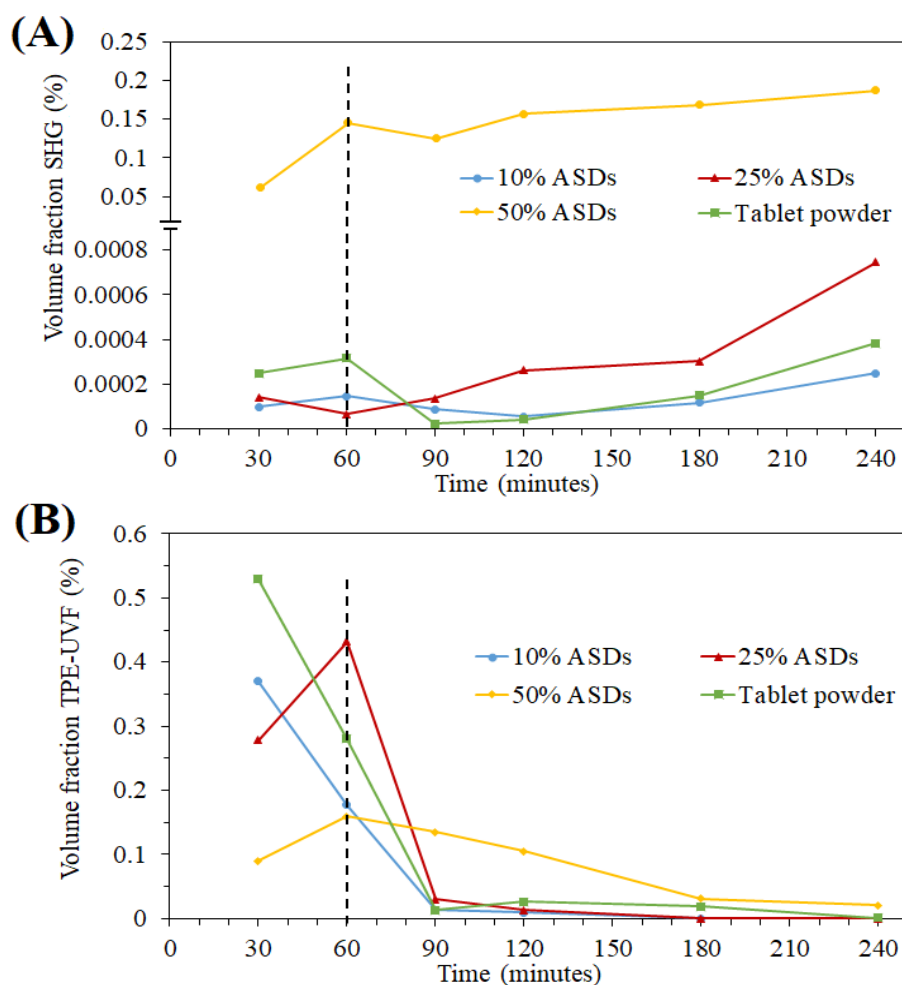


Figure 7.4. Volume fraction (%) calculated for (A) SHG signal (crystallinity) and (B) TPE-UVF signal (undissolved posaconazole either in amorphous or crystalline form) for all ASDs and the tablet powder at different time points, upon dissolution in FaSSGF then FaSSIF. The dashed vertical line denotes media transfer at that timepoint. Error bars are omitted for clarity.

The drug remaining in the undissolved ASD appears to be susceptible to crystallization when suspended in an aqueous solution. This is clearly demonstrated in Figure 7.2, where SHG images indicate that some crystals are present following suspension of the ASDs in the gastric medium, even after only 30 minutes. TPE-UVF analysis (Figure 7.3) confirms that phase-separated posaconazole is still present in the matrix, and therefore full release in the gastric medium had not occurred for any of these systems. The extent of crystal formation was found to be much greater in the 50% ASD, although varying levels of crystallinity evolved in all formulations. The finding raises questions about the functionality of polymers with pH dependent solubility, not only in terms of controlling drug release, but also in mitigating drug crystallization upon dissolution. Notably, no crystallinity was detected in any ASD prior to immersion in gastric media indicating that HPMC-AS is effective at preventing crystallization during ASD fabrication, but not upon exposure to water. In Figure 7.5, the ratio of the average volume fraction crystallinity (based on SHG analysis) and the average volume fraction of undissolved posaconazole (based on TPE-UVF analysis) is shown for all dispersions during suspension/dissolution in FaSSGF after 30 minutes. This ratio provides an estimate of the percentage of matrix crystallization that occurred in the gastric media and highlights the much higher extent of crystallization in the 50% ASDs relative to the other formulations, which show only limited crystallinity.

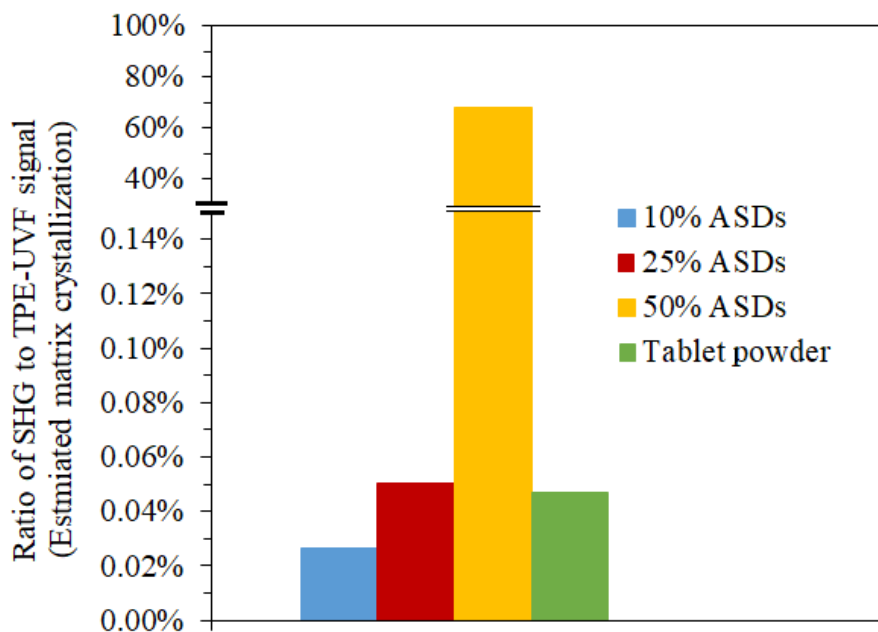


Figure 7.5. Ratio of volume fraction crystallinity to volume fraction posaconazole (from Figure 7.4) during suspension/dissolution in FaSSGF after 30 minutes.

Despite the higher dissolved concentration in gastric conditions, a minimal extent and duration of supersaturation was observed for the 50% ASD upon media transfer. This can be attributed to the presence of extensive matrix crystallization (Figure 7.2). Crystals present in the undissolved matrix at the time of media transfer were released when HPMCAS dissolved in the higher pH environment. These posaconazole crystals were expected to grow rapidly due to the ambient supersaturation present in the intestinal medium, whereby the rate of desupersaturation depended on the surface area available for crystal growth, the extent of the initial supersaturation, as well the occurrence of any additional primary or secondary nucleation events. For the 50% ASD, extensive matrix crystallization occurs in the gastric stage, and correspondingly, desupersaturation is instantaneous, to an extent that the first analysis point reveals that the amorphous solubility is not achieved. In addition, no posaconazole nanodroplets were observed for these ASDs. This implies that majority of posaconazole remaining in the ASD matrix underwent crystallization in the gastric medium stage, whereby no detectable amorphous drug was still present (Figure 7.5). This was not the case for the low drug loading systems, since they had a much lower crystal burden and a largely amorphous content at the time of media transfer, and consequently, a greater potential for supersaturation.

7.4 Conclusion

Characterization of posaconazole ASDs in a multi-compartmental biorelevant dissolution setting was crucial to understanding the impact of pH-shift on drug release, supersaturation and precipitation kinetics. The extent of generated supersaturation upon conversion to the unionized state of posaconazole in the intestinal medium, was highly affected by the amount of posaconazole released in the gastric medium and the extent of matrix crystallization in the undissolved ASD particles. SHG microscopy images revealed the presence of crystals during the first stage of dissolution for all systems, which promoted further crystallization during dissolution in the simulated intestinal medium, even when supersaturation was initially generated. These *in vitro* dissolution results provide insights for better formulation prediction of poorly soluble weakly basic drugs, in the context of utilizing controlled-release ASDs, as well as understanding origins of intraluminal absorption variability for such systems.

CHAPTER 8. NON-NEGATIVE MATRIX FACTORIZATION FOR ISOLATING DAMAGE-FREE REFLECTIONS IN MACROMOLECULAR SYNCHROTRON DATA COLLECTION

8.1 Introduction

High resolution structures of macromolecules enable rational drug design and provide direct insights into fundamental mechanisms of action in proteins and protein assemblies.⁷⁷ Currently, X-ray diffraction (XRD) is arguably one of the most versatile tools for the generation of high-resolution structures supporting such efforts.⁷⁸ However, X-ray induced damage during diffraction data collection, results in overall loss in diffraction intensity, which ultimately limits the achievable resolution.^{79,80} The precise mechanism by which photoelectrons of the high-energy X-ray beam contribute towards the loss in diffraction resolution still leaves room for exploration.

Significant work has been done to combat the issue of radiation damage induced to protein crystals during X-ray diffraction. Performing experiments under cryogenic conditions can significantly decrease the induced radiation damage.⁸¹ However, cryo-cooling of the crystals can lead to an increase in mosaicity, which results in a reduction in diffraction signal to noise and an increase in spot overlap and does not allow for access to dynamic information within the crystal.⁸² Few mathematical models have been established to predict the diffraction intensities by extrapolation to a zero-dose point.^{83,84} Beam shaping to produce a “top-hat” beam profile has been used to reduce the non-uniform X-ray exposure associated with traditional Gaussian beam profiles.^{85,86} Implementation of this method is nontrivial and does not actually reduce the X-ray dosage delivered to the crystal, still resulting in damage. Free radicals generated during X-ray diffraction can be removed using radical scavengers in an effort to reduce secondary radiation damage, although additives can complicate the crystallization process and there is a large variability in the success of this method. In the X-ray free electron laser (XFEL) approach, atomic resolution diffraction data are being produced without the need of cryo-cooling the sample to reduce damage, an alternative source is followed by utilizing the “diffract, then destroy” approach.⁸⁷ XFEL has been proven to be significantly effective only for serial crystallography, not for single crystal data collection. Nevertheless, new ways to reduce the influence of damage during X-ray data collection are continually being explored.

In this work, the numerical isolation of the unperturbed peaks by non-negative matrix factorization (NMF) method is proposed. In brief, the original XRD pattern of tetragonal lysozyme prior to any significant X-ray damage was recovered. Identification of multiple sequential perturbations was enabled by NMF and corresponding changes in the reflections from each of them were isolated.

8.2 Methods

8.2.1 Synchrotron XRD data acquisition

The crystallization protocol for tetragonal lysozyme was adapted from a method previously reported⁸⁸ and further detailed in previous publications.⁸⁹ For cryogenic X-ray diffraction experiments, crystals were prepared in 96-well plates and then looped and flash-frozen in liquid nitrogen. For room temperature diffraction experiments, crystals were grown in capillaries, which were then sealed with epoxy prior to mounting for diffraction.

All X-ray diffraction data were collected at the Advanced Photon Source (APS) at Argonne National Lab using GM/CA@APS beamline 23-ID-B. Diffraction of lysozyme under cryogenic conditions was acquired with a 20 μm -diameter X-ray beam, $20 \times 20 \mu\text{m}$ cell size, with 1 s exposure time and full unattenuated beam and a detector distance of 200 mm. A full tilt series involving a 90-degree rotation of the lysozyme crystal in 0.9-degree increments was obtained using these conditions.

To assess the X-ray damage caused by radiation in the mother liquor adjacent to a crystal, room temperature diffraction was performed with the same conditions used for diffraction at cryogenic temperatures. A flowchart detailing the room temperature diffraction data acquisition can be found in Figure 8.1. Radiation was imposed at one spot on the crystal for 10 ms. After a 1-minute interregnum, the process was repeated for 5 cycles. A grid area was then selected surrounding the crystal and radiated with a 1 s exposure at each stop in the grid. Radiation of the previously selected spot on the crystal was repeated for another 5 cycles with the same conditions.

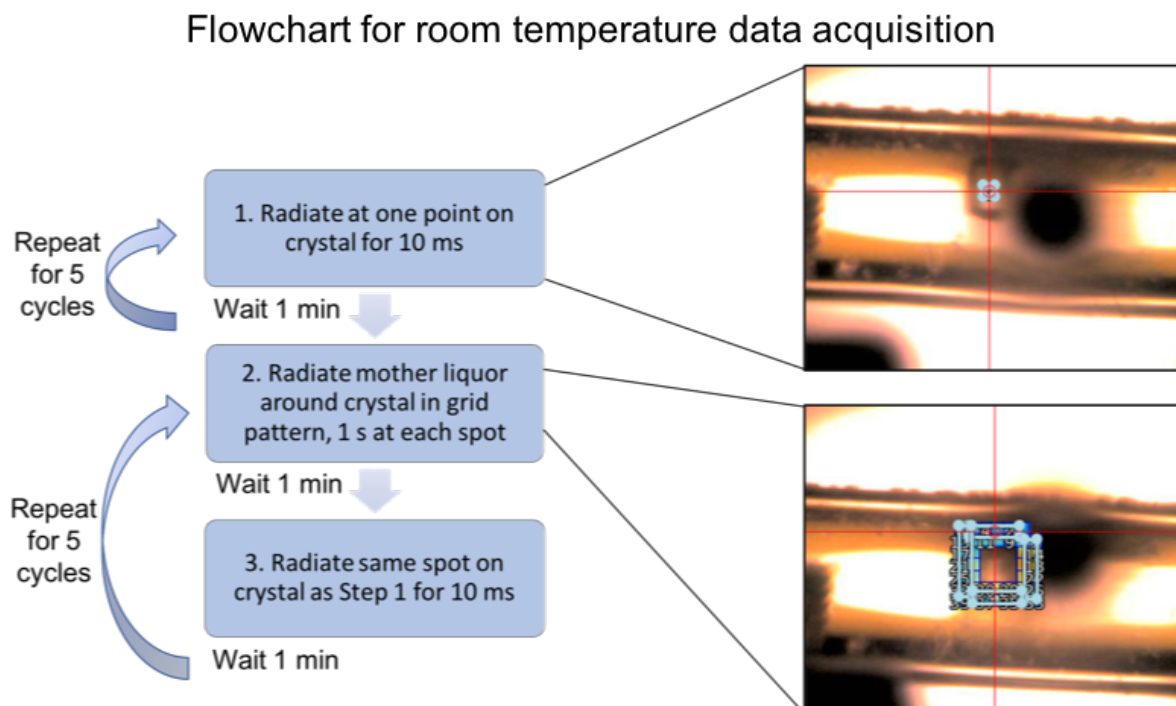


Figure 8.1. Schematic for data collection by X-ray radiation in locations adjacent to the crystal at room temperature.

8.2.2 Algorithm

8.2.2.1 Dimension Reduction

Peak-fitting was performed to identify discrete reflections arising from crystal diffraction. A MATLAB script written in-house was used to read-in a series of synchrotron X-ray diffraction patterns, which were all taken at the same location of the crystal repeatedly, i.e. with accumulated X-ray dosage. The first step involved identification of peaks in the first image of the stack and then tracking the intensities of these peaks through the entire stack of images. For image peak identification at a particular tilt angle, intensity-based threshold settings were applied on a per pixel basis following background subtraction. Each individual peak was fit to a Gaussian, and the 99.95% confidence interval was used to track corresponding reflections throughout the data acquisition stack. Based on these criteria, the following information regarding individual peaks in each image was obtained: (i) number of pixels in the peak, (ii) X coordinate of the center of the peak, (iii) Y coordinate of the center of the peak, (iv) integrated intensity of the peak, and (v) distance from the peak center to the center of the diffraction image. The peak-identification results of the first XRD image served as a "library" or "reference" for subsequent XRD images. The

program then compared the (X,Y) location and variance of peaks in a given image with corresponding parameters within the “library”, which were scored as arising from the same reflection when overlapping within 99.95% confidence. Next, the integrated intensities of peaks scored to be from the same reflection within the image stack were arranged in a matrix D, with M rows and N columns, where M is the number of peaks in the peak library, and N is the total number of XRD images.

8.2.2.2 NMF

In the NMF formulation of the XRD problem, the N experimentally measured (or generated) diffraction intensity patterns were combined into one observational data matrix $D_{M \times N}$, given by the product of the (yet unknown) matrices C and S (Equation 8.1). The overall algorithm comprising of dimension reduction followed by NMF has been illustrated in Figure 8.2. At each of the N peaks at every M image, the values of the matrix D are formed by a linear mixing of K unique but unknown end members. These end members form the unknown matrix, $C_{M \times K}$ (Equation 8.3), blended by an also unknown mixing matrix, $S_{K \times N}$ (Equation 8.2). The goal of the NMF algorithm is to retrieve the K original non-negative basis patterns (encoded in C) that optimally recover the M measured intensity values for each peak in D. Since both factor matrices C and S are unknown, and even their size K (i.e., the number of unique components) is unknown the problem is under-determined if no additional constraints are imposed. In NMF, both the amplitudes of the diffraction peaks and the amplitudes in C are assumed to be positive, consistent with the underlying physics. With these constraints, solution of Equation 8.1 is no longer necessarily under-determined, and can be solved by iterative solutions for C and S. NMF can solve such types of problems by leveraging the multiplicative update algorithm.

One of the complications of the classical NMF algorithm is that it requires *a priori* estimate of K, the number of end members. In this particular case, we assumed the number of unique components produced during XRD data collection is 3. The assumption was based upon the optimum recovery of XRD patterns of the components and their kinetics approach. First, assuming three pure components ($K = 3$), the contributions of individual peaks in each unique diffraction pattern was determined, removing negative entries. Since negative concentrations correspond to nonphysical results, negative entries were set to zero.

$$D_{(M \times N)} = C_{(M \times K)} S_{(K \times N)} \quad (8.1)$$

$$S = (C^T C)^{-1} C^T D \quad (8.2)$$

From the guessed set of contributions, the diffraction pattern of each component was determined, again setting negative entries to zero.

$$C = DS^T(SS^T)^{-1} \quad (8.3)$$

The algorithm was iterated between these two steps until no negative values were present in either S or C.

8.2.3 Kinetic modeling

The variation in the concentration of NMF components were modeled as a first-order kinetic process. A first-order reaction can be described by a system of differential equations,

$$\frac{d\vec{A}}{dt} = K\vec{A} \quad (8.4)$$

where $\frac{d\vec{A}}{dt}$ is a vector of derivatives representing the change in concentration of a reactant or product with respect to time, K is a matrix of rate constants, and \vec{A} is a vector of length m containing concentrations of reactants and products. As has been demonstrated previously,⁹⁰ this differential equation can be solved in such a way as to show that,

$$\vec{A}_t = (Pe^{\Lambda t} P^{-1}) \vec{A}_0 \quad (8.5)$$

such that,

$$\Lambda = P^{-1} K P \quad (8.6)$$

where Λ is a diagonal matrix and P is an orthonormal matrix of dimension $m \times m$. This relation is used in this work to generate the first-order fits to the variation in component concentrations extracted via NMF.

Algorithm for dimension reduction followed by non-negative matrix factorization (NMF)

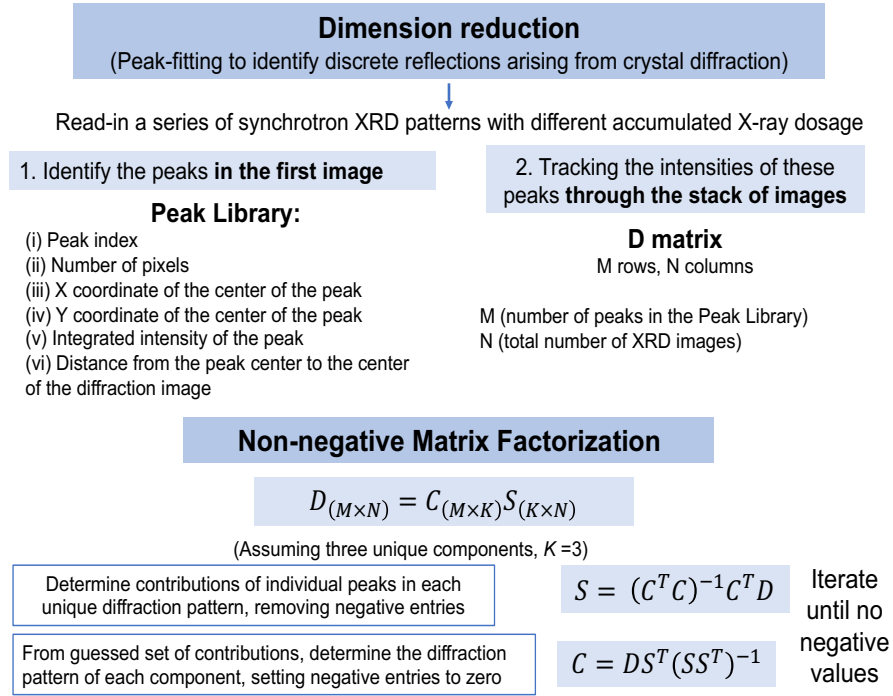


Figure 8.2. Flowchart of the algorithm for dimension reduction followed by NMF.

8.3 Results and Discussions

8.3.1 Decomposition into multiple XRD patterns

Matrix C contained information about contribution of each individual peak towards each unique component. Therefore, after multiple rounds of iteration to obtain C with no negative entries, 4096×4096 pixels simulated XRD images were generated to assist in visualization of the outputs. The MATLAB generated images after NMF, as seen in Figure 8.3, depicted the reconstructed XRD pattern of the three decomposed components, namely (A), (B), and (C). The color scale bar on the right side of each image signified the relative intensity of each peak in each component.

It is worthwhile to make a note on the angular distribution of the peaks. As shown in Figure 8.3, no significant difference was noticeable among the angular distributions of the peaks in all of the three components and relative intensity of the peaks was indeed the key determining factor.

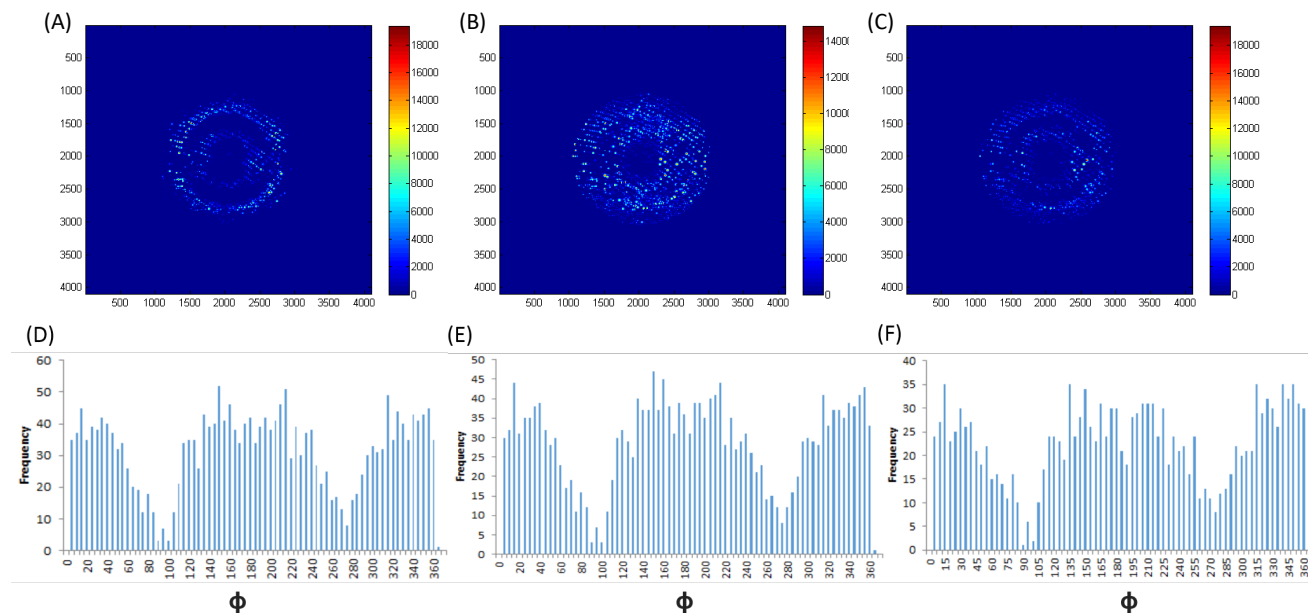


Figure 8.3. (A), (B), (C) Decomposed XRD patterns for three components; (D), (E), (F) angular distribution of the peaks in three respective components.

8.3.2 Kinetic modeling of X-ray damage

Matrix S from equation 8.1 depicts the change in concentration of the peaks with increasing dose for three individual components. Equation 8.6 was used for first-order kinetic modeling to fit the variation in relative integrated intensities of the peaks in respective components. The results of the fitting are shown in Figure 8.4 for A, B, and C. Remarkably, the different components appear to be consistent with a simple, sequential kinetics process. The unperturbed protein had the highest overall integrated intensity at the beginning of the damage process, with small, but not zero contributions present from the damaged protein, namely B, and C. Component A undergoes rapid damage by the X-ray radiation fairly quickly, after ~ 20 -30 doses. Whereas, relative integrated intensities of components B and C started to increase at the same rate. While B experienced an initial rise and then fall, C showed a consistent increase and then maintained the same relative contributions even after going through high-energy radiation damage at the end of 90 doses.

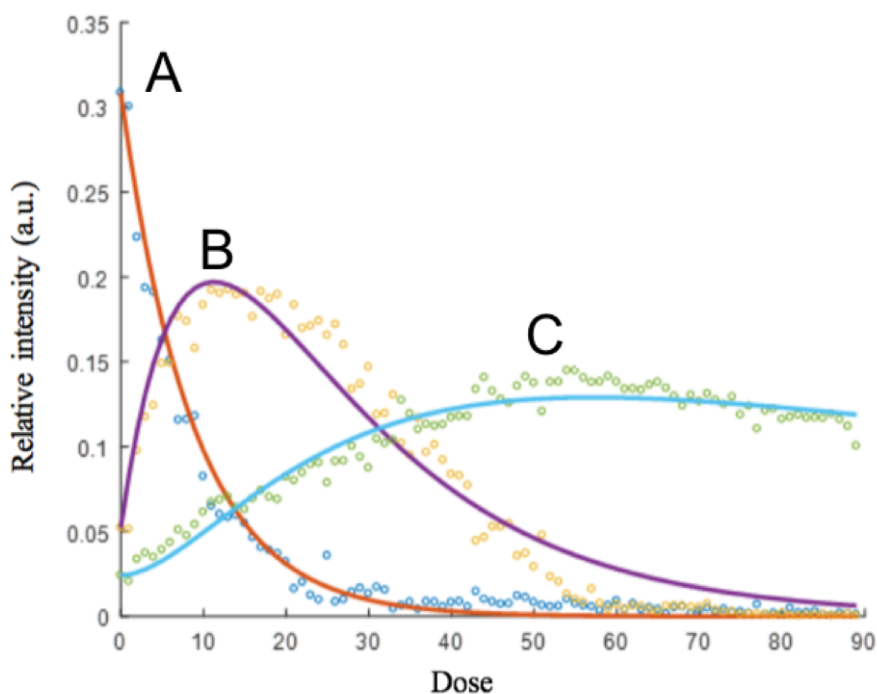


Figure 8.4. Kinetics of propagation of damage at cryogenic conditions.

8.3.3 Effect of X-ray exposure around the crystal at room temperature

Free radicals produced by primary and secondary photoelectrons can migrate at room temperature to produce X-ray damage through a mechanism largely shut down at cryogenic temperature. At this condition, even a small amount of radiation dose can damage the protein crystal to a significant extent. The effect of X-ray exposure around the crystal (i.e. in the mother liquor), without any direct exposure on the crystal was investigated. The results are outlined in Figure 8.5, where the top profile, (A) illustrated change in the overall integrated intensity of XRD peaks due to damage induced by radiation around the crystal at room temperature and the bottom profiles, (B), (C), and (D) represented variation of the intensity after decomposition into three components by applying NMF. The vertical bar in each plot signifies the point at which the X-ray radiation was applied around the crystal, that was between 6th and 7th data point. In Figure 8.5 (B), (C), and (D) the initial slower loss or gain in relative integrated intensities can be attributed to the damage process due to the direct exposure at the center of the crystal till the 6th data point. As the crystal experienced immediate damage caused by the diffusion of radiation in the mother liquor around the sample, all the components exhibited sudden decrease or increase in intensity, rendering rapid transitions due

to damage. Without the application of NMF, the effect of radiation around the crystal was not pronounced in the change of overall integrated intensity for the whole protein.

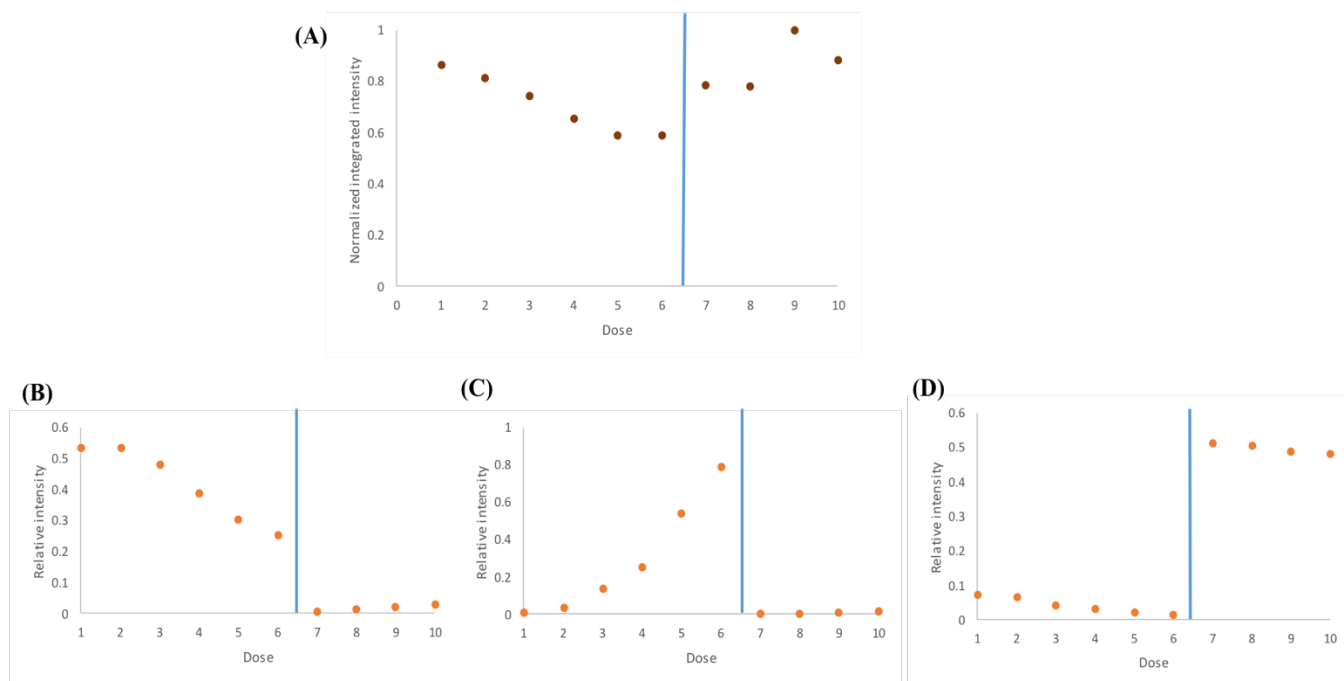


Figure 8.5. (A) Change in the overall integrated intensity of XRD peaks, (B), (C), and (D) decomposition into multiple components after applying NMF due to damage induced by radiation around the crystal at room temperature.

8.4 Conclusions

A “damage-free” set of reflections in macromolecular crystallography was mathematically isolated by NMF. Biological samples undergoing X-ray induced damage under synchrotron X-ray radiation impose a fundamental limit in data collection for crystallography/structural biology. Damage during diffraction data collection can have a significant impact on the quality of the recovered protein structures. Here, we recovered the native X-ray diffraction (XRD) pattern of tetragonal lysozyme prior to X-ray exposure. NMF enabled identification of multiple sequential perturbations and isolated the corresponding changes in the reflections from each. NMF is a matrix factorization method that can extract scattered and significant features from large high-dimensional datasets. In NMF, the entire set of dose-varying reflections were cast in a matrix-form as a product of two non-negative matrices, describing the correlated sets of reflections and amplitudes of a small number of pure components. The findings indicate that the unperturbed

protein transitions rapidly into multiple sequential components with X-ray exposure corresponding to a dose of 20 MGy under cryogenic conditions. At room temperature, NMF enabled independent isolation of perturbations to the reflections from direct X-ray exposure versus diffusion of molecular radicals generated upon solvent exposure. During room temperature X-ray data collection, the crystals were damaged faster than cryogenic conditions. Application of NMF during the damage mechanism helps in observing the firsthand effects of indirect X-ray radiation around the sample.

REFERENCES

- (1) DiMasi, J. A.; Grabowski, H. G.; Hansen, R. W. Innovation in the Pharmaceutical Industry: New Estimates of R&D Costs. *J. Health Econ.* **2016**, *47*, 20–33. <https://doi.org/10.1016/j.jhealeco.2016.01.012>.
- (2) *Aulton's Pharmaceutics: The Design and Manufacture of Medicines*, 4th ed.; Aulton, M. E., Taylor, K. M. G., Eds.; Churchill Livingstone/Elsevier: Edinburgh, 2013.
- (3) Amidon, G. L.; Lennernäs, H.; Shah, V. P.; Crison, J. R. A Theoretical Basis for a Biopharmaceutic Drug Classification: The Correlation of in Vitro Drug Product Dissolution and in Vivo Bioavailability. *Pharm. Res.* **1995**, *12* (3), 413–420.
- (4) Baghel, S.; Cathcart, H.; O'Reilly, N. J. Polymeric Amorphous Solid Dispersions: A Review of Amorphization, Crystallization, Stabilization, Solid-State Characterization, and Aqueous Solubilization of Biopharmaceutical Classification System Class II Drugs. *J. Pharm. Sci.* **2016**, *105* (9), 2527–2544. <https://doi.org/10.1016/j.xphs.2015.10.008>.
- (5) Fahr, A.; Liu, X. Drug Delivery Strategies for Poorly Water-Soluble Drugs. *Expert Opin. Drug Deliv.* **2007**, *4* (4), 403–416. <https://doi.org/10.1517/17425247.4.4.403>.
- (6) Serajuddin, A. T. Solid Dispersion of Poorly Water-Soluble Drugs: Early Promises, Subsequent Problems, and Recent Breakthroughs. *J. Pharm. Sci.* **1999**, *88* (10), 1058–1066.
- (7) Kennedy, M.; Hu, J.; Gao, P.; Li, L.; Ali-Reynolds, A.; Chal, B.; Gupta, V.; Ma, C.; Mahajan, N.; Akrami, A.; et al. Enhanced Bioavailability of a Poorly Soluble VR1 Antagonist Using an Amorphous Solid Dispersion Approach: A Case Study. *Mol. Pharm.* **2008**, *5* (6), 981–993. <https://doi.org/10.1021/mp800061r>.
- (8) Lehmkomper, K.; Kyeremateng, S. O.; Heinzerling, O.; Degenhardt, M.; Sadowski, G. Long-Term Physical Stability of PVP- and PVPVA-Amorphous Solid Dispersions. *Mol. Pharm.* **2017**, *14* (1), 157–171. <https://doi.org/10.1021/acs.molpharmaceut.6b00763>.
- (9) Van den Mooter, G.; Wuyts, M.; Blaton, N.; Busson, R.; Grobet, P.; Augustijns, P.; Kinget, R. Physical Stabilisation of Amorphous Ketoconazole in Solid Dispersions with Polyvinylpyrrolidone K25. *Eur. J. Pharm. Sci.* **2001**, *12* (3), 261–269. [https://doi.org/10.1016/S0928-0987\(00\)00173-1](https://doi.org/10.1016/S0928-0987(00)00173-1).
- (10) Qian, F.; Huang, J.; Hussain, M. A. Drug–Polymer Solubility and Miscibility: Stability Consideration and Practical Challenges in Amorphous Solid Dispersion Development. *J. Pharm. Sci.* **2010**, *99* (7), 2941–2947. <https://doi.org/10.1002/jps.22074>.
- (11) Yu, L. Amorphous Pharmaceutical Solids: Preparation, Characterization and Stabilization. *Adv. Drug Deliv. Rev.* **2001**, *48* (1), 27–42. [https://doi.org/10.1016/S0169-409X\(01\)00098-9](https://doi.org/10.1016/S0169-409X(01)00098-9).
- (12) Ambike, A. A.; Mahadik, K. R.; Paradkar, A. Spray-Dried Amorphous Solid Dispersions of Simvastatin, a Low Tg Drug: In Vitro and in Vivo Evaluations. *Pharm. Res.* **2005**, *22* (6), 990–998. <https://doi.org/10.1007/s11095-005-4594-z>.
- (13) Gupta, P.; Kakumanu, V. K.; Bansal, A. K. Stability and Solubility of Celecoxib-PVP Amorphous Dispersions: A Molecular Perspective. *Pharm. Res.* **2004**, *21* (10), 1762–1769. <https://doi.org/10.1023/B:PHAM.0000045226.42859.b8>.
- (14) Newman, A.; Engers, D.; Bates, S.; Ivanisevic, I.; Kelly, R. C.; Zograf, G. Characterization of Amorphous API:Polymer Mixtures Using X-Ray Powder Diffraction. *J. Pharm. Sci.* **2008**, *97* (11), 4840–4856. <https://doi.org/10.1002/jps.21352>.

- (15) Yoshihashi, Y.; Iijima, H.; Yonemochi, E.; Terada, K. Estimation of Physical Stability of Amorphous Solid Dispersion Using Differential Scanning Calorimetry. *J. Therm. Anal. Calorim.* **2006**, *85* (3), 689–692. <https://doi.org/10.1007/s10973-006-7653-8>.
- (16) Taylor, L. S.; Zografi, G. [No Title Found]. *Pharm. Res.* **1997**, *14* (12), 1691–1698. <https://doi.org/10.1023/A:1012167410376>.
- (17) Tantishaiyakul, V.; Kaewnopparat, N.; Ingkatawornwong, S. Properties of Solid Dispersions of Piroxicam in Polyvinylpyrrolidone. *Int. J. Pharm.* **1999**, *181* (2), 143–151. [https://doi.org/10.1016/S0378-5173\(99\)00070-8](https://doi.org/10.1016/S0378-5173(99)00070-8).
- (18) Pham, T. N.; Watson, S. A.; Edwards, A. J.; Chavda, M.; Clawson, J. S.; Strohmeier, M.; Vogt, F. G. Analysis of Amorphous Solid Dispersions Using 2D Solid-State NMR and ^1H T_1 Relaxation Measurements. *Mol. Pharm.* **2010**, *7* (5), 1667–1691. <https://doi.org/10.1021/mp100205g>.
- (19) Govender, T. PLGA Nanoparticles Prepared by Nanoprecipitation: Drug Loading and Release Studies of a Water Soluble Drug. *J. Controlled Release* **1999**, *57* (2), 171–185. [https://doi.org/10.1016/S0168-3659\(98\)00116-3](https://doi.org/10.1016/S0168-3659(98)00116-3).
- (20) Kissick, D. J.; Wanapun, D.; Simpson, G. J. Second-Order Nonlinear Optical Imaging of Chiral Crystals. *Annu. Rev. Anal. Chem.* **2011**, *4* (1), 419–437. <https://doi.org/10.1146/annurev.anchem.111808.073722>.
- (21) Rawle, C. B.; Lee, C. J.; Strachan, C. J.; Payne, K.; Manson, P. J.; Rades, T. Towards Characterization and Identification of Solid State Pharmaceutical Mixtures through Second Harmonic Generation. *J. Pharm. Sci.* **2006**, *95* (4), 761–768. <https://doi.org/10.1002/jps.20575>.
- (22) Wampler, R. D.; Kissick, D. J.; Dehen, C. J.; Gualtieri, E. J.; Grey, J. L.; Wang, H.-F.; Thompson, D. H.; Cheng, J.-X.; Simpson, G. J. Selective Detection of Protein Crystals by Second Harmonic Microscopy. *J. Am. Chem. Soc.* **2008**, *130* (43), 14076–14077. <https://doi.org/10.1021/ja805983b>.
- (23) Song, Z.; Sarkar, S.; Vogt, A. D.; Danzer, G. D.; Smith, C. J.; Gualtieri, E. J.; Simpson, G. J. Kinetic Modeling of Accelerated Stability Testing Enabled by Second Harmonic Generation Microscopy. *Anal. Chem.* **2018**, *90* (7), 4406–4413. <https://doi.org/10.1021/acs.analchem.7b04260>.
- (24) Schmitt, P. D.; Trasi, N. S.; Taylor, L. S.; Simpson, G. J. Finding the Needle in the Haystack: Characterization of Trace Crystallinity in a Commercial Formulation of Paclitaxel Protein-Bound Particles by Raman Spectroscopy Enabled by Second Harmonic Generation Microscopy. *Mol. Pharm.* **2015**, *12* (7), 2378–2383. <https://doi.org/10.1021/acs.molpharmaceut.5b00065>.
- (25) Elkhazab, A.; Sarkar, S.; Dinh, J. K.; Simpson, G. J.; Taylor, L. S. Variation in Supersaturation and Phase Behavior of Ezetimibe Amorphous Solid Dispersions upon Dissolution in Different Biorelevant Media. *Mol. Pharm.* **2018**, *15* (1), 193–206. <https://doi.org/10.1021/acs.molpharmaceut.7b00814>.
- (26) Chowdhury, A. U.; Ye, D. H.; Song, Z.; Zhang, S.; Hedderich, H. G.; Mallick, B.; Thirunahari, S.; Ramakrishnan, S.; Sengupta, A.; Gualtieri, E. J.; et al. Second Harmonic Generation Guided Raman Spectroscopy for Sensitive Detection of Polymorph Transitions. *Anal. Chem.* **2017**, *89* (11), 5958–5965. <https://doi.org/10.1021/acs.analchem.7b00431>.
- (27) Kommanaboyina, B.; Rhodes, C. T. Trends in Stability Testing, with Emphasis on Stability During Distribution and Storage. *Drug Dev. Ind. Pharm.* **1999**, *25* (7), 857–868. <https://doi.org/10.1081/DDC-100102246>.

- (28) *Stability of Drugs and Dosage Forms*; Kluwer Academic Publishers: Boston, 2002. <https://doi.org/10.1007/b114443>.
- (29) Wu, L.; Zhang, J.; Watanabe, W. Physical and Chemical Stability of Drug Nanoparticles. *Adv. Drug Deliv. Rev.* **2011**, *63* (6), 456–469. <https://doi.org/10.1016/j.addr.2011.02.001>.
- (30) Lyon, R. C.; Taylor, J. S.; Porter, D. A.; Prasanna, H. R.; Hussain, A. S. Stability Profiles of Drug Products Extended beyond Labeled Expiration Dates. *J. Pharm. Sci.* **2006**, *95* (7), 1549–1560. <https://doi.org/10.1002/jps.20636>.
- (31) Dressman, J. B.; Reppas, C. In Vitro–in Vivo Correlations for Lipophilic, Poorly Water-Soluble Drugs. *Eur. J. Pharm. Sci.* **2000**, *11*, S73–S80. [https://doi.org/10.1016/S0928-0987\(00\)00181-0](https://doi.org/10.1016/S0928-0987(00)00181-0).
- (32) Shah, N. H.; Carvajal, M. T.; Patel, C. I.; Infeld, M. H.; Malick, A. W. Self-Emulsifying Drug Delivery Systems (SEDDS) with Polyglycolyzed Glycerides for Improving in Vitro Dissolution and Oral Absorption of Lipophilic Drugs. *Int. J. Pharm.* **1994**, *106* (1), 15–23. [https://doi.org/10.1016/0378-5173\(94\)90271-2](https://doi.org/10.1016/0378-5173(94)90271-2).
- (33) Leuner, C. Improving Drug Solubility for Oral Delivery Using Solid Dispersions. *Eur. J. Pharm. Biopharm.* **2000**, *50* (1), 47–60. [https://doi.org/10.1016/S0939-6411\(00\)00076-X](https://doi.org/10.1016/S0939-6411(00)00076-X).
- (34) Martinez, M. N.; Amidon, G. L. A Mechanistic Approach to Understanding the Factors Affecting Drug Absorption: A Review of Fundamentals. *J. Clin. Pharmacol.* **2002**, *42* (6), 620–643.
- (35) Guo, Y.; Shalaev, E.; Smith, S. Physical Stability of Pharmaceutical Formulations: Solid-State Characterization of Amorphous Dispersions. *TrAC Trends Anal. Chem.* **2013**, *49*, 137–144. <https://doi.org/10.1016/j.trac.2013.06.002>.
- (36) Oliva, A.; Llabrés, M.; Fariña, J. B. Data Analysis of Kinetic Modelling Used in Drug Stability Studies: Isothermal Versus Nonisothermal Assays. *Pharm. Res.* **2006**, *23* (11), 2595–2602. <https://doi.org/10.1007/s11095-006-9096-0>.
- (37) Sarode, A. L.; Wang, P.; Obara, S.; Worthen, D. R. Supersaturation, Nucleation, and Crystal Growth during Single- and Biphasic Dissolution of Amorphous Solid Dispersions: Polymer Effects and Implications for Oral Bioavailability Enhancement of Poorly Water Soluble Drugs. *Eur. J. Pharm. Biopharm.* **2014**, *86* (3), 351–360. <https://doi.org/10.1016/j.ejpb.2013.10.005>.
- (38) Yang, J.; Grey, K.; Doney, J. An Improved Kinetics Approach to Describe the Physical Stability of Amorphous Solid Dispersions. *Int. J. Pharm.* **2010**, *384* (1–2), 24–31. <https://doi.org/10.1016/j.ijpharm.2009.09.035>.
- (39) Surana, R.; Suryanarayanan, R. Quantitation of Crystallinity in Substantially Amorphous Pharmaceuticals and Study of Crystallization Kinetics by X-Ray Powder Diffractometry. *Powder Diffr.* **2000**, *15* (1), 2–6. <https://doi.org/10.1017/S0885715600010757>.
- (40) Kestur, U. S.; Wanapun, D.; Toth, S. J.; Wegiel, L. A.; Simpson, G. J.; Taylor, L. S. Nonlinear Optical Imaging for Sensitive Detection of Crystals in Bulk Amorphous Powders. *J. Pharm. Sci.* **2012**, *101* (11), 4201–4213. <https://doi.org/10.1002/jps.23280>.
- (41) Breitenbach, J. Melt Extrusion: From Process to Drug Delivery Technology. *Eur. J. Pharm. Biopharm.* **2002**, *54* (2), 107–117. [https://doi.org/10.1016/S0939-6411\(02\)00061-9](https://doi.org/10.1016/S0939-6411(02)00061-9).
- (42) Tho, I.; Liepold, B.; Rosenberg, J.; Maegerlein, M.; Brandl, M.; Fricker, G. Formation of Nano/Micro-Dispersions with Improved Dissolution Properties upon Dispersion of Ritonavir Melt Extrudate in Aqueous Media. *Eur. J. Pharm. Sci.* **2010**, *40* (1), 25–32. <https://doi.org/10.1016/j.ejps.2010.02.003>.

- (43) Lindfors, L.; Forssén, S.; Westergren, J.; Olsson, U. Nucleation and Crystal Growth in Supersaturated Solutions of a Model Drug. *J. Colloid Interface Sci.* **2008**, *325* (2), 404–413. <https://doi.org/10.1016/j.jcis.2008.05.034>.
- (44) Fanfoni, M.; Tomellini, M. The Johnson-Mehl- Avrami-Kohnogorov Model: A Brief Review. *Il Nuovo Cimento D* **1998**, *20* (7–8), 1171–1182. <https://doi.org/10.1007/BF03185527>.
- (45) Kelton, K. F. Analysis of Crystallization Kinetics. *Mater. Sci. Eng. A* **1997**, *226–228*, 142–150. [https://doi.org/10.1016/S0921-5093\(96\)10607-9](https://doi.org/10.1016/S0921-5093(96)10607-9).
- (46) Zhou, D.; Schmitt, E. A.; Zhang, G. G.; Law, D.; Vyazovkin, S.; Wight, C. A.; Grant, D. J. W. Crystallization Kinetics of Amorphous Nifedipine Studied by Model-Fitting and Model-Free Approaches. *J. Pharm. Sci.* **2003**, *92* (9), 1779–1792. <https://doi.org/10.1002/jps.10425>.
- (47) Fang, C.; Bhattarai, N.; Sun, C.; Zhang, M. Functionalized Nanoparticles with Long-Term Stability in Biological Media. *Small* **2009**, *5* (14), 1637–1641. <https://doi.org/10.1002/smll.200801647>.
- (48) Neuberger, T.; Schöpf, B.; Hofmann, H.; Hofmann, M.; von Rechenberg, B. Superparamagnetic Nanoparticles for Biomedical Applications: Possibilities and Limitations of a New Drug Delivery System. *J. Magn. Magn. Mater.* **2005**, *293* (1), 483–496. <https://doi.org/10.1016/j.jmmm.2005.01.064>.
- (49) Wang, S.; Xu, T.; Yang, Y.; Shao, Z. Colloidal Stability of Silk Fibroin Nanoparticles Coated with Cationic Polymer for Effective Drug Delivery. *ACS Appl. Mater. Interfaces* **2015**, *7* (38), 21254–21262. <https://doi.org/10.1021/acsami.5b05335>.
- (50) Yang, Z.; Nollenberger, K.; Albers, J.; Moffat, J.; Craig, D.; Qi, S. The Effect of Processing on the Surface Physical Stability of Amorphous Solid Dispersions. *Eur. J. Pharm. Biopharm.* **2014**, *88* (3), 897–908. <https://doi.org/10.1016/j.ejpb.2014.07.013>.
- (51) Sun, Y.; Zhu, L.; Wu, T.; Cai, T.; Gunn, E. M.; Yu, L. Stability of Amorphous Pharmaceutical Solids: Crystal Growth Mechanisms and Effect of Polymer Additives. *AAPS J.* **2012**, *14* (3), 380–388. <https://doi.org/10.1208/s12248-012-9345-6>.
- (52) Li, L.; Fijneman, A. J.; Kaandorp, J. A.; Aizenberg, J.; Noorduyn, W. L. Directed Nucleation and Growth by Balancing Local Supersaturation and Substrate/Nucleus Lattice Mismatch. *Proc. Natl. Acad. Sci.* **2018**, *115* (14), 3575–3580. <https://doi.org/10.1073/pnas.1712911115>.
- (53) Wanapun, D.; Kestur, U. S.; Taylor, L. S.; Simpson, G. J. Single Particle Nonlinear Optical Imaging of Trace Crystallinity in an Organic Powder. *Anal. Chem.* **2011**, *83* (12), 4745–4751. <https://doi.org/10.1021/ac1031397>.
- (54) Gardner, C. R.; Almarsson, O.; Chen, H.; Morissette, S.; Peterson, M.; Zhang, Z.; Wang, S.; Lemmo, A.; Gonzalez-Zugasti, J.; Monagle, J.; et al. Application of High Throughput Technologies to Drug Substance and Drug Product Development. *Comput. Chem. Eng.* **2004**, *28* (6–7), 943–953. <https://doi.org/10.1016/j.compchemeng.2003.09.028>.
- (55) Widjaja, E.; Kanaujia, P.; Lau, G.; Ng, W. K.; Garland, M.; Saal, C.; Hanefeld, A.; Fischbach, M.; Maio, M.; Tan, R. B. H. Detection of Trace Crystallinity in an Amorphous System Using Raman Microscopy and Chemometric Analysis. *Eur. J. Pharm. Sci.* **2011**, *42* (1–2), 45–54. <https://doi.org/10.1016/j.ejps.2010.10.004>.
- (56) Mahlin, D.; Berggren, J.; Alderborn, G.; Engström, S. Moisture-Induced Surface Crystallization of Spray-Dried Amorphous Lactose Particles Studied by Atomic Force Microscopy. *J. Pharm. Sci.* **2004**, *93* (1), 29–37. <https://doi.org/10.1002/jps.10503>.
- (57) Wu, T.; Sun, Y.; Li, N.; de Villiers, M. M.; Yu, L. Inhibiting Surface Crystallization of Amorphous Indomethacin by Nanocoating. *Langmuir* **2007**, *23* (9), 5148–5153. <https://doi.org/10.1021/la070050i>.

- (58) Raghavan, S. L.; Ristic, R. I.; Sheen, D. B.; Sherwood, J. N. The Bulk Crystallization of A-lactose Monohydrate from Aqueous Solution. *J. Pharm. Sci.* **2001**, *90* (7), 823–832. <https://doi.org/10.1002/jps.1036>.
- (59) Zhu, L.; Wong, L.; Yu, L. Surface-Enhanced Crystallization of Amorphous Nifedipine. *Mol. Pharm.* **2008**, *5* (6), 921–926. <https://doi.org/10.1021/mp8000638>.
- (60) Wanapun, D.; Kestur, U. S.; Kissick, D. J.; Simpson, G. J.; Taylor, L. S. Selective Detection and Quantitation of Organic Molecule Crystallization by Second Harmonic Generation Microscopy. *Anal. Chem.* **2010**, *82* (13), 5425–5432. <https://doi.org/10.1021/ac100564f>.
- (61) Kesisoglou, F.; Wu, Y. Understanding the Effect of API Properties on Bioavailability Through Absorption Modeling. *AAPS J.* **2008**, *10* (4), 516–525. <https://doi.org/10.1208/s12248-008-9061-4>.
- (62) Smith, C. J.; Dinh, J.; Schmitt, P. D.; Stroud, P. A.; Hinds, J.; Johnson, M. J.; Simpson, G. J. Calibration-Free Second Harmonic Generation (SHG) Image Analysis for Quantification of Trace Crystallinity Within Final Dosage Forms of Amorphous Solid Dispersions. *Appl. Spectrosc.* **2018**, *72* (11), 1594–1605. <https://doi.org/10.1177/0003702818786506>.
- (63) Alonzo, D. E.; Gao, Y.; Zhou, D.; Mo, H.; Zhang, G. G. Z.; Taylor, L. S. Dissolution and Precipitation Behavior of Amorphous Solid Dispersions. *J. Pharm. Sci.* **2011**, *100* (8), 3316–3331. <https://doi.org/10.1002/jps.22579>.
- (64) Kanaujia, P.; Poovizhi, P.; Ng, W. K.; Tan, R. B. H. Amorphous Formulations for Dissolution and Bioavailability Enhancement of Poorly Soluble APIs. *Powder Technol.* **2015**, *285*, 2–15. <https://doi.org/10.1016/j.powtec.2015.05.012>.
- (65) Alonzo, D. E.; Zhang, G. G. Z.; Zhou, D.; Gao, Y.; Taylor, L. S. Understanding the Behavior of Amorphous Pharmaceutical Systems during Dissolution. *Pharm. Res.* **2010**, *27* (4), 608–618. <https://doi.org/10.1007/s11095-009-0021-1>.
- (66) Badawy, S. I. F.; Hussain, M. A. Microenvironmental PH Modulation in Solid Dosage Forms. *J. Pharm. Sci.* **2007**, *96* (5), 948–959. <https://doi.org/10.1002/jps.20932>.
- (67) Vasconcelos, T.; Sarmiento, B.; Costa, P. Solid Dispersions as Strategy to Improve Oral Bioavailability of Poor Water Soluble Drugs. *Drug Discov. Today* **2007**, *12* (23–24), 1068–1075. <https://doi.org/10.1016/j.drudis.2007.09.005>.
- (68) Miller, J. M.; Beig, A.; Carr, R. A.; Spence, J. K.; Dahan, A. A Win–Win Solution in Oral Delivery of Lipophilic Drugs: Supersaturation via Amorphous Solid Dispersions Increases Apparent Solubility without Sacrifice of Intestinal Membrane Permeability. *Mol. Pharm.* **2012**, *9* (7), 2009–2016. <https://doi.org/10.1021/mp300104s>.
- (69) Konno, H.; Taylor, L. S. Influence of Different Polymers on the Crystallization Tendency of Molecularly Dispersed Amorphous Felodipine. *J. Pharm. Sci.* **2006**, *95* (12), 2692–2705. <https://doi.org/10.1002/jps.20697>.
- (70) Wegiel, L. A.; Mauer, L. J.; Edgar, K. J.; Taylor, L. S. Crystallization of Amorphous Solid Dispersions of Resveratrol during Preparation and Storage—Impact of Different Polymers. *J. Pharm. Sci.* **2013**, *102* (1), 171–184. <https://doi.org/10.1002/jps.23358>.
- (71) Overhoff, K. A.; Moreno, A.; Miller, D. A.; Johnston, K. P.; Williams, R. O. Solid Dispersions of Itraconazole and Enteric Polymers Made by Ultra-Rapid Freezing. *Int. J. Pharm.* **2007**, *336* (1), 122–132. <https://doi.org/10.1016/j.ijpharm.2006.11.043>.
- (72) Hörter, D.; Dressman, J. B. Influence of Physicochemical Properties on Dissolution of Drugs in the Gastrointestinal Tract. *Adv. Drug Deliv. Rev.* **2001**, *46* (1–3), 75–87. [https://doi.org/10.1016/S0169-409X\(00\)00130-7](https://doi.org/10.1016/S0169-409X(00)00130-7).

- (73) Hörter, D.; Dressman, J. B. Influence of Physicochemical Properties on Dissolution of Drugs in the Gastrointestinal Tract. *Adv. Drug Deliv. Rev.* **1997**, *25* (1), 3–14. [https://doi.org/10.1016/S0169-409X\(96\)00487-5](https://doi.org/10.1016/S0169-409X(96)00487-5).
- (74) Brouwers, J.; Brewster, M. E.; Augustijns, P. Supersaturating Drug Delivery Systems: The Answer to Solubility-Limited Oral Bioavailability? *J. Pharm. Sci.* **2009**, *98* (8), 2549–2572. <https://doi.org/10.1002/jps.21650>.
- (75) Kostewicz, E. S.; Wunderlich, M.; Brauns, U.; Becker, R.; Bock, T.; Dressman, J. B. Predicting the Precipitation of Poorly Soluble Weak Bases upon Entry in the Small Intestine. *J. Pharm. Pharmacol.* **2004**, *56* (1), 43–51. <https://doi.org/10.1211/0022357022511>.
- (76) Courtney, R.; Radwanski, E.; Lim, J.; Laughlin, M. Pharmacokinetics of Posaconazole Coadministered with Antacid in Fasting or Nonfasting Healthy Men. *Antimicrob. Agents Chemother.* **2004**, *48* (3), 804–808. <https://doi.org/10.1128/AAC.48.3.804-808.2004>.
- (77) Gane, P. J.; Dean, P. M. Recent Advances in Structure-Based Rational Drug Design. *Curr. Opin. Struct. Biol.* **2000**, *10* (4), 401–404. [https://doi.org/10.1016/S0959-440X\(00\)00105-6](https://doi.org/10.1016/S0959-440X(00)00105-6).
- (78) Sunde, M.; Serpell, L. C.; Bartlam, M.; Fraser, P. E.; Pepys, M. B.; Blake, C. C. F. Common Core Structure of Amyloid Fibrils by Synchrotron X-Ray Diffraction 1 Edited by F. E. Cohen. *J. Mol. Biol.* **1997**, *273* (3), 729–739. <https://doi.org/10.1006/jmbi.1997.1348>.
- (79) Ravelli, R.; Garman, E. Radiation Damage in Macromolecular Cryocrystallography. *Curr. Opin. Struct. Biol.* **2006**, *16* (5), 624–629. <https://doi.org/10.1016/j.sbi.2006.08.001>.
- (80) Weik, M.; Ravelli, R. B. G.; Kryger, G.; McSweeney, S.; Raves, M. L.; Harel, M.; Gros, P.; Silman, I.; Kroon, J.; Sussman, J. L. Specific Chemical and Structural Damage to Proteins Produced by Synchrotron Radiation. *Proc. Natl. Acad. Sci.* **2000**, *97* (2), 623–628. <https://doi.org/10.1073/pnas.97.2.623>.
- (81) Cryo-Protection of Protein Crystals against Radiation Damage in Electron and X-Ray Diffraction. *Proc. R. Soc. Lond. B Biol. Sci.* **1990**, *241* (1300), 6–8. <https://doi.org/10.1098/rspb.1990.0057>.
- (82) Harp, J. M.; Timm, D. E.; Bunick, G. J. Macromolecular Crystal Annealing: Overcoming Increased Mosaicity Associated with Cryocrystallography. *Acta Crystallogr. D Biol. Crystallogr.* **1998**, *54* (4), 622–628. <https://doi.org/10.1107/S09074444997019008>.
- (83) Diederichs, K. Some Aspects of Quantitative Analysis and Correction of Radiation Damage. *Acta Crystallogr. D Biol. Crystallogr.* **2006**, *62* (1), 96–101. <https://doi.org/10.1107/S09074444905031537>.
- (84) Diederichs, K.; McSweeney, S.; Ravelli, R. B. G. Zero-Dose Extrapolation as Part of Macromolecular Synchrotron Data Reduction. *Acta Crystallogr. D Biol. Crystallogr.* **2003**, *59* (5), 903–909. <https://doi.org/10.1107/S09074444903006516>.
- (85) Sanishvili, R.; Yoder, D. W.; Pothineni, S. B.; Rosenbaum, G.; Xu, S.; Vogt, S.; Stepanov, S.; Makarov, O. A.; Corcoran, S.; Benn, R.; et al. Radiation Damage in Protein Crystals Is Reduced with a Micron-Sized X-Ray Beam. *Proc. Natl. Acad. Sci.* **2011**, *108* (15), 6127–6132. <https://doi.org/10.1073/pnas.1017701108>.
- (86) Sutter, J. P.; Alcock, S. G.; Kashyap, Y.; Nistea, I.; Wang, H.; Sawhney, K. Creating Flat-Top X-Ray Beams by Applying Surface Profiles of Alternating Curvature to Deformable Piezo Bimorph Mirrors. *J. Synchrotron Radiat.* **2016**, *23* (6), 1333–1347. <https://doi.org/10.1107/S1600577516013308>.
- (87) Spence, J. C. H. XFELs for Structure and Dynamics in Biology. *IUCrJ* **2017**, *4* (4), 322–339. <https://doi.org/10.1107/S2052252517005760>.

- (88) Yaoi, M.; Adachi, H.; Takano, K.; Matsumura, H.; Inoue, T.; Mori, Y.; Sasaki, T. Effect of Stirring Method on Protein Crystallization. *Jpn. J. Appl. Phys.* **2004**, *43* (No. 10A), L1318–L1319. <https://doi.org/10.1143/JJAP.43.L1318>.
- (89) Dettmar, C. M.; Newman, J. A.; Toth, S. J.; Becker, M.; Fischetti, R. F.; Simpson, G. J. Imaging Local Electric Fields Produced upon Synchrotron X-Ray Exposure. *Proc. Natl. Acad. Sci.* **2015**, *112* (3), 696–701. <https://doi.org/10.1073/pnas.1407771112>.
- (90) Norman, S.; Maeder, M. Model-Based Analysis for Kinetic and Equilibrium Investigations. *Crit. Rev. Anal. Chem.* **2006**, *36* (3–4), 199–209. <https://doi.org/10.1080/10408340600969619>.

VITA

Sreya Sarkar was born to Mrs. Mala Sarkar and Mr. Manoranjan Sarkar in Kolkata, India on January 31, 1992. Sreya obtained her bachelor's degree in Chemistry (Honors.) with minor in Physics and Mathematics from Lady Brabourne College, India in 2012. Later on, she attended Indian Institute of Technology Madras, India, where she graduated with MS in Chemistry in 2014 and worked with Prof. T. Pradeep for the isolation and mass spectral identification of alloy clusters. Sreya joined Purdue in Fall 2014, where she is working in Prof. Garth Simpson's lab, specialization in characterization of physicochemical and biopharmaceutical properties of small molecules using state-of-the-art analytical methods, and data analysis to support formulation design and drug product development.

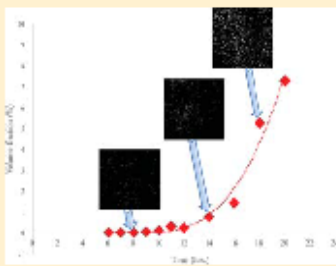
PUBLICATIONS

Kinetic Modeling of Accelerated Stability Testing Enabled by Second Harmonic Generation Microscopy

Zhengtian Song,^{†,‡,||} Sreya Sarkar,^{†,‡,||} Andrew D. Vogt,[†] Gerald D. Danzer,[†] Casey J. Smith,[†] Ellen J. Gualtieri,[§] and Garth J. Simpson^{*,†,||}[†]Department of Chemistry, Purdue University, 560 Oval Drive, West Lafayette, Indiana 47906, United States[‡]AbbVie Inc., 1 North Waukegan Road, North Chicago, Illinois 60064, United States[§]Formulatrix, Inc., 10 DeAngelo Drive, Bedford, Massachusetts 01730, United States

Supporting Information

ABSTRACT: The low limits of detection afforded by second harmonic generation (SHG) microscopy coupled with image analysis algorithms enabled quantitative modeling of the temperature-dependent crystallization of active pharmaceutical ingredients (APIs) within amorphous solid dispersions (ASDs). ASDs, in which an API is maintained in an amorphous state within a polymer matrix, are finding increasing use to address solubility limitations of small-molecule APIs. Extensive stability testing is typically performed for ASD characterization, the time frame for which is often dictated by the earliest detectable onset of crystal formation. Here a study of accelerated stability testing on ritonavir, a human immunodeficiency virus (HIV) protease inhibitor, has been conducted. Under the condition for accelerated stability testing at 50 °C/75%RH and 40 °C/75%RH, ritonavir crystallization kinetics from amorphous solid dispersions were monitored by SHG microscopy. SHG microscopy coupled by image analysis yielded limits of detection for ritonavir crystals as low as 10 ppm, which is about 2 orders of magnitude lower than other methods currently available for crystallinity detection in ASDs. The four decade dynamic range of SHG microscopy enabled quantitative modeling with an established (JMAK) kinetic model. From the SHG images, nucleation and crystal growth rates were independently determined.



Many emerging drug candidates exhibit low aqueous solubility, which can directly impact bioavailability and ultimately efficacy. In such cases, the bioavailability of an active pharmaceutical ingredient (API) is routinely improved by rendering the API amorphous within a polymer matrix to form an amorphous solid dispersion (ASD).^{1,2} However, ASDs are generally metastable systems; spontaneous crystallization of the API during storage at elevated relative humidity, for example, or processing can negatively impact the bioavailability of the API. The effective dose of a formulation may be lower than the intended dose. Furthermore, residual crystals present upon dissolution may serve as nuclei for recrystallization following dissolution under conditions of supersaturation.³ To mitigate these complications, extensive accelerated stability testing methods are currently performed to quantify trace crystallinity present in ASDs under stressed conditions, as stability testing under ambient conditions is prohibitively time-consuming.^{4,5}

In principle, kinetic modeling at elevated temperatures and humidity can be used to predict stability under ambient conditions, which is ultimately the defining property of interest.^{6,7} Two key kinetic processes are most directly relevant: molecular diffusion and crystal nucleation/growth. Parameterized models for nucleation and growth allow prediction of time-dependent crystallization under ambient conditions.⁸

Given the exponential dependence of the crystallinity on many of the recovered parameters, experimental uncertainties can have large impacts on the predicted behaviors. Confident determination of reliable kinetic parameters is most directly obtained through acquisition over a large range of concentrations, suggesting the need for sensitive methods capable of quantification at the early stages of crystallization. Kinetic modeling is arguably the simplest to interpret from measurements acquired in the low crystallinity regime, in which local depletion and concentration gradients are negligible. The relatively low drug loading present in many ASDs further exacerbates the challenges in acquisition of kinetic data over a large dynamic range.

The most common benchtop methods for characterizing crystallinity in situ for kinetic modeling routinely exhibit limits of detection within 1 order of magnitude of the total drug loading, greatly reducing the accessible dynamic range for quantifying crystallinity. A suite of methods is typically brought to bear to inform stability assessments of ASDs, including

Received: October 16, 2017

Accepted: March 5, 2018

Published: March 5, 2018

polarized light microscopy (PLM),⁹ differential scanning calorimetry (DSC),^{10,11} X-ray powder diffraction (XRPD),¹² and solid-state NMR spectroscopy (ssNMR).^{13,14} PLM is arguably the most common method currently used to detect crystallinity in ASDs during stability testing. However, it only provides qualitative information on optically transparent samples for Boolean assessments and routinely exhibits interferences by occlusions, contaminants, and other crystalline excipients.⁹ DSC can provide information about thermal processes such as solid–solid transition but lacks the sensitivity to allow trace detection.¹⁵ XRPD, the current gold-standard method for crystallinity, detection also suffers from a relatively high detection limit.¹⁶ Detection of crystallinity below 1% is challenging for the above analytical techniques.¹⁵ Solid-state NMR has been used to quantitatively determine all components in ASDs¹³ with detection limits as low as 0.4% for carbon.¹⁴ However, ssNMR is costly and requires a relatively long sample analysis times.

Nonlinear optical imaging has recently emerged as a successful method in the pharmaceutical field for the sensitive detection of trace crystallization in amorphous systems.^{17–19} Second harmonic generation (SHG), in particular, is a scattering process, in which the incoming light is converted to light of twice the frequency.²⁰ The particular symmetry properties of SHG only permit this second-order process in noncentrosymmetric systems such as chiral crystals, whereas amorphous systems do not generate a coherent SHG signal and negligible background.^{21–23} SHG microscopy has been demonstrated as a powerful method for the detection of noncentrosymmetric crystals with low detection limits, which shows high potential for accelerated stability testing of ASDs.¹⁷

Ritonavir is an active ingredient in many successful anti-HIV formulations with extensively studied crystallization kinetics.^{24,25} Given the rich phase behavior of ritonavir, a substantial body of literature has accumulated for modeling crystallization of amorphous ritonavir, both as a pure compound and as an amorphous formulation. In a recent study centered on crystallization of ritonavir and formulations containing amorphous ritonavir, Zhu et al.²⁶ performed a series of stability experiments to develop predictive models for ritonavir crystallization behaviors, as a case study. The kinetic modeling was performed based on determination of the induction time, corresponding to the minimum time required to detect onset of crystallization.

In this work, we seek to significantly expand upon the results of the preceding studies with ritonavir to interrogate the early stage ($\leq 1\%$) crystalline regime by SHG microscopy. Accelerated stability testing has been carried out on a model ritonavir-ASD to determine the detection of limit of SHG microscopy and assess the utility of the approach for informing kinetic modeling of crystal nucleation and growth. Specifically, the primary objective of the present work is the development of parametrized models for early stage crystal nucleation and growth kinetics that can be used for quantitatively assessing the anticipated stability under ambient conditions.

METHODS

Amorphous ritonavir extrudate with 15% (w/w) ritonavir (manufactured by AbbVie), copovidone (BASF), plasticizer/surfactant, and silicon dioxide was prepared by hot melt extrusion, as previously described^{27,28} and then milled to a powder. The dry glass transition temperature of the milled extrudate was 56 °C, as measured by DSC. For the studies

described herein, samples were prepared by placing powdered extrudates on the glass slides as a thin layer ($\sim 300\ \mu\text{m}$) over a sample area of $\sim 1\ \text{cm}^2$. For accelerated stability testing, samples were stressed at 50 °C/75% relative humidity (RH) or 40 °C/75% RH. SHG microscopy was used to observe the crystallization of stressed amorphous ritonavir at early times (0 to 24 h). At this RH, the extrudates exhibited low turbidity, suggestive of temperatures above the glass transition temperature. High RH is known to suppress the glass transition temperature of copovidone.²⁹

SHG images were acquired by using a commercial SONICC (second-order nonlinear optical imaging of chiral crystals) microscope (Formulatrix, Inc.), modified in-house for compatibility with powder analysis. Specifically, the instrument was redesigned to allow epi-detection of SHG (details shown in the Supporting Information). The system was powered by a Fianium FemtoPower laser (1060 nm, 170 fs, 50 MHz). A resonant mirror (8 kHz) and a galvanometer mirror are used for beam scanning to generate SHG images. In this study, all of the SHG images were acquired with 350 mW excitation laser power at the sample, and each field of view was $\sim 2.0\ \text{mm} \times 2.0\ \text{mm}$. This power level is significantly higher than typically used in NLO microscopy measurements of tissue samples. However, the power density at the sample was relatively low, as all measurements were acquired with a low numerical aperture objective (NA = 0.3) over a large field of view ($>4\ \text{mm}^2$). Furthermore, the use of a fast-scan (8 kHz) resonant mirror with the beam blocked at the turning points reduced the single-pass exposure for each pixel to $\sim 50\ \text{ns}$ (or approximately 2–3 laser pulses) per scan and then allowed for 1/30 s of thermal relaxation prior to subsequent sampling. For unstressed samples, the SHG signal was collected in the epi direction (i.e., back through the same objective used to deliver the infrared beam), as powders typically generate little signal in transmission due to optical scattering. For the ritonavir milled extrudate samples stressed at either 50 or 40 °C with 75%RH, the SHG signal was collected in transmission. Two replicates of each sample were prepared, and three different positions of each sample were observed for a total of six fields of view obtained for each time-point. ImageJ was used to analyze the SHG images based on particle counting analysis as described previously.⁹

THEORY

Crystal growth rates can be independently and self-consistently modeled in terms of nucleation and diffusion-limited growth. Parameterized models for nucleation and fundamental models for growth allow prediction of time-dependent crystallization. The overall crystallization kinetics under isothermal conditions can be described by JMAK (Johnson, Mehl, Avrami, and Kolmogorov) theory in terms of volume fraction of the new phase under the assumption that nucleation and growth rates are constant throughout the transformation.^{30,31} In this theory, the volume fraction of the new phase, α , is proposed by eq 1, in which t is time, t_0 is the induction time and is defined as the earliest detection of an SHG signal, I is the nucleation rate, and U is the crystal growth rate.

$$\alpha(t - t_0) = 1 - \exp\left\{-g \int_{t_0}^t I(t') \left[\int_{t'}^t U(t'') dt'' \right]^3 dt'\right\} \quad (1)$$

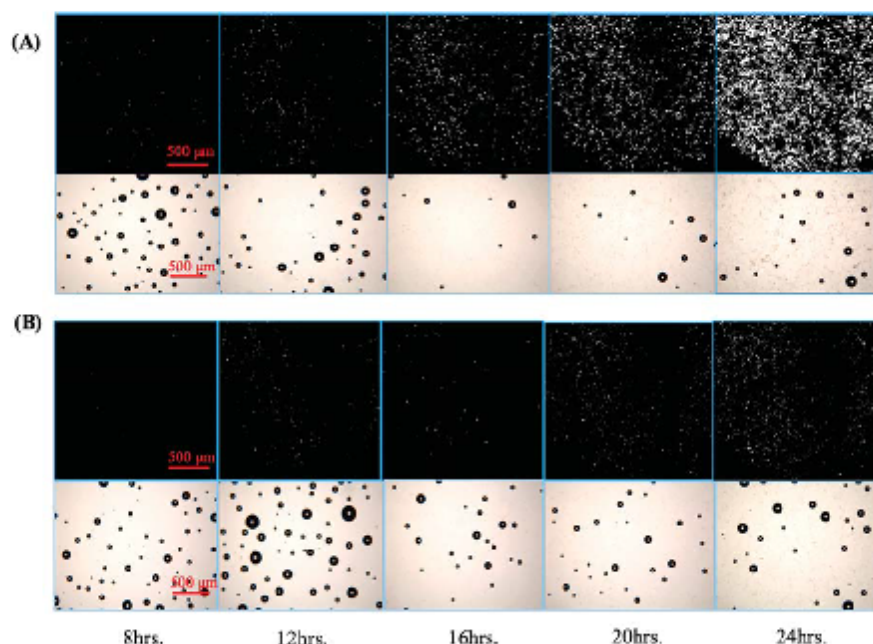


Figure 1. SHG and bright field images for time-dependent crystal growth in 15% atazanavir milled extrudate stressed in (A) 50 °C/75% RH and (B) 40 °C/75% RH chambers. The spherical occlusions in the bright field images correspond to air pockets within the partially melted copovidone matrix. After ~16 h, crystals can be observed by bright field imaging with low contrast.

For spherical crystals, the shape-factor g is $4\pi/3$. For steady-state homogeneous nucleation, nucleation and growth rates are considered to be constant; therefore, eq 1 can be rewritten as eq 2.

$$\alpha(t - t_0) = 1 - \exp\left[-\frac{gIU^3(t - t_0)^4}{4}\right] \quad (2)$$

The assumption of constant nucleation and growth rates are only expected to rigorously hold at the early stages of crystallization ($\ll 1\%$), for which the concentration of amorphous API is not significantly affected by the crystalline fraction. The assumption of approximately spherical particles may initially appear to be questionable given that pristine single crystals exhibit diverse habits. For high aspect ratio needle-like crystals, this assumption will no longer be valid. However, the ritonavir particles studied in the present case exhibit aspect ratios of less than 3, which is common in many pharmaceutically desirable materials given the challenges of manufacturing associated with needle-like crystals. In this range, the error introduced by assumption of approximately spheroidal particles is insignificant relative to the Poisson uncertainty introduced by the finite number of discrete crystals sampled.

The volume fraction of the transformed material can be recovered by simplification of the more general form of the JMAK equation as shown in eq 3 by grouping constants and generalizing the exponential to an adjustable parameter.³⁰

$$\alpha(t - t_0) = 1 - \exp(-K(t - t_0)^n) \quad (3)$$

The parameter n is the Avrami coefficient and depends on both nucleation and crystal growth rates and thus from the formulas $N \propto (t - t_0)^2$ and $r \propto (t - t_0)^m$, which describe the variation in crystal number (N) and crystal size (r) with time.³⁰ The Avrami coefficient can be given by the following eq 4.

$$n = k + 3m \quad (4)$$

The preceding expressions hold at a particular temperature, but stability testing is most commonly performed at as a function of temperature in order to induce phase transformations in practical time scales. Connecting these accelerated stability test results back to room temperature behavior can be performed by considering the temperature dependence of diffusion and crystal growth. The growth rate of an individual crystal U (described by m in eq 4) can be parametrized and related back to diffusion and the Gibbs free energy of crystallization through eq 5.³⁰ In that equation, ΔG_v is the thermodynamic Gibbs free energy per unit volume of crystal, a is an average (effective) size parameter of the molecules building the crystalline phase, k_B is Boltzman's constant, and f is a dimensionless parameter describing the different growth modes. For the continuous growth mechanism, which is assumed that the interface between the growing crystal and the surrounding medium displays a sufficiently high concentration of growth sites, $f = 1$.³¹ U is the crystal growth rate, which is the slope from a plot of the mean crystal radius with time.

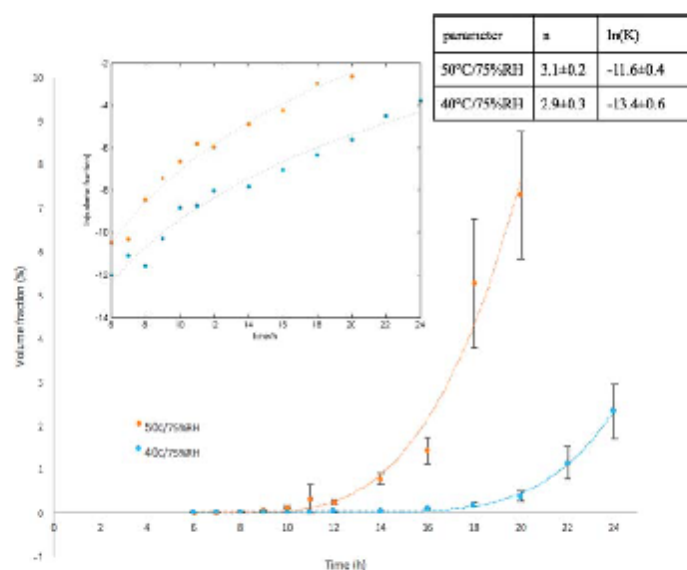


Figure 2. Percent volume fraction of crystallinity from 15% amorphous ritonavir milled extrudate at different stress conditions showing the formation and evolution of crystals with time and detection limits as low as 10 ppm (0.001%) of the total drug load.

$$U = f \frac{D}{4a} \left[1 - \exp\left(-\frac{1}{2} \frac{\Delta G_V a^3}{k_B T}\right) \right] \quad (5)$$

In practice, the expression in eq 5 can often be simplified if either diffusion limits the growth rate (in which case D dictates the overall kinetics) or if the Gibbs free energy term in the exponential represented by ΔG_V dictates the crystallization rate. Since the supersaturation decreases with increasing temperature, growth rates would be expected to decrease at elevated temperatures for crystallization under thermodynamic control. Under diffusion-limited growth conditions, the kinetics obey standard Arrhenius behaviors for diffusion $D = D_0 e^{-E_a/k_B T}$ at intermediate and lower temperatures.

The expression in eq 5 allows prediction of the growth rates at temperatures other than those measured. Extrapolation from elevated temperature behavior to ambient conditions can provide a means for evaluating potential stability of ASDs, provided that no additional phase transformations arise over temperatures not interrogated experimentally.

RESULTS AND DISCUSSIONS

Under the condition for accelerated stability testing at both 50 °C/75% RH and 40 °C/75% RH, crystal growth kinetics from the 15% w/w amorphous ritonavir milled extrudate was recorded by collecting SHG images on a scheduled basis. Ten representative SHG images and corresponding bright field images are shown in Figure 1. All of the images are shown with the same brightness scale for comparative purposes. The SHG micrographs even at the earliest stages shown in the figure yield signals well above the noise floor of the instrument (i.e., particles with >3 contiguous pixels exhibiting counts >3 counts). The time-zero samples showed no detectable SHG,

with the onset of detectable SHG at 5 h for samples stressed at 50 °C/75% RH and 40 °C/75% RH. Compared with SHG-active particles shown in Figure 1B, the number and the average size of SHG-active particles are larger as shown in Figure 1A, which form the basis of more detailed kinetic analysis (vide infra).

The 15% drug loading (DL) ritonavir milled extrudate samples contained only amorphous ritonavir and copovidone. Neither of the components is SHG-active. Ritonavir crystals are noncentrosymmetric and SHG active.^{23,32} For SHG images in Figure 1, the SHG-active areas represent ritonavir crystals. Based on the comparison of Figure 1A,B, after the same stressed time, the milled extrudate stressed at 50 °C/75% RH developed more ritonavir crystals with larger size than did the sample stressed at 40 °C/75% RH.

A particle counting approach was used to quantify crystallinity at levels from ppm regime to 10%, which corrected particle–particle overlap. In brief, the volume of each individual crystallite was estimated based on the cross-sectional area of the particle. This approach removes noise associated with variance in the SHG intensity from differences in crystal orientation. Bias introduced from particle overlap for crystallinities >1% was removed using a size-distribution dependent correction algorithm detailed elsewhere.³² Although the algorithm as described is formally derived assuming spherical particles, the aspect ratio of the ritonavir particles (~3:1) is sufficiently low to allow reliable application of the method in the present study. A minimum crystal cross-sectional area of 45 μm^2 (corresponding to three contiguous pixels) was implemented in the algorithm to ensure statistical confidence in crystal identification by image analysis. Based on the volume sampled as set by the depth of field and the field of view, this algorithm places a practical lower limit of ~0.5 ppm for detection of crystallinity.

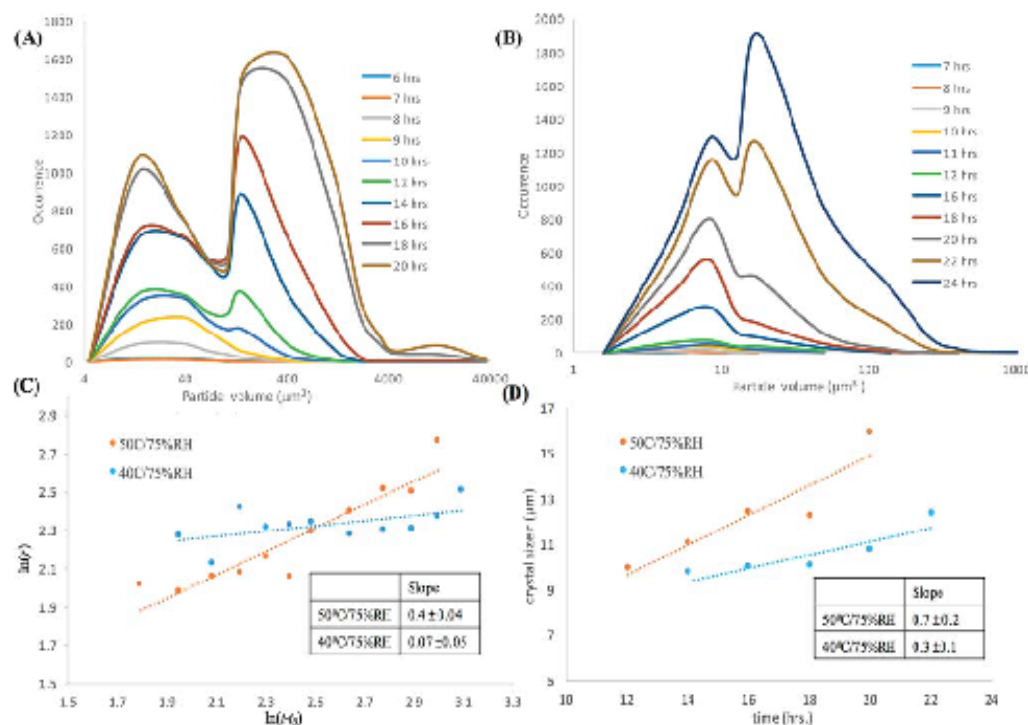


Figure 3. Crystal growth rate: Time-dependent ritonavir crystal particle size distribution at (A) 50 °C/75%RH and (B) 40 °C/75%RH; (C) crystal growth rate depicted by $\ln(r)$ vs $\ln(t - t_0)$ plot; (D) crystal growth rate for latest five time points.

This limit is substantially higher than has been reported previously based on the minimum detectable radius of 100 nm. However, Poisson statistics associated with the stochastic nature of crystallization were found to be the dominant noise source in the analysis, which were minimized by maximizing both the depth of field and field of view. Despite the high limit of detection (LoD) imposed by the particle-counting algorithm relative to previous work, SHG still produced an LoD several orders of magnitude lower than practically achievable by alternative routine benchtop methods.

Figure 2 shows the volume fraction of crystallinity from 15% amorphous ritonavir milled extrudate stressed at 50 °C/75% RH (orange) or 40 °C/75% RH (blue) and corresponding fits to eq 3. The crystallization rates were clearly not linear with each condition, exhibiting a significant induction time, which is tentatively attributed to the stochastic nature of nucleation coupled with the need to generate particles large enough to generate significant SHG (>100 nm) for detection.¹⁵ In this study, the induction time t_0 was approximately 5 h for both samples stressed at 50 °C/75% RH and 40 °C/75% RH, which was the earliest time point at which the SHG was detected with statistical confidence (i.e., with a signal greater than 3-fold higher than the standard deviation of the blank).

The limits of detection based on SHG microscopy are defined to be the concentration corresponding to a signal 3-fold higher than the standard deviation of the initially prepared samples. In Figure 2, the lower-limit for the SHG response is

also shown on a log-scale in the inset figure, consistent with the form in eq 3, calculated with the measured induction times. Both sets of fits (linear and log scaling) are shown with identical parameters in each case, given in the inset table. From the 40 °C fits, SHG microscopy exhibited a lower detection limit of 10 ppm (v/v) for crystalline ritonavir in a milled extrudate powder, which is approximately 2 to 3 orders of magnitude lower than commonly used methods (DSC, XRPD, near IR). Given the similarities in the densities of copovidone and ritonavir, the volume ratio and the mass fraction are essentially identical.

With knowledge of the induction time, additional insights into the crystallization behavior can be recovered from particle-counting analysis of the SHG images, shown in Figure 3. The top part of the figure contains the histogram of particle sizes, indicating an increase in both the number of crystals and the distribution of crystal sizes with time. To assess the crystal growth rate, the mean crystal radii were calculated by using the mean crystal size from the distribution. The time-dependent evolutions of the mean crystal radius were given by the bottom two plots. A log-log plot of mean crystal radius versus time in Figure 3C was used to extract the exponential scaling parameter m , assuming that the particle size scales as $r \propto (t - t_0)^m$. This scaling is consistent with expectations for the derivation of eq 4. An estimate of the steady-state growth rate was generated from the latest five time points under each of the two stressed conditions as shown in Figure 3D.

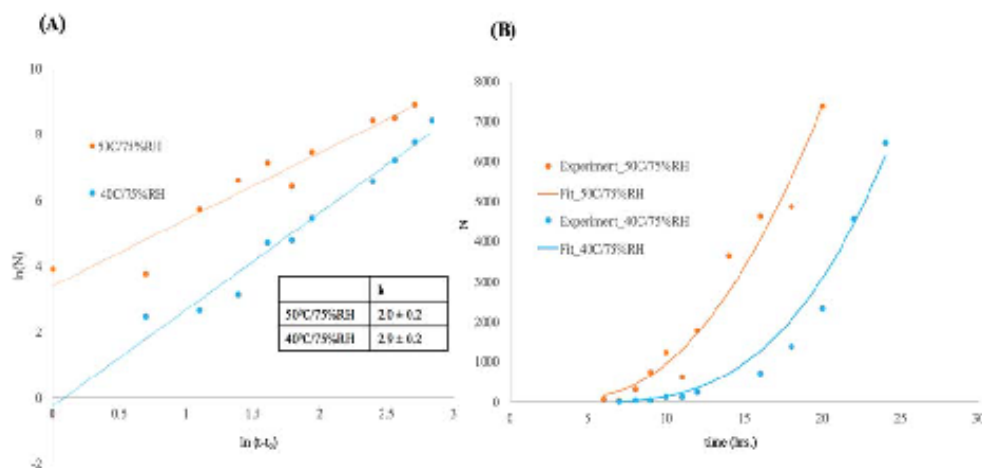


Figure 4. Kinetics of nucleation, plotted logarithmically (A) and linearly (B) to determine the exponential order parameter k in eq 4.

Particle counting approaches also allow determination of both the number of particles and the rate of new particle production (i.e., nucleation rate). The total crystalline volume fraction is a function of the combined rates of nucleation and growth through eqs 3 and 4. In Figure 4A, log-log plots of the nucleation rate recover the exponential parameter k in eq 4 from the slope, based on the relationship $N \propto (t - t_0)^k$. In contrast to the crystal growth rate, the nucleation rates (N versus t) were similar for both temperatures tested as shown in Figure 4B. It is worth noting that the nucleation rate was evaluated from data points appearing after the induction time, corresponding to the steady-state rate at which particles have both nucleated and subsequently grown to a size commensurate with reliable detection by SHG. As such, the nucleation rate is unbiased by the presence of a finite induction time.

Independent determination of the crystal nucleation and growth kinetics from particle counting of the SHG-active domains allows evaluation of the exponential parameters describing the overall crystallinity in eq 4. For crystallization reliably described by the JMAK model, the relationship $n \approx k + 3m$ is expected together with the total crystallinity scaling linearly with the average nucleation rate and cubically with the growth rate in the average particle radius. The slope results shown in Table 1 were fit via eq 4 and show good internal consistency with these expectations, suggesting general validity for use of the JMAK model.

Table 1. Parameter in JMAK Model

	k	m	$k + 3m$	n
50 °C/75%RH	2.0 ± 0.2	0.40 ± 0.04	3.2 ± 0.3	3.1 ± 0.2
40 °C/75%RH	2.9 ± 0.2	0.07 ± 0.05	3.1 ± 0.4	2.9 ± 0.3

While the nucleation kinetics were largely insensitive to the difference in temperature over the regime investigated as shown in Figure 4, the crystal growth kinetics in Figure 3 exhibited a steep temperature-dependence. A temperature-insensitive nucleation rate is consistent with a system in which both thermodynamics and kinetics play significant roles in driving nucleation. As the temperature is decreased, thermodynamics

suggests a higher supersaturation and a corresponding increase in nucleation rate (according to classical nucleation theory³⁰). In contrast, diffusion models suggest higher nucleation rates with increasing temperature for mass-transport limited processes. These two effects are described by ΔG_v and D in eq 5. A weak temperature dependence for nucleation, as observed for the current study, suggests that both effects are significant, such that the decrease in nucleation rates from thermodynamics as supersaturation decreases is largely offset by an increase in nucleation rates from diffusion at elevated temperature.

The increase in crystal growth rates with increased temperature is consistent with diffusion-limited kinetics over the temperatures investigated. In this case, simplification of eq 5 to the diffusion-only expression enables Arrhenius descriptions of diffusion. In order to extract the Arrhenius parameters for predicting the temperature-dependence of diffusion (and in turn, crystal growth rate), an estimate of the steady-state growth rate was generated from the latest five time points under each of the two stressed conditions explored, shown in Figure 3D. These points contained the least number of crystallites smaller than the lower limits of detection of the instrument. In this regime, the growth rates based on crystal size changes was most confidently recorded with minimal bias from nucleation. In this temperature range, the crystal growth rate was mainly dominated by diffusion. Based on the temperature-dependent crystal growth rate, the calculated activation energy of diffusion is 68.8 ± 4.3 kJ/mol, which is generally consistent with previously reported values for polymers.^{33,34}

It is worth comparing the results of the kinetic modeling of the SHG data to analogous modeling performed using conventional methods for crystallinity determination. The low limits of detection by SHG significantly reduce the induction time required to first observe the onset of detectable crystallinity for integration into kinetic modeling. In the case of API crystallization in amorphous solid dispersion, limits of detection on the order of 0.5% crystallinity are enabled by XRPD with a synchrotron source.¹⁶ From inspection of Figure 2, this limit of detection would correspond to four data points

in the 50 °C/75%RH crystallization trial and two data points in the 40 °C/75%RH trial over the same time frame of the experiment. With so few data points available, it would be challenging at best to assess the validity of any particular model for predicting crystallization kinetics by XRPD alone. In principle, longer times could be devoted to monitoring crystallization (e.g., several days or longer). However, the modeling becomes more challenging as the concentration of solubilized drug and the corresponding degree of supersaturation changes significantly at higher crystallinity. In addition, the present study was performed under conditions leading to relatively rapid crystal formation. For stability testing performed approximating ambient conditions, the timeframes required for observation of crystallinity to inform modeling by conventional benchtop methods can become prohibitive for routine optimization of formulations.

The importance of quantitative modeling for predictive behavior is particularly relevant to pharmaceutical analysis given the regulatory shifts toward QbD concepts for pharmaceutical characterization. QbD approaches rely on a quantitative understanding of key aspects of the formulation for predicting performance and bioavailability. For ASDs, stability is arguably one of the most critical factors to evaluate. The results summarized in Figure 2 demonstrate a dynamic range of detection by SHG spanning more than four decades (100 ppm to several %), the collective results of which can be integrated into a single unified kinetic model capable of predicting both the overall number and size distribution of API crystals under diverse storage conditions. In contrast, the dynamic range of many alternative benchtop methods routinely span 1 order of magnitude or less and provide little direct information on the size distribution. Consequently, the predictive capability of SHG microscopy measurements for QbD assessments is significantly improved relative to alternative established methods for samples amenable to SHG analyses. By using parametrized models, the measurements also allow prediction of anticipated trends under alternative conditions (e.g., ambient). This predictive ability can benefit long-term stability assessments for which the direct measurements are prohibitively time-consuming during formulation optimization.

While the use of SHG for analysis of amorphous solid dispersions has been demonstrated previously,¹⁵ the present study is unique in the use of image analysis for determination of not only the percent crystallinity, but recovery of the particle size distribution at each time-point. This additional information enabled independent determination of the nucleation and crystal growth rates, both of which combine to provide a complete description of crystallization kinetics in amorphous solid dispersions. Dissolution kinetics and correspondingly bioavailability is profoundly impacted by the particle size distribution, with dissolution arising more rapidly from a large number of small crystals as opposed to a small number of large crystals.³⁵

The SHG image analysis approach demonstrated in this work also has distinct practical advantages over established methods such as PLM. PLM can exhibit limits of detection well below 1% under favorable conditions. However, the image contrast for crystals is reduced by the presence of false-positive contributions from surface/edge effects in the sample, occlusions, scattering, etc. (representative SHG and PLM images are provided in Figure S1, in the Supporting Information). The high background and false-positives within the PLM images effectively render most automated particle counting image

analysis approaches inapplicable, such that images are often interpreted manually. In contrast, SHG exhibits little detectable background from occlusions and the polymer matrix, such that the resulting images are directly compatible with well-established and relatively simple automated image analysis algorithms. Compatibility with automated operation is clearly an attractive property for widespread adoption within the pharmaceutical community.

The particle counting approach described herein has the distinct advantage of being applicable irrespective of the crystal form of the SHG-active moiety or the need for calibration with a pure substance. Crystallinity is assessed entirely based on the calculated volume from individual particles. This capability is particularly advantageous in studies of pharmaceutical materials, as APIs often exhibit rich phase behavior with several crystal forms and/or polymorphs potentially accessible for crystal formation. Ritonavir is a particularly well-studied example of crystal polymorphism, in which the Form II polymorph exhibits significantly lower bioavailability in oral formulations relative to the metastable Form I. Confocal Raman and near-infrared spectra acquired from later stages in the crystallization were consistent with the more stable Form II produced in the present study, which are shown in Figure S2. Such combined measurements highlight the advantages of coupling quantitative analysis approaches such as SHG with qualitatively rich spectroscopic characterization methods.

While the focus of the present study is centered on characterization of extruded feedstock materials, it is worthwhile to consider the challenges associated with accelerated stability assessments in final dosage forms. For oral dosage forms comprised of compressed powders, additional crystalline excipients may be present in addition to the ASDs. Several strategies have been pursued for enabling quantitative analysis by SHG in these more complex matrices. UV-SHG has been shown to exhibit enhanced selectivity for aromatic APIs, enabling selective detection of crystalline API in the presence of crystalline sugars (e.g., lactose and mannitol).¹⁸ In addition, SHG-active particles can be targeted for subsequent Raman microscopy measurements for definitive determination of composition on a per-particle basis.²¹ Alternatively, synchrotron XRD can inform structural composition of individual microscopic particles identified for analysis by SHG.³² These strategies are generally compatible with the kinetic modeling approach described herein, although with the caveat that the lower limits of detection and temporal resolution may be compromised in complex multicomponent mixtures containing additional SHG-active excipients. Final dosage forms with amorphous excipients can generally be expected to be directly compatible with SHG analysis for quantification of crystallinity.¹⁹

CONCLUSION

In this study, SHG microscopy was used to develop analytical models for predicting the crystallization behavior of ritonavir in a model ASD formulation. The low (10 ppm v/v) limit of detection of SHG microscopy extended the range of data to incorporate into the model by ~2 orders of magnitude lower compared to other routine benchtop methods (e.g., DSC, XRPD) for ritonavir crystallinity detection in ASDs. Most significantly, SHG extends the measurement into the low crystallinity regime, in which the analytical modeling is simplified by the assumption of a constant average concentration in the polymer. Image analysis of the SHG micrographs

allowed separate evaluation of contributions from both nucleation and growth in dictating the overall net kinetics of crystallization. The values of crystallinity were demonstrated to be consistent with the JMAK kinetic model. This information allows prediction of both the anticipated crystalline fraction as well as the crystalline number density and size distribution. The temperature-dependent changes in the SHG microscopy images allowed for determination of a diffusional activation energy, which in turn allowed for modeling to predict the anticipated kinetics under unique experimental conditions. Since these results build off measurements acquired primarily for crystalline fractions much lower than 0.5%, the overall time frame for optimization of a particular ASD formulation has the potential to be substantially reduced through integration of SHG imaging. Consequently, full kinetic modeling with predictive capability can be performed with a collective set of measurements obtained at crystallinities below those typically required for simple pass/fail Boolean assessments in formulation optimization. Finally, mathematical understanding of the kinetics of crystallization facilitates quality by design (QbD) approaches in the development of formulations.

■ ASSOCIATED CONTENT

Supporting Information

The Supporting Information is available free of charge on the ACS Publications website at DOI: 10.1021/acs.analchem.7b04260.

Modification of instruments, the comparison of PLM and SHG for crystallinity detection, and the identification of ritonavir crystal form. (PDF)

■ AUTHOR INFORMATION

Corresponding Author

*E-mail: gsimpson@purdue.edu.

ORCID

Sreya Sarkar: 0000-0002-1614-3730

Garth J. Simpson: 0000-0002-3932-848X

Author Contributions

[†]Z.S. and S.S. contributed equally to this work.

Notes

The authors declare no competing financial interest.

■ ACKNOWLEDGMENTS

The authors gratefully acknowledge funding for the present work from the National Science Foundation through an NSF-GOALI award (No. CHE-1643745). In addition, Z.S. and S.S. acknowledge financial support for this work from AbbVie. The authors would also like to acknowledge Jayanth Doddi for assistance in sample preparation and Geoff G. Zhang for helpful feedback on the kinetic modeling. We would also like to acknowledge Formulatrix for the use of SONICC instrumentation.

■ REFERENCES

- (1) Serajuddin, A. T. M. *J. Pharm. Sci.* 1999, 88 (10), 1058–1066.
- (2) Kennedy, M.; Hu, J.; Gao, P.; Li, L.; Ali-Reynolds, A.; Chai, B.; Gupta, V.; Ma, C.; Mahajan, N.; Akrami, A.; Surapaneni, S. *Mol. Pharmaceutics* 2008, 5 (6), 981–993.
- (3) Guo, Y. S.; Shalae, E.; Smith, S. *TrAC, Trends Anal. Chem.* 2013, 49, 137–144.
- (4) Kommanaboina, B.; Rhodes, C. T. *Drug Dev. Ind. Pharm.* 1999, 25 (7), 857–868.

- (5) Waterman, K. C.; Adami, R. C. *Int. J. Pharm.* 2005, 293 (1–2), 101–125.
- (6) Yang, J.; Grey, K.; Doney, J. *Int. J. Pharm.* 2010, 384 (1–2), 24–31.
- (7) Sindait, W.; Leane, M.; Clarke, G.; Dennis, A.; Tobyn, M.; Timmins, P. J. *Pharm. Sci.* 2011, 100 (11), 4687–4699.
- (8) Schmelzer, J. W. P.; Boltachev, G. S.; Baidakov, V. G. *J. Chem. Phys.* 2006, 124 (19), 194503.
- (9) Carlton, R. A. *Polarized Light Microscopy*. In *Pharmaceutical Microscopy*; Springer: New York, 2011; pp 7–64.
- (10) Yoshihashi, Y.; Iijima, H.; Yonemochi, E.; Tenda, K. J. *Therm. Anal. Calorim.* 2006, 85 (3), 689–692.
- (11) Baird, J. A.; Taylor, L. S. *Adv. Drug Delivery Rev.* 2012, 64 (5), 396–421.
- (12) Ghebremeskel, A. N.; Venamarapu, C.; Lodaya, M. *Pharm. Res.* 2006, 23 (8), 1928–1936.
- (13) Berendt, R. T.; Speiser, D. M.; Ibbester, P. K.; Munson, E. J. *TrAC, Trends Anal. Chem.* 2006, 25 (10), 977–984.
- (14) Lubach, J. W.; Padden, B. E.; Winslow, S. L.; Salisbury, J. S.; Masters, D. B.; Topp, E. M.; Munson, E. J. *Anal. Bioanal. Chem.* 2004, 378 (6), 1504–1510.
- (15) Wanapun, D.; Kestur, U. S.; Kissick, D. J.; Simpson, G. J.; Taylor, L. S. *Anal. Chem.* 2010, 82 (13), 5425–5432.
- (16) Thakral, S.; Terban, M. W.; Thakral, N. K.; Suryanarayanan, R. *Adv. Drug Delivery Rev.* 2016, 100, 183–193.
- (17) Kissick, D. J.; Wanapun, D.; Simpson, G. J. *Annu. Rev. Anal. Chem.* 2011, 4, 419–437.
- (18) Toth, S. J.; Madden, J. T.; Taylor, L. S.; Marsac, P.; Simpson, G. J. *Anal. Chem.* 2012, 84 (14), 5869–5875.
- (19) Schmitt, P. D.; Tasi, N. S.; Taylor, L. S.; Simpson, G. J. *Mol. Pharmaceutics* 2015, 12 (7), 2378–2383.
- (20) Chowdhury, A. U.; Zhang, S. J.; Simpson, G. J. *Anal. Chem.* 2016, 88 (7), 3853–3863.
- (21) Chowdhury, A. U.; Ye, D. H.; Song, Z. T.; Zhang, S. J.; Hedderich, H. G.; Mälicke, B.; Thinnahari, S.; Ramakrishnan, S.; Sengupta, A.; Gualtieri, E. J.; Bouman, C. A.; Simpson, G. J. *Anal. Chem.* 2017, 89 (11), 5958–5965.
- (22) Toth, S. J.; Schmitt, P. D.; Snyder, G. R.; Trasi, N. S.; Sullivan, S. Z.; George, I. A.; Taylor, L. S.; Simpson, G. J. *Cryst. Growth Des.* 2015, 15 (2), 581–586.
- (23) Schmitt, P. D.; DeWalt, E. L.; Dow, X. Y.; Simpson, G. J. *Anal. Chem.* 2016, 88 (11), 5760–5768.
- (24) Danner, S. A.; Carr, A.; Leonard, J. M.; Lehman, L. M.; Gudiol, F.; Gonzales, J.; Raventos, A.; Rubio, R.; Bouza, E.; Pintado, V.; Aguado, A. G.; Delomas, J. G.; Delgado, R.; Borluffs, J. C. C.; Hsu, A.; Valdes, J. M.; Boucher, C. A. B.; Cooper, D. A.; Gilman, C.; Clotet, B.; Tor, J.; Ferrer, E.; Martinez, P. L.; Moreno, S.; Zancada, G.; Alcamí, J.; Notega, A. R.; Pulido, F.; Glassman, H. N. *N. Engl. J. Med.* 1995, 333 (23), 1528–1533.
- (25) Bauer, J.; Spanton, S.; Henry, R.; Quick, J.; Draki, W.; Porter, W.; Morris, J. *Pharm. Res.* 2001, 18 (6), 859–866.
- (26) Zhu, D. H.; Zograf, G.; Gao, P.; Gong, Y. C.; Zhang, G. G. Z. *J. Pharm. Sci.* 2016, 105 (9), 2932–2939.
- (27) Breitenbach, J. *Eur. J. Pharm. Biopharm.* 2002, 54 (2), 107–117.
- (28) Tho, L.; Liepold, B.; Rosenberg, J.; Maegerlein, M.; Brandl, M.; Fritzer, G. *Eur. J. Pharm. Sci.* 2010, 40 (1), 25–32.
- (29) Oksanen, C. A.; Zograf, G. *Pharm. Res.* 1990, 7 (6), 654–657.
- (30) Schmelzer, J. W. *Nucleation theory and applications*; Wiley-VCH: Weinheim, Germany, 2005.
- (31) Gutzow, L.; Schmelzer, J. *The vitreous state: thermodynamics, structure, rheology and crystallization*; Springer: Berlin, 1995.
- (32) Newman, J. A.; Schmitt, P. D.; Toth, S. J.; Deng, F. Y.; Zhang, S. J.; Simpson, G. J. *Anal. Chem.* 2015, 87 (21), 10950–10955.
- (33) Schmitt, E. A.; Law, D.; Zhang, G. G. Z. *J. Pharm. Sci.* 1999, 88 (3), 291–296.
- (34) Vrentas, J. S.; Vrentas, C. M. *J. Polym. Sci., Part B: Polym. Phys.* 2003, 41 (8), 785–788.
- (35) Amidon, G. L.; Lennemas, H.; Shah, V. P.; Crison, J. R. *Pharm. Res.* 1995, 12 (3), 413–420.